The Dissertation Committee for Marla Rose Knebl Lowrey certifies that this is the approved version of the following dissertation:

Regional scale flood modeling and watershed investigation, using NEXRAD rainfall, GIS, and HEC-HMS/RAS: A case study for the San Antonio River Basin, Texas

Committee:

____
Zong-Liang Yang, Supervisor

____
David Maidment

____
Keith Hutchison

____
Clark Wilson

____
John McCray

____
Philip Bennett

Regional scale flood modeling and watershed investigation, using NEXRAD rainfall, GIS, and HEC-HMS/RAS: A case study for the San Antonio River Basin, Texas

by

Marla Rose Knebl Lowrey, B.S.; M.M.E.

Dissertation

Presented to the Faculty of the Graduate School of

The University of Texas at Austin

In Partial Fulfillment

of the Requirements

for the Degree of

Doctor of Philosophy

The University of Texas at Austin

December 2006

Acknowledgements

This work was supported by funding from the Center for Space Research and the U.S. Department of Homeland Security Fellowship Program. I sincerely appreciate the assistance of the many agencies and people who provided data and support for this research, including staff at the West Gulf River Forecast Center, Hydrologic Engineering Center, U.S. Geological Survey, Texas Speleological Society, Texas Advanced Computing Center, National Center for Atmospheric Research, and Teresa Howard and Gayla Malson at the Center for Space Research for their assistance in remote sensing analysis.

I would also like to thank our climate research group for their thoughtful discussions and critiques: Guo-Yue Niu, Lindsey Gulden, Xiaoyan Jiang, Hua Su, Jeff Lo, and Xuemei Wang. Special thanks goes to all of my committee members, especially Keith Hutchison for initiating the project , David Maidment and his students Oscar Robayo and Pierre Gueudet for provision and assistance with GIS modeling, and Liang Yang for his continuous direction and support. Finally, I would like to thank my family and friends for their encouragement over the past few years, especially my mother, father, Sieg, and Rudi for their unconditional support through the many various paths I have taken, and Parker for his constant encouragement and unwavering confidence.

Regional scale flood modeling and watershed investigation, using NEXRAD rainfall, GIS, and HEC-HMS/RAS: A case study for the San Antonio River Basin, Texas

Publication No. ____________

Marla Rose Knebl Lowrey, Ph.D.
The University of Texas at Austin, 2006
Supervisor: Zong-Liang Yang

This research develops a methodology and framework for regional scale flood modeling that integrates NEXRAD Level III rainfall, GIS, and a hydrological model (HEC-HMS/RAS). The case study surrounds a summer storm event over the San Antonio River Basin (about 4000 square miles, 10000 square kilometers) in central Texas, USA, a region subject to frequent occurrences of severe flash flooding. The basic model design connects a rainfall-runoff model (HEC-HMS) with a hydraulic model (HEC-RAS) to model unsteady state flow. The infrastructure presented in this study extends the prototype Map to Map GIS tool to a regional scale. The preliminary model system is driven by NEXRAD 4km rainfall grids. Subsequent model experiments investigate the potential to use numerical weather forecasts of precipitation to drive the rainfall-runoff model. Results demonstrate that despite some significant errors, the calibrated model is capable of producing flood forecasts comparable to observed conditions. Addressing the heterogeneous nature of basin geomorphology and hydrology may aid in improving model accuracy. To this end, the variation in river and floodplain characteristics and their relationship to hydrologic behavior are investigated, and implications for future modeling efforts discussed. The regional scale flood model and watershed study will provide a useful tool for future flood studies over the San Antonio River Basin or similar catchments, and demonstrates the potential of increasing forecast lead time by incorporating numerical weather forecasts of rainfall into the modeling system.

TABLE OF CONTENTS

List of Tables

List of Figures

CHAPTER 1: INTRODUCTION

River flooding is a significant and nationwide problem; lack of understanding of watershed hydrologic response and modeling limitations result in insufficient lead-time for flood forecasts and costly damage to life and property. Severe flash flooding is endemic to central Texas; the region holds numerous world records for precipitation during storms of varying durations (Patton and Baker 1977). Increasing rates of urbanization threaten to worsen the effects of rainfall events. Global warming issues and extreme weather events in the recent past have further underscored the need for accurate predictions of flood levels and potential damages.

Recently, new methodologies and techniques have been developed in GIS that allow for more efficient storage and processing of data and joint analysis of numerous datasets. Widespread use of NEXRAD data has demonstrated that it can produce realistic rainfall patterns and intensities. The radar data is bias-corrected using gauges to further improve its accuracy. In this research, I hypothesize that 4-km NEXRAD gridded datasets are sufficient to drive a regional flood prediction system over the San Antonio River Basin.

The major motivations behind the present study include the following: 1) the need for regional scale models that address an entire river network; 2) the need to increase lead-time for mitigation steps necessary in preparing for the flood; and 3) the need to investigate the unique hydrologic signatures of watersheds. This study successfully incorporates NEXRAD data to develop a regional scale model that divides precipitation into infiltration and runoff at a fine-resolution grid scale. I also demonstrate the potential for increasing lead-time for forecasts by replacing NEXRAD real-time data with rainfall forecasts from a numerical weather prediction model. Finally, I delineate some of the important heterogeneities across the basin, and suggest modeling approaches to best account for these variations.

CHAPTER SUMMARIES

Chapter 2

This chapter addresses the development and forecast potential of a flood prediction system. The system utilizes GIS software to combine precipitation inputs with a hydrologic and hydraulic model to produce streamflow hydrographs and inundation polygons over the basin. Watershed divide and stream channel networks were delineated using a 10 meter DEM grid to derive slope and flow direction. Twelve subwatersheds were delineated based upon the locations of major gaging stations of the basin. NEXRAD Level III hourly 4-km estimates, which uses the standard tropical conversion from reflectivity to rainfall rate, were processed and used as the driving dataset for the model. STATSGO soil data and National Land Cover Dataset coverages were combined in GIS to produce curve number values at the gridded scale. Curve numbers were used to represent infiltration capacity and allowed rainfall to be partitioned into effective precipitation and losses, such as infiltration, detention, and evapotranspiration. Storage and attenuation of runoff was determined using unit hydrograph analysis. Flow routing in the hydraulic model was calculated using one-dimensional unsteady flow equations based upon cross-sectional channel geometry. Results from preliminary model runs demonstrated the ability of the regional-scale, semi-distributed model to provide useful flood alerts within the forecast framework.

Chapter 3

This chapter addresses the use of numerical weather model rainfall forecasts to drive the modeling system. Recent development of high resolution numerical weather models has spurred successful research into storm evolution and development. Increased understanding of the type and formation of precipitation allows for improved prediction of storm movement, timing, and intensity. This study tests the viability of these model products to predict flood events over the San Antonio River Basin. The Weather Research and Forecasting (WRF) model is driven with regional reanalysis data at a 32 km resolution, including all land surface variables. The data is downscaled to 12 km for WRF model runs, with a nested model at 4 km over the flood domain of interest (San Antonio Basin). For atmospheric calculations, 31 vertical layers are modeled, corresponding to pressure levels from 1000 mb to 100 mb at the model top. The WRF model was initialized on June 30, 2002 and integrated for eleven days to cover the entire storm duration. Output rainfall grids (4 km resolution) were then used to drive the model system. Model runs produced encouraging results and I conclude that WRF numerical forecasts can be used for hydrological flood event modeling, provided that the proper WRF configuration is used. Sensitivity studies using ensemble realizations of physics, initialization, and domain were undertaken to determine the best-fit scenario for WRF modeling of the San Antonio River Basin. Finally, numerous small perturbations to the best-fit grid were implemented and run through the hydrological model to determine significance and predictability of error in WRF. Results demonstrate that locations errors are most significant and detrimental to flood forecasting.

Chapter 4

This chapter addresses the heterogeneity of geomorphic characteristics across the watershed system, and its relation to hydrologic response. This variability is described, classified, and analyzed to determine efficient ways to incorporate information into the model. Several examples are provided that demonstrate the applicability of this knowledge, along with suggestions for further improvement. Datasets such as topography, land use, vegetation, soils, climate, and literature on geologic history were studied. Aerial photography provided most geomorphic observations and calculations, such as drainage density and sinuosity. Hydrologic data gathered included flow hydrographs, channel cross-sections, and water table data from well investigations. Based upon the above investigations, the watershed was divided into three major regions, (although recognizing that variability also exists within the regions): hilly source regions on Edwards limestone bedrock, urbanized and highly dissected midstream areas over the Balcones Fault Zone, and low-relief downstream areas in alluvial sediments of the Gulf Coastal Plain. Results from this investigation demonstrate large variability among the regions in river and floodplain characteristics that are manifested in differences in hydrologic behavior. Different modeling approaches are recommended for each unique region.

Chapter 2: Regional Scale Flood Modeling Using NEXRAD Rainfall, GIS, and HEC-HMS/RAS: A Case Study for the San Antonio River Basin Summer 2002 Storm Event

ABSTRACT

This research develops a framework for regional scale flood modeling that integrates NEXRAD Level III rainfall, GIS, and a hydrological model (HEC-HMS/RAS). The San Antonio River Basin (about 4000 square miles, 10000 square kilometers) in central Texas, USA, is the domain of the study because it is a region subject to frequent occurrences of severe flash flooding. A major flood in the summer of 2002 is chosen as a case to examine the modeling framework. The model consists of a rainfall-runoff model (HEC-HMS) that converts precipitation excess to overland flow and channel runoff, as well as a hydraulic model (HEC-RAS) that models unsteady state flow through the river channel network based on the HEC-HMS derived hydrographs. HEC-HMS is run on a 4 km × 4 km grid in the domain, a resolution consistent with the resolution of NEXRAD rainfall taken from the local river authority. Watershed parameters are calibrated manually to produce a good simulation of discharge at 12 subbasins. With the calibrated discharge, HEC-RAS is capable of producing floodplain polygons that are comparable to the satellite imagery. The modeling framework presented in this study incorporates a portion of the recently developed GIS tool named Map to Map that has been created on a local scale and extends it to a regional scale. The results of this research will benefit future modeling efforts by providing a tool for hydrological forecasts of flooding on a

regional scale. While designed for the San Antonio River Basin, this regional scale model may be used as a prototype for model applications in other areas of the country.

1.INTRODUCTION

Flooding induced by storm events is a major concern in many regions of the world (e.g., Townsend and Walsh, 1998; Dutta et al., 2000; Dolcine et al., 2001; Sheng et al., 2001; Bryant and Rainey, 2002; Horritt and Bates, 2002; Lee and Lee, 2003; Hudson and Colditz, 2003). In a time period of six years (1989–1994), eighty percent of declared federal disasters in the United States were related to flooding; floods themselves average four billion dollars annually in property damage alone (Wadsworth, 1999). The extreme weather in recent years has demonstrated the necessity of reliable flood models, as emergency managers and city planners begin to realize the importance of advance warning in severe storm situations. As globally averaged temperatures increase, the potential for severe to extreme weather events increases (Becker and Grunewald, 2003; WMO, 2003). Therefore, global warming has brought further urgency to the prediction of flood levels and damages.

Flood inundation modeling requires distributed model predictions to inform major decisions relating to planning and insurance (Bates, 2004). Since the blueprint paper by Freeze and Harlan (1969), flood modeling has greatly improved in recent years with the advent of geographic information systems (GIS), radar-based rainfall estimation using next generation radar (NEXRAD), high-resolution digital elevation models, distributed hydrologic models, and delivery systems on the internet (Garrote and Bras, 1995; Bedient et al., 2003). There are, however, major issues that limit the accuracy in flood forecasts. These issues include errors associated with the radar rainfall input (Vieux and Bedient, 1998; Borga, 2002; Grassotti et al., 2003; Jayakrishnan et al., 2004), realism of model structure (Horritt and Bates, 2002), availability of distributed data to parameterize and validate the models (Bates, 2004), and scaling theory to relate point measurements to grid-averaged quantities predicted by the models (Beven, 2002; Bates, 2004). In addition, the time required to convert the NEXRAD rainfall time series to a flood inundation map is critical in practical applications, especially during the extreme storm events that demand a highly efficient predicting capability.

Despite the progress in flood modeling research, flooding continues to plague many areas of the world, including regions such as Central Texas. In the summer of 2002, a major precipitation event caused extensive flooding, twelve deaths, and nearly one billion dollars in damage in the San Antonio River Basin, which is the case presented in this study. Urban areas such as San Antonio are especially prone to flooding due to the large proportion of impermeable surface cover such as concrete that increases the total volume of runoff and peak flows and shortens the time that the floodwaters take to arrive at peak runoff (Hall, 1984).

Recent work in the area of flood modeling has focused on developing more efficient tools for ArcGIS. Robayo et al. (2004) developed a new Map to Map tool that couples NEXRAD precipitation time series with GIS applications and hydrological modeling to produce a floodplain map. This Map to Map technology involves the creation of an ArcHydro data model in GIS, an Interface Data Model (IDM) for each outside model that shares data with the GIS, and a number of scripts to process the data in GIS. A more in-depth description of Map to Map can be found in Whitaker et. al. (2004) and Whiteaker and Maidment (2004). Successful pilot tests of the Map to Map tool have been made in small basins including the Salado Basin (222 square miles) and the Rosillo Basin (29 square miles). These two basins are small catchments located within the much larger San Antonio River Basin. The nearly 4000 square mile San Antonio River Basin contains numerous other small catchments, and thus demonstrates much diversity of land cover, geology, and topography.

The Map to Map methodology has proven successful at the local and small basin scale, but until now has not been applied to a regional scale model. As the first of a series of studies that focus on regional scale flood forecasts, this study extends the Map to Map technology to the entire San Antonio River Basin. Major goals of this research include: 1) the development of a hydrological model of the San Antonio River Basin and the implementation of NEXRAD precipitation products in the model; and 2) the analysis of rainfall-runoff characteristics of the basin and adequacy of current infiltration methods for describing these basin characteristics. The methodology presented in this study attempts to create a streamlined process of rainfall input and floodplain output that will enable researchers to model rainfall-runoff relations with greater efficiency and will also contribute to improvements in the ability of Texas counties to respond in the scenario of a disastrous flooding event.

The structure of the study is as follows. Section 2 describes the major datasets used in development of the model. Section 3 outlines the parameterizations used and descriptions of both the rainfall-runoff model and the hydraulic model, and Section 4 describes the processing and calibration of the model. Section 5 discusses results and the potential utility of model development, and Section 6 draws some concluding remarks.

2. DATASETS

The study area selected for model development is the San Antonio River Basin, a 3,921 square mile basin located in South Central Texas (Figure 2.1). San Antonio, a city of 1.1 million people, is situated in the middle section of the basin. The temporal extent of the study was selected as June 30–July 9, 2002 to cover the duration of the summer storm of 2002. Heavy rainfall (3–10 inches/day) was observed from days 1 to 6 (or June 30–July 5), while days 7–10 (or July 6–9) fall on days in which rainfall was minimal or zero. Days 5-7 coincide with peak stream gage heights at area stations.

Rainfall inputs to the model were processed to convert binary rainfall intensities into a format compatible for input into the gridded hydrological model. Traditional rain gages are often sparse and do not provide a fine enough resolution for accurate runoff calculations and flood warnings (Ahrens and Maidment, 1999; Bedient et al., 2003). NEXRAD radar data have performed well in comparison studies with ground-based gages and have led to the consensus that the data are a high quality input to hydrological models (HEC, 1996a,b; Reed and Maidment, 1995). The accuracy of NEXRAD rainfall is dependent on the Z-R relationship used to convert reflectivity Z to rainfall rate R. In a case study of an extreme storm event in South Texas in October 1994, Vieux and Bedient (1998) found that use of the traditional Z-R relationship, $Z=300R^{1.4}$, caused significant errors when compared to rain gauge accumulations. The tropical Z-R relationship, $Z=250R^{1.2}$, performed much better. The tropical Z-R has been recommended for use where appropriate by the National Weather Service (NWS) since 1995; hence, the use of the more accurate Z-R relationship should reduce errors in tropical rainfall estimation for storms such as in the present study. The type of precipitation product used may also make a significant difference in output when used to drive hydrologic models. Grassotti et al. (2003) compared rainfall estimates from three different products, 1) hourly 4-km resolution P1 (an update to the Stage III process) estimates, 15-min 2-km resolution NOWrad estimates, and conventional hourly rain gage observations, and found that the 4-km P1 estimates demonstrated the best agreement with rain gage observations. For the present study, NEXRAD Level III datasets over the calibration period were obtained in a four kilometer gridded format from Texas' West Gulf River Forecast Center and processed into a format compatible with the hydrological model. Table 2.1 displays daily rainfall totals extracted from this NEXRAD data for subbasins in the study region.

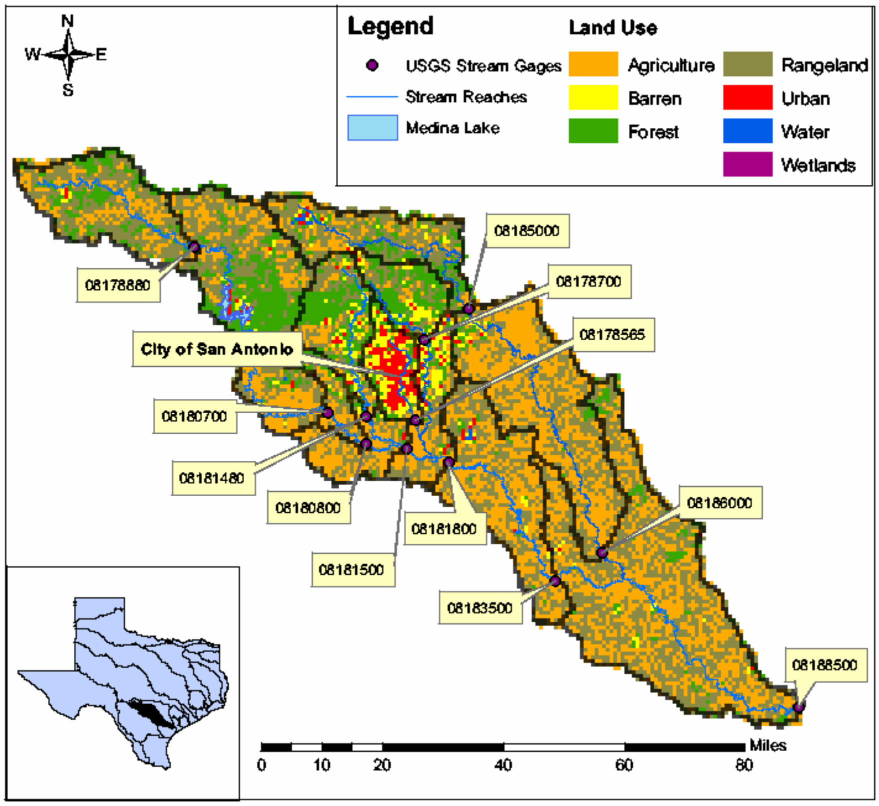

Figure 2.1. Map of the San Antonio River Basin. Prominent features include the 12 subbasins and numerous river reaches delineated in this research, the 12 USGS gauging stations coinciding with outlet points of the 12 subbasins, land-cover data, and the model grid used in the study. The model grid consists of 4 km x 4 km cells used for hydrologic processing of runoff.

Table 2.1: Daily rainfall totals for subbasins in the San Antonio River Basin

Subbasin ID	Precipitation (in) Date									
	6/30/02	7/1/02	7/2/02	7/3/02	7/4/02	7/5/02	7/6/02	7/7/02	7/8/02	7/9/02
08178880	4.30	0.84	6.98	2.09	5.57	5.67	0.05	0.09	0.03	0.09
08180700	3.83	4.81	6.27	5.50	4.26	2.69	0.00	0.03	0.17	0.13
08185000	3.87	4.35	8.92	4.48	3.25	3.15	0.01	0.07	0.14	0.19
08178700	2.92	4.36	10.16	2.70	1.56	2.31	0.05	0.03	0.04	0.33
08181480	3.76	5.31	7.08	4.38	4.73	3.19	0.03	0.01	0.05	0.29
08178565	2.10	6.47	5.94	2.43	2.18	2.58	0.06	0.00	0.00	0.37
08180800	2.86	8.03	4.20	3.92	4.88	3.92	0.00	0.00	0.00	0.22
08181800	1.10	7.57	2.88	0.91	0.52	3.02	0.01	0.00	0.00	0.40
08181500	1.61	7.17	1.62	1.71	3.64	2.92	0.03	0.00	0.00	0.48
08186000	2.27	5.15	4.11	0.50	0.11	2.73	0.11	0.00	0.00	0.25
08183500	1.74	6.52	2.70	0.90	0.14	3.18	0.04	0.00	0.00	0.21
08188500	0.61	3.89	2.62	0.11	0.10	1.96	0.15	0.00	0.11	0.69

Topography was downloaded from the USGS National Elevation Dataset (NED), a continuously updated grid of elevation values across the country with a minimum resolution of 30 meters. The data are among the highest quality and finest resolution available at the basin scale. The preliminary model used a 30 meter resolution only; Digital Elevation Models (DEMs) of 10 meter resolution where available were incorporated into later model runs. The 30 meter elevation product was resampled to a 10 meter grid and updated with the 10 meter values where available (approximately 75 percent of the basin).

Twelve USGS stream flow gages with complete hydrological datasets formed a base of streamflow observations over the study region, including both discharge measurements and gage heights. These datasets were used both in parameter derivation and in calibration of the model. Information about the land surface was gathered from multiple sources. The U.S. Department of Agriculture Soil Conservation Service (now the National Resource Conservation Service) holds a database of soils data for each state, called the State Soil Geographic Database (STATSGO). These data are derived from 1:250,000 scale USGS quadrangles. The National Land Cover Dataset created by the USGS (NLCD92) contains information about the land use and cover at a 30 meter resolution over most regions of the United States. This dataset divides land use and land cover into 21 categories, which were aggregated as shown in Figure 2.1. Finally, river geometry is necessary to run the hydraulic model; the data were obtained by combining measured survey data with cross-sections delineated from the DEM.

3. MODEL DESCRIPTION

3.1. Rainfall-runoff model: HEC-HMS

Runoff is modeled using the Hydrologic Engineering Center's Hydrologic Modeling System (HEC-HMS), version 2.2.1. HEC-HMS, developed by the U.S. Army Corps of Engineers, is designed to simulate the precipitation-runoff processes of dendritic watershed systems. HEC-HMS allows the modeler to choose between numerous infiltration loss parameterizations (HEC, 2000). However, only the gridded curve number technique enables spatially distributed infiltration calculations. Infiltration capacity is quantified in a parameter derived by the Soil Conservation Service (SCS) called the curve number (CN). The curve number is a method for determining storm runoff over an area based on land use, soil and land cover type, and hydrologic soil group (U.S. SCS, 1986). Soil groups are determined based on type and infiltrability of a soil. The infiltration loss method is derived from a set of empirical equations that define the partitioning of rainfall into infiltration and runoff,

$$Q = (P-I_a)^2 / ((P-I_a) + S) \qquad (1)$$

$$I_a = 0.2S \qquad (2)$$

$$S = (1000/CN) - 10 \qquad (3)$$

Substituting (2) into (1) gives

$$Q = (P-0.2S)^2 / (P+0.8S) \qquad (4)$$

where Q = runoff in inches

P = rainfall in inches

S = potential maximum retention

I_a = initial abstraction

CN = runoff curve number

This CN parameter was derived for each grid cell using an Avenue script that combines STATSGO soils data with the land use data layer. For the San Antonio area, most soils are classified into Hydrologic Soil Group C, which corresponds to soils having a low infiltration rate when thoroughly wetted, often with impeding layers in the soil, and curve number of approximately 75-90 (Chow et al., 1988). Initial abstraction is a variable parameter that takes into account losses prior to the start of runoff such as interception and depression storage. Evapotranspiration losses are considered negligible for the preliminary model due to several factors: the intensity of the storm being modeled, the continuous saturation of the air, and the resulting assumption that ET volume is negligible compared to runoff volume. Model runs testing this hypothesis demonstrated minimal to no effect on the subbasin hydrographs during the 10-day storm.

Translation of excess precipitation to runoff is accomplished using the ModClark algorithm, a version of the Clark unit hydrograph transformation modified to accommodate spatially distributed precipitation (Clark, 1945). This method convolves precipitation increments with the unit hydrograph ordinates to determine the basin hydrograph, $Q_n=\sum P_m*U_{n-m+1}$, as m goes from 1 to n, where n is the number of simulated hydrograph ordinates. Time of concentration for each cell in the basin is derived as $t_{cell}=t_c*(d_{cell}/d_{max})$, where t_c is the time of concentration for the subwatershed and is a function of basin length and slope, d_{cell} is the travel distance from the cell to the outlet, and d_{max} is the travel distance from the cell furthest from the outlet. The method requires an input coefficient for storage, R, where R accounts for both translation and attenuation of excess precipitation as it moves over the basin toward the outlet. Storage coefficient R is estimated as the discharge at the inflection point on the recession limb of the hydrograph divided by the slope at the inflection point. The translation hydrograph is routed using the equation (HEC, 2000)

$$Q(t) = [(\Delta t / (R + 0.5\Delta t)) * I(t)] + [(1 - (\Delta t / (R + 0.5\Delta t))) * Q(t-1)] \qquad (5)$$

where

$Q(t)$ = outflow from storage at time t

Δt = time increment

R = storage coefficient

$I(t)$ = average inflow to storage at time t

$Q(t-1)$ = outflow from storage at previous time t-1

Baseflow can be an important parameter in flood studies because it defines a minimum river depth over which additional runoff accumulates. Models that neglect baseflow may underestimate water levels and therefore fail to identify inundated reaches. Baseflow is modeled using an exponential decrease function, $Q=Q_o*e^{-kt}$, where k is a fitting parameter.

3.2. Hydraulic model: HEC-RAS

The hydraulic model is based on HEC's River Analysis System (HEC-RAS), version 3.1 (HEC, 2002). HEC-RAS calculates one-dimensional steady and unsteady flow, and the model equations are also described by Horritt and Bates (2002). The hydraulic model requires as input the output hydrographs from HMS; its parameters are representative cross-sections for each subbasin, including left and right bank locations, roughness coefficients (Manning's n), and contraction and expansion coefficients. Roughness coefficients, which represent a surface's resistance to flow and are integral parameters for calculating water depth, were estimated by combining land use data with tables of Manning's n values such as that found in HEC (2002). As present engineering studies are completed throughout the basin, more detailed cross-sectional data will be incorporated into the model. Due to the regional scale of the model, channel geometry was considered only for the larger streams in the network: the San Antonio and Medina Rivers, and the Salado, Cibolo, and Leon Creeks (Figure 2.2). In order to use the RAS model to develop floodplain maps, it must be georeferenced to the basin. Hence, the

DEM formed the basis for derivation of channel geometry, and was enhanced by available cross-sections from the USGS and other field measurements.

4. MODELING METHODOLOGY

4.1. Processing steps

The development of the present flood model integrates GIS with the HEC-HMS rainfall-runoff model and the HEC-RAS river hydraulic model. Numerous past studies have shown these models to provide accurate and useful results in flood related studies (Ahrens and Maidment, 1999; Anderson et al., 2002). An additional component of this research involves Map to Map, the aforementioned tool developed for ArcGIS by the research team of Professor David Maidment of the University of Texas at Austin College of Engineering. Map to Map's model infrastructure accepts processed rainfall data, a rainfall-runoff model, and a hydraulic model, and streamlines the processes into one operation that delineates polygons showing the floodplain extents (O. Robayo, pers. comm.). The Map to Map tool was modified by the author to meet the specific needs of the present research, including accommodations for unsteady flow and the incorporation of dissimilar precipitation products. This research tests the utility of the prototype Map to Map in regional-scale flood investigations. A flow chart outlining the fundamental steps in the model development is shown in Figure 2.3.

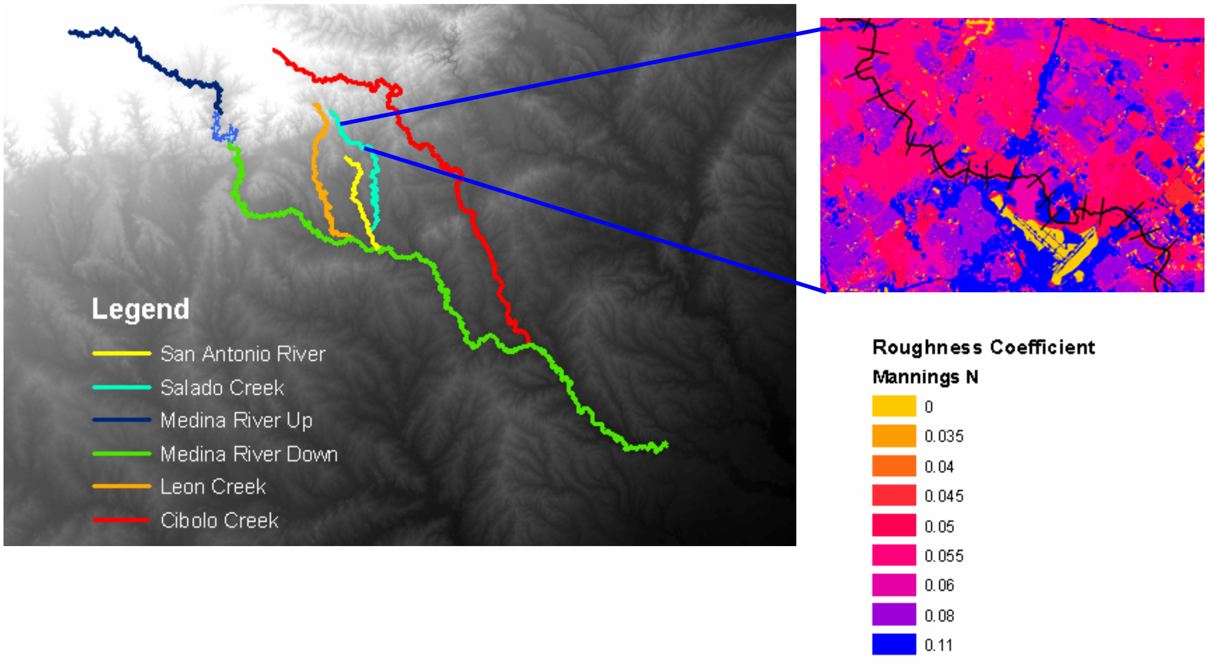

Figure 2.2. Six subreaches of the San Antonio River Basin overlain on the 10 meter DEM; each reach is run as a separate project in the hydraulic model. The inset figure displays a portion of Salado Creek (north of San Antonio), locations of extracted cross-sections, and roughness coefficients for the river and floodplain area. High Manning's N values imply a lower velocity flow.

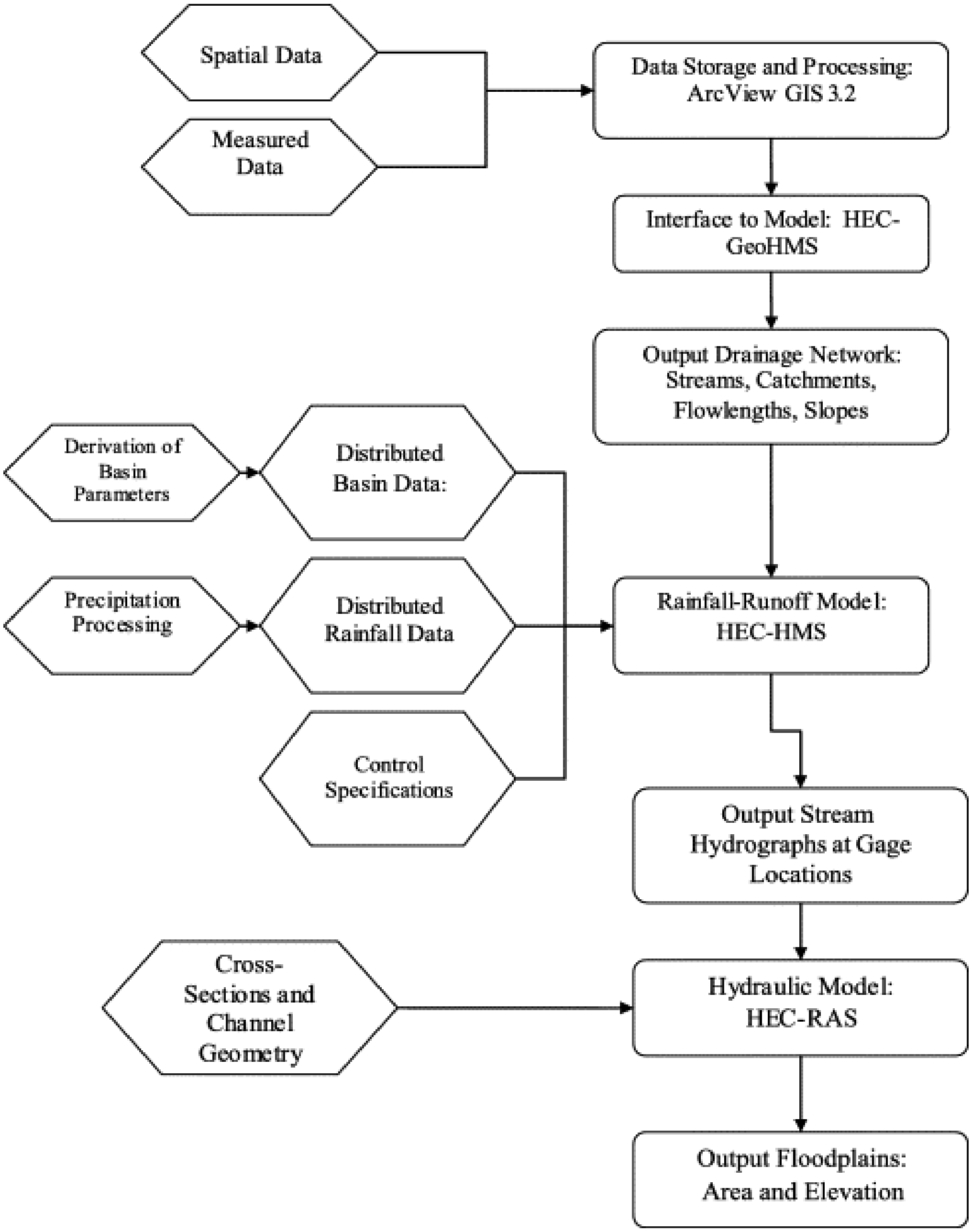

Figure 2.3. Steps in model design. Spatial data such as land use and elevation were gathered in addition to measured data such as the USGS discharge time series. Processing of data was completed in ArcView GIS 3.2 and exported to the hydrological model HEC-HMS through the model interface HEC-GeoHMS. Binary files of rainfall were processed and basin parameters were derived for the study area; the hydrological model was run using these inputs. Channel geometry was derived using elevation data, and output hydrographs were then used as input to drive the hydraulic model HEC-RAS. Finally, time series of cross-section heights were processed in ArcGIS and converted to flood inundation polygons. The Map to Map tool used in this study connects each of these processes and allows them to run as a single process.

Using ArcGIS, a geodatabase was created to contain all of the above mentioned data. The data were imported, merged, reprojected into the Albers Equal Area coordinate system and the NAD83 datum, and clipped to the study area. While much of this functionality is available in ArcGIS, some processes required outside scripts from various authors, such as the Grid Projection Extension (author: K.R. McVay) used to process raster data.

Following collection and processing of data, the stream network was delineated. An extension of GIS called HEC-GeoHMS executes this function through a series of steps collectively known as terrain preprocessing, implying the utilization of the surface topography as the origin of the stream network. The importance of using an accurate and high-resolution DEM for hydrologic modeling is underscored by these terrain preprocessing steps; if the DEM used is not sufficiently accurate, simulated rivers may follow very different paths from their actual pathways, and consequently watersheds will be delineated incorrectly. Two major methods exist for drainage network delineation from topography: the area-threshold method and the slope-area method. A comparison of the results obtained by the two methods has shown little difference between the two delineations (Giannoni et al., 2003). The area-threshold method was used in this study due to the gridded nature of the input datasets. In this method, water in each grid cell can potentially flow into any of the eight surrounding cells; the algorithm maps the water into a neighboring cell along the path of steepest descent. Each cell is then assigned a value according to how many cells flow into that particular cell. A threshold of upstream drainage area (in units of cells) is then specified by the modeler; every cell exceeding that threshold value becomes part of the stream network, i.e., part of the channel flow.

HEC-GeoHMS also includes functionality to delineate subbasins from the network and local topography; for calibration purposes, locations of USGS stream gages were designated as subbasin outlets. Figure 2.1 demonstrates the preliminary drainage system delineated over the San Antonio River Basin.

A rainfall-runoff model simulates the runoff response of an area to a given amount and distribution of precipitation over a defined period of time. The output of the model is the discharge hydrograph at each subbasin outlet; hydrograph characteristics define each subbasin's unique runoff response due to differences in watershed properties including geology, geomorphology, and anthropogenic effects. The creation of the rainfall-runoff model requires three files of input data: a map file, a grid cell parameter file, and a distributed model file. The map model file is a background file for spatial reference around the basin. The grid cell parameter file describes the location and properties of each cell across the basin; the modeler must first derive curve numbers representing each grid cell for input into this file. This file was used with the ModClark method of transforming rainfall to runoff, and the grid chosen for this process was the Standard Hydrologic Grid (SHG), which uses a custom Albers Equal Area projection. The distributed model file contains the hydrologic elements and their connectivity, and links the subbasins to the gridded data in the grid cell parameter file.

Hydrographs extracted from the rainfall-runoff model were saved as time series data and inputted directly into the hydraulic model. The model computed an unsteady flow analysis to derive water levels in the river network. These water levels were then exported back to the geodatabase and overlain on the DEM. At each grid cell, water elevation was checked against the topographic elevation - if water elevation was greater than the terrain elevation, then the cell was assigned a value of 1; otherwise, the cell was assigned a value of 0. The flood polygon was then drawn by the GIS and consisted of all cells having a value of 1. The flood polygons for each reach can be displayed and analyzed in the GIS, making the model methodology very versatile and simple to apply to various applications.

4.2. Model calibration

Calibration of the model with appropriate data is a crucial step in the creation of a reliable basin representation. Watershed parameters such as infiltration coefficients, time of concentration, and baseflow may need modification to produce a best fit between model and observations. Discharge output from a rainfall-runoff model is generally calibrated with observed streamflow. During severe storms, gage capacity is sometimes exceeded and streamflow must be extrapolated to record measurements; this extrapolation carries potential error that must be taken into account in flood studies (S. Gonzales, pers. comm.). The hydraulic model delineating floodplain extent should be validated with an accurate image of flooding during the storm in question. Remote sensing is a valuable tool for this purpose. Several studies have utilized remote sensing data such as that from Landsat Thematic Mapper (TM) to determine the extent of floodplain inundation (Townsend and Walsh, 1998; Hudson and Colditz, 2003). The Landsat data over San Antonio (Path 27 Row 39) was processed by the Center for Space Research with an algorithm that produces spatial extent of flooding during the storm event. The satellite pass over the study area occurs once every sixteen days; the one date with available Landsat data, July 8 2002, was chosen for comparison with model output. This date is several days past the storm peak, and therefore represents flood response after nearly a week of heavy rainfall.

Upon completion of model development and trial runs, the model presented in this study was calibrated against measured data to assess its ability to reproduce flooding from the July 2002 storm event. This determination involved several sets of data: the flood hydrographs produced at USGS gaging stations, and flood area as determined from Landsat TM satellite data. The output from the rainfall-runoff model was used to assess the accuracy of the model in reproducing hydrograph response, including flood peaks. Estimated parameters were modified to produce a best-fit model. It is important to note that the calibration was performed at two scales: 1) watershed parameters were modified at the subbasin scale (200 km^2 or more) and 2) curve numbers were modified at the ModClark grid cell scale (4 km^2). The calibrated best-fit parameters are specific to the San Antonio watershed and thus, although surrounding basins may display similar topography and sedimentological characteristics, implications from calibration do not extend beyond the study basin. However, since the 2002 storm evolution is characteristic of typical Texas warm-season convective storms, the best-fit parameters can be assumed constant for all storm events of this type.

5. RESULTS AND DISCUSSION

Preliminary results for the hydrological model showed a reasonable fit between model and observations; hydrograph shape and timing of peaks matched well, although the model tended to overestimate runoff. In the majority of subbasins, the hydrograph shape was accurately reproduced in model output. However, the model overestimated volume of runoff and frequently did not accurately define peak sharpness as observed through stream measurements. Calibration of the model improved results by greatly decreasing the volume of runoff and improving peak sharpness at most locations.

Initial calibration efforts altered the values of curve numbers on a regional scale (Figure 2.4) and modified other watershed parameters (Table 2.2) for each subbasin to more accurately represent surface flow over the region. The calibration efforts have shown promising results (Figure 2.5, Table 2.3). As an example, subbasin 08180700 initially had a percent bias of 215, a mean absolute error of 215 percent, and a correlation coefficient of 0.92. After calibration, these were, respectively, reduced to -1, 22, and 0.93. This reduced error is mostly due to the underestimation of peak and peak sharpness in the model. The most sensitive parameters were found to be the time of concentration of the basin, the initial abstraction (I_a), and the curve number (Table 2.2 and Figure 2.4). Modifying the time of concentration improved the timing of peaks, both absolute and in relation to other peaks. Since each subbasin has unique infiltration, topography, soils, etc., the time of concentration in some basins was increased while in others was decreased from its calculated value. The initial abstraction, defined in Equation 2, was determined in many subbasins to be too low. This value was increased to account for additional abstractions that may include detention areas or man-made structures. Curve numbers were decreased for subbasins as necessary to optimize the model fit (Figure 2.4). Decreasing the curve number increased the amount of recharge into the watershed system and therefore reduced overestimation of runoff in the model. In addition, the hydrologic routing method was modified to include a greater ratio of attenuation to translation of runoff in the subbasins; this change in routing method significantly improved the model results. The results for Cibolo Creek subbasins (08185000, 08186000) consistently overestimate runoff in the model, even after calibration. Further calibration is necessary to reduce model error for this section of the basin. Only one subbasin, basin number 08178880, currently demonstrates a significant underestimation of runoff. This is mostly due to the large peak in measured streamflow on July 5; in the modeled hydrograph for this subbasin, the July 5 peak is much smaller. Basin 08178880, the northernmost subbasin in the study area, is one of the largest subbasins, and hence averaging of basin parameters may have lead to model error. However, it is quite likely that the extrapolation of peaks due to the exceedance of gage capacity during extreme storm flows resulted in an erroneously high measurement of streamflow during these periods ((S. Gonzales, pers. comm.).

It is clear from the calibrated hydrographs (Figure 2.5) that different subbasins show different degrees of agreement between modeled and observed discharge. There are several possible explanations for this result. Basins with a greater diversity of watershed characteristics, including topography, soils, and land use, will produce poorer results at the regional scale than more homogeneous basins. The availability of USGS streamflow data limited the number of basins for which watershed parameters (time of concentration, baseflow) could be derived. In this research it was found that averaging basin properties over larger areas appeared to decrease model accuracy. Another possible source of error is the differences in data resolutions. The NEXRAD precipitation grid is overlain on the model at a 4 km resolution. The ModClark grid, the grid at which runoff calculations are made, is at a 4 km^2 (2km x 2km) resolution to match the NEXRAD data. The finer resolutions of the land cover and soils data is converted to an infiltration coefficient (CN) and averaged to get one value for each 4 km^2 grid cell. The use of data values derived at different resolutions to determine runoff may lead to errors in the outflow hydrographs. Although CN is derived from physical measurements, it is an empirical parameter and hence is a limitation in the present model. A more physically based approach to infiltration of water into soils such as the Green and Ampt parameterization (Green and Ampt, 1911) might improve model accuracy.

The final output of the model consists of flood polygons showing inundated areas over the basin. Flood inundation results were derived separately for each river reach in the San Antonio Basin. A total of six river reaches were processed over the basin; an example of floodplain output over a portion of one reach is shown in Figure 2.6. The

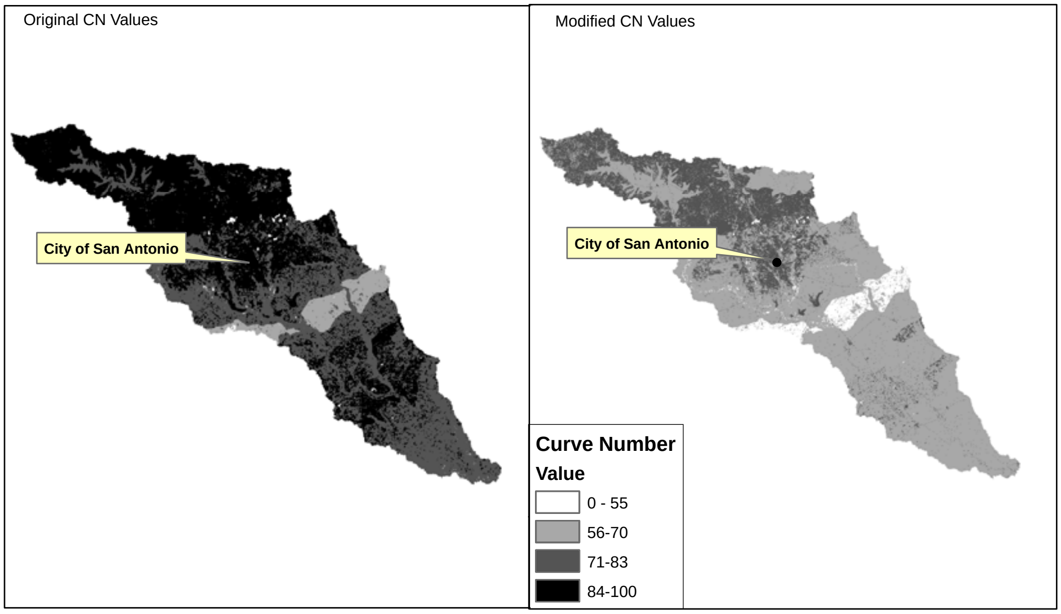

Figure 2.4. Modification of curve number during model calibration. The figure on the left is the infiltration grid prior to calibration displaying the curve number distribution across the basin. The figure on the right is the infiltration grid after calibration; curve numbers were decreased approximately 20% across the basin to correct for overestimation of runoff volume in the preliminary model.

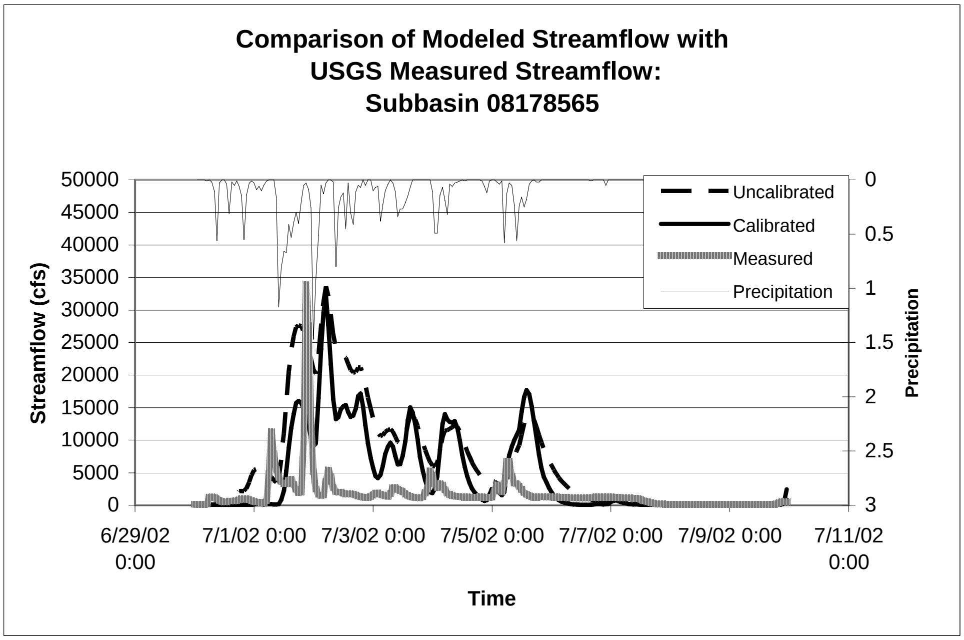

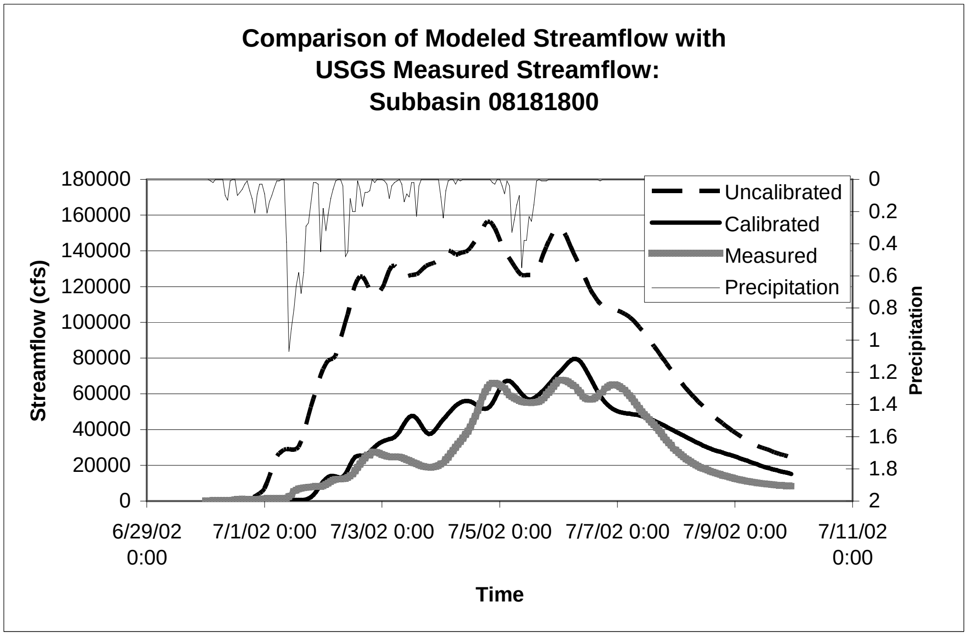

Figure 2.5. Hydrologic model results and calibration for a selected downstream portion of the San Antonio River. Subbasin 08178565 is located on the San Antonio River 12 km south of downtown San Antonio, and Subbasin 08181800 is located 20 km downstream from 08178565. The figures compare measured results (hatched line) with uncalibrated (dashed line) and calibrated (solid line) modeled results. Precipitation time series are included for reference.

Table 2.2: Original and calibrated lumped subbasin parameters

Subbasin ID	Time of concentration (hrs)		Storage coefficient (hrs)		Initial Baseflow ft^3/s		Initial Abstraction Ratio	
	Orig.[1]	Calib.[2]	Orig.[1]	Calib.[2]	Orig.[1]	Calib.[2]	Orig.[1]	Calib.[2]
08178880	96	5	185	20	14.94	14.94	0.20	0.35
08180700	96	10	76	35	53.78	53.78	0.20	0.40
08185000	96	4	71	20	0.0	0.0	0.20	0.35
08178700	48	6	22	10	0.0	0.0	0.20	0.38
08181480	36	10	20	10	4.98	4.98	0.20	0.38
08178565	72	5	31	8	78.67	78.67	0.20	0.38
08180800	96	134	253	345	45.8	45.8	0.20	0.20
08181800	84	465	67	445	151.4	151.4	0.20	0.30
08181500	72	109	295	349	97.6	97.6	0.20	0.30
08186000	96	588	71	567	65.73	39.83	0.20	0.25
08183500	96	482	70	480	119.5	119.5	0.20	0.30
08188500	120	930	960	1000	262.91	262.91	0.20	0.20

[1] Original parameter values

[2] Calibrated parameter values

Table 2.3: Comparison of Percent Bias, Mean Absolute Error, and Correlation Coefficient between original and calibrated simulations for the 12 subbasins. The three statistical measures are defined according to Zhang et al. (2004).

Subbasin ID	Bias (%)		MAE (%)		Correlation Coefficient	
	Original	Calibrated	Original	Calibrated	Original	Calibrated
08178880	-14	-27	61	54	0.63	0.69
08180700	215	-1	215	22	0.92	0.93
08185000	54	100	102	105	0.35	0.83
08178700	314	54	350	132	0.39	0.23
08181480	151	8	156	16	0.75	0.78
08178565	285	157	311	225	0.41	0.29
08180800	158	2	158	16	0.95	0.97
08181800	197	20	197	29	0.78	0.92
08181500	208	21	208	31	0.88	0.93
08186000	28	58	44	67	0.69	0.96
08183500	237	27	237	38	0.53	0.90
08188500	447	0	359	54	0.40	0.94

flood polygons display the model output from July 8, 2002 (Day 9 of the storm event). This day was chosen for analysis in order to compare it to the available satellite data during the storm: a Landsat TM flight over Central Texas on July 8, 2002. The Landsat TM data were processed by classifying each grid cell according to its pixel value. Histogram stretching was employed to gain a greater visual difference between pixels. A threshold pixel value was chosen and used to extract inundated cells from non-flood areas, and the result was converted to a vector shapefile in ArcGIS and overlain on the modeled flood polygon.

Results from the Landsat analysis demonstrate that the model overestimates flooding with respect to the Landsat data throughout the reach with the exception of the southernmost portion of the reach, where the model underestimates flooding. While some overestimation of flooding was expected due to the overestimation of runoff volume demonstrated in the modeled hydrographs, there are several other possible causes for the discrepancy between modeled and satellite-derived flood areas. In the Landsat image, dark blue areas signify flooded regions. Cloud shadows are represented by lighter shades of blue. It is often difficult to distinguish between water and cloud shadows on the image; in the extraction analysis, errors may occur when: 1) Similar pixel values cause confusion between flooded regions and cloud shadows, 2) clouds cover a significant portion of cells that are actually flooded and therefore these cells are mistakenly identified as not flooded, and 3) areas of less intense flooding are omitted from the extraction because their values are near or equal to that of the cloud shadows. Time of image collection may also be a significant factor in model error. The Landsat image was collected three days after the storm peak passed over the region; the model overestimation of flooding depicted in Figure 2.6 may reflect inaccuracies in the model's representation of flood dispersal following the storm peak. Analysis of the Landsat data implies that actual infiltration and dispersal of runoff is quicker than that represented in the model.

Research for the regional scale model is ongoing. Due to the highly heterogeneous nature of karstic areas in the San Antonio River Basin, groundwater recharge is difficult to quantify and a general parameterization of infiltration based on soils data such as that originally used by the Soil Conservation Service may be inadequate to portray this heterogeneity. Infiltration coefficients are currently being investigated to reassign curve numbers to the basin grid cells using a more physical basis and more detailed land cover observations. In addition, the feasibility of using various precipitation products to drive a flood model will be investigated by determining the translation of error between input (rainfall data) and output. NEXRAD and other products carry a certain degree of error; since this data drives the model, the question of interest is how this error will affect the final output. The complex hydrological processes in the model may attenuate the error; alternatively, the model may exacerbate the input error. In addition, the author is currently working with several research groups to obtain, process, and ingest other real-time and forecast precipitation products at various resolutions into the model. With the incorporation of different precipitation products, the author hopes to demonstrate the versatility of the model.

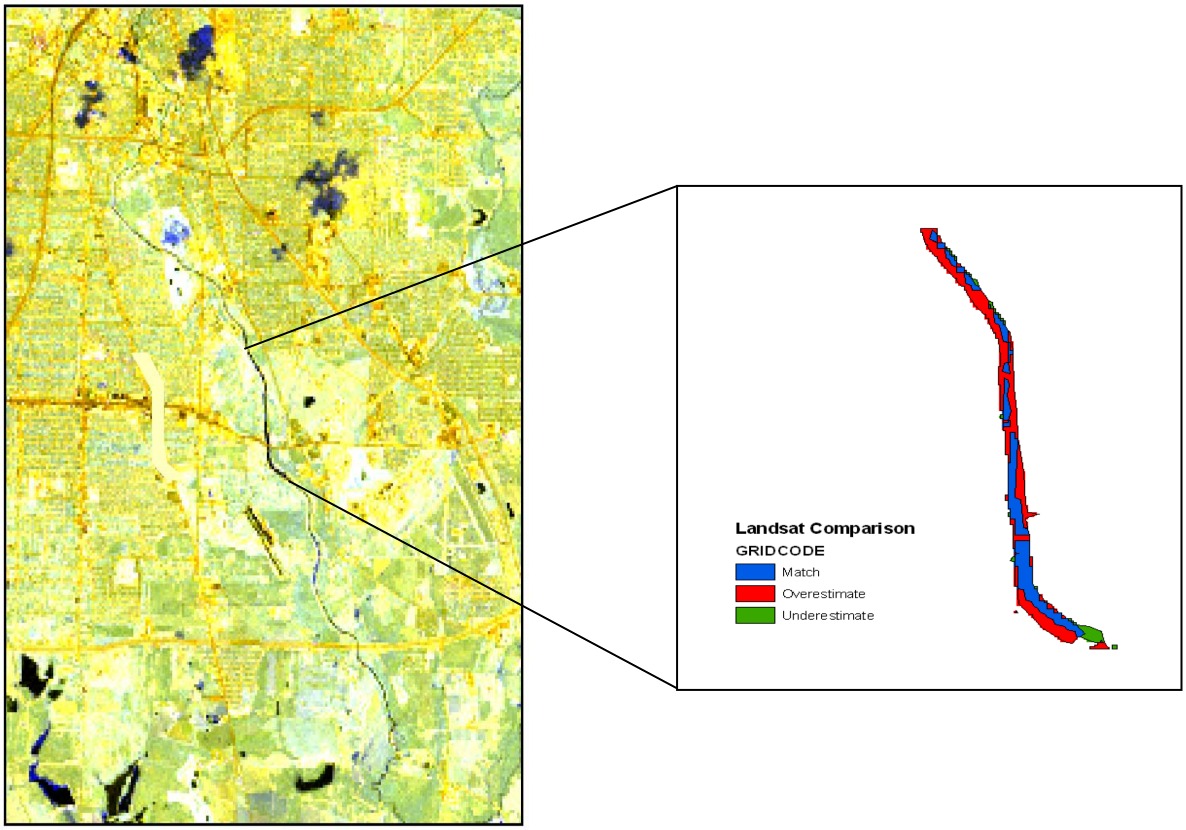

Figure 2.6. Comparison of modeled flood polygon with Landsat TM data. Satellite data was acquired for July 8, 2002; dark areas show inundated regions. The inset figure displays a 2 km long stretch of the San Antonio River, 7.5 km south of downtown San Antonio, located just upstream of subbasin 08178565. The area which both model and satellite data indicate as flooded is shown in blue; red regions demonstrate model overestimation of flooding, and green regions demonstrate areas identified as flooded by satellite data but omitted by the model.

Due to the nature of flood events and the model presented herein, this study has widespread applications in research, operations, and policy. The final result of this study is a complete hydrological and hydraulic model for the San Antonio River Basin, along with a comprehensive GIS database of the area. The model investigates several scientific questions; among these are the feasibility of incorporating rainfall real-time products into a regional flood model, and the testing of a new methodology for deriving floodplain polygons from gridded rainfall. Preliminary model runs have demonstrated a strong potential for successful hydrological modeling at the regional level. In addition, this research has displayed the capability of Map to Map to be extended upward in scale from a small catchment to a large basin. The model can be used a research vehicle for other scientific questions concerning flooding in the San Antonio River Basin region. In addition, the methodology used in this study can easily be applied to other regions of Texas, and can be extended to other areas of the nation as well.

6. CONCLUSION

As all areas of the country increase their level of development, infiltration capacity of the terrain decreases and the threat of flooding becomes even more pronounced. This study presents a methodology and development of a flood model that may be incorporated into both regional hydrological studies and/or a regional alert system for hazard mitigation. The present model will have the capability to perform hydrological studies on a regional scale, and can be incorporated into or provide boundary conditions for local models as well. The successful incorporation of the Map to Map technology at a regional scale demonstrates the versatility of this tool for flood inundation studies at the city, county, and regional levels.

Chapter 3: Assessing the capability of a regional-scale weather model to simulate extreme precipitation patterns and flooding: Central Texas, USA

ABSTRACT

A regional-scale weather model is used to determine the potential for flood forecasting based on model-predicted rainfall. Extreme precipitation and flooding events are a significant concern in Central Texas, due to both the high occurrence and severity of flooding in the area. However, many current regional prediction models do not provide sufficient accuracy at the watershed scale necessary for flood mitigation efforts. The Weather Research and Forecasting (WRF) Model, created with the purpose of improving upon the current Pennsylvania State University / National Center for Atmospheric Research Fifth-Generation Mesoscale Model (PSU/NCAR MM5), is specifically designed for regional resolutions of 1-10 km. Previous research by the authors resulted in the development of a regional-scale prediction system over the San Antonio River Basin, using a GIS database, a hydrologic model, and a hydraulic model. Observed precipitation drives the prediction system; the authors hypothesize that the WRF model has the potential to predict flooding, at a lead time of several days, with an accuracy near that of observed precipitation. Causes of model bias are also investigated, to determine the relative errors caused by model physics, initialization interval, buffer zone and domain size, and small-amplitude random errors. Results show that the Betts-Miller-Janjic cumulus and Lin microphysics schemes, 48-hour initialization interval, and two-domain configuration covering minimal ocean and having a parent-to-nest area ratio of greater than ten best simulates the 2002 storm event. Location errors in rainfall are most significant because of the inherent difficulties in their prediction. Errors in intensity and timing show a more predictable watershed response that may be useful in estimation of streamflow ranges for flood forecasting.

1. INTRODUCTION

Precipitation is the single most difficult and often erroneously modeled parameter in numerical weather models (Wang and Seaman, 1997, Nielson-Gammon et al., 2006). Determining the appropriate resolution that captures both small and large-scale processes is vital to accurately representing storm events. For example, neglecting sub-grid-scale variability of precipitation has been shown to result in an underestimation of precipitation and runoff, and consequentially an overestimation of evapotranspiration (Wang et al., 2005). Mitigation decisions based on local-scale engineering models may not give the relative contributions and responses of runoff to rainfall over all subbasins in the entire watershed. A nested regional model provides a realistic method for modeling flood events at the watershed scale by capturing synoptic scale triggers over the entire domain and downscaling to capture mesoscale factors over the region of interest. This approach has proved successful at various resolutions (Liang et al., 2004a, Smedsmo et al., 2005).

Systematic biases still exist in regional models. Major causes of model bias are investigated in this study. Since causes of bias vary with the specific region and climate of interest, a regional model must be adapted for each application (Giorgi and Mearns, 1999). Biases arise from model physics, domain and buffer zone treatments, initial and boundary conditions, and small-amplitude random errors.

The implementation of various physics schemes causes a large variation in forecast output (Zhang et al., 2006), especially the choice of cumulus scheme (Gallus and Segal, 2001). The particular skill of a cumulus scheme in simulating rainfall is dependent upon the region and storm being modeled (Giorgi and Mearns, 1999). The Grell-Devenyi (GD) scheme has displayed widespread skill in simulating precipitation (Giorgi and Shields, 1999, Warner and Hsu, 2000, Xu and Small, 2002, Zhang et al., 2006). However, several studies have shown the Kain-Fritch (KF) scheme to produce realistic precipitation over the North American Monsoon region (Gochis et al., 2002, and Leung et al., 2003, Liang et al., 2004a); other research has demonstrated the strength of the Betts-Miller Janjic (BMJ) scheme to produce accurate forecasts (Baik et al., 1991, Vaidya and Singh, 2000). Emanuel and Zivkovic-Rothman (1999) found that the BMJ scheme performs consistent with observations for relative humidity from the surface up to 500 mb. Jankov and Gallus (2004) found that neither the BMJ nor the KF scheme accurately reproduced mesoscale convective systems (MCS) in the Upper Midwest, with the BMJ scheme consistently overestimating and the KF scheme underestimating rainfall.

Cloud microphysics is the second parameterization most important in the production of precipitation in WRF. Cloud microphysics schemes vary widely, from a simple warm-cloud scheme (Kessler, 1969) to a complex four-class ice scheme (Ferrier, 1994). The scheme most suited to the model application varies with location; for example, the Lin scheme is appropriate for hail-bearing storms in the Midwest (Smedsmo et al., 2005).

Emanuel and Zivkovic-Rothman (1999) assert that correct microphysics is integral to determining cumulus convection and hence precipitation. They postulate that re-evaporation of condensed water, currently not included in most parameterizations, allows correct estimates of convective moistening. Their cumulus parameterization controls entrainment and detrainment by allowing the level of natural buoyancy to vary depending on moisture levels in cloud air. Both BMJ (Janjic, 1994) and Emanuel's scheme are comparable to observations; other schemes tested were less so.

Errors in the driving initial and boundary conditions can cause large variation in forecast output. Liang et al. (2004a) found large uncertainties in boundary conditions, mostly over oceans and other areas lacking complete data, contributed greatly to model error. The use of the National Centers for Environmental Prediction-National Center for Atmospheric Research (NCEP-NCAR) reanalysis caused less sensitivity to model domain when compared to the European Centre for Medium-Range Weather Forecasts (ECMWF) reanalysis (Liang and Kunkel, 2001). The initialization interval is important because of the spinup time needed for model adjustment, as well as the inability of most weather models to accurately forecast beyond several days.

The size of the model domains and the interaction between nested domains greatly impact forecasts. If the domain edges are too close to the area of interest, edge effects may cause inaccuracies in the forecast. For example, Seth and Giorgi (1998) found that small domains caused unrealistic responses in the inner domain that were inconsistent with large-scale forcing. Location of domain edges must be chosen so that important regional meteorological features can be resolved, and the edges must be located away from areas where reanalysis inaccuracies exist; parent and nest domains should be spaced far enough apart to avoid edge distortions (Liang and Kunkel, 2001). The boundary zone width may also contribute to error. Increasing the width across which dynamical relaxation of boundary conditions occurs, or nudging over the entire domain, may help preserve large-scale waves and hence reduce errors due to domain size (Juang and Hong, 2001).

The major objectives of the present study surround the following questions: 1) How well does WRF model the synoptic setting which produced the 2002 storm event?; 2) What are major causes of model bias in terms of physics, initialization, domain, and small-amplitude errors?; 3) What types of precipitation error propagate most strongly into streamflow: magnitude, location, or timing? How do these each affect flood forecast outcomes? In the next section, an overview of the 2002 storm meteorology is presented. Section 3 discusses background information on the driving datasets and WRF model structure, section 4 presents experimental methods and results, and section 5 discusses the conclusions and implications of this research.

2. METEOROLOGY OF THE 2002 STORM EVENT

The high frequency of flooding in Texas results from a unique juxtaposition of meteorological factors including moisture influx from the Gulf of Mexico, easterly waves moving across the area, and orographic uplift from the Balcones Escarpment (Hirschboeck, 1987). In fact, Texas has recorded some of the greatest precipitation intensities in the world, for storms with durations up to 24 hours (Patton and Baker, 1977). Although storm events over Central Texas are generally controlled by large-scale anomalies in atmospheric circulation patterns, the interaction of these anomalous behaviors with local and mesoscale processes, such as topographic influences and the location of mesohigh outflow boundaries, determines whether or not a flood event occurs in any given region. This combination of factors at a variety of scales complicates numerical weather modeling, causing model output to become highly sensitive to changes in model structure and parameterizations. Extreme storms in Texas may be triggered by tropical cyclogenesis, cyclonic dissipation, frontal processes, orographic lifting, or a combination of several local and synoptic-scale events. Most extreme storm events over Texas show large-scale meteorology significantly different from climatology at the 95% significance level (Nielson-Gammon et al., 2006). The summer 2002 storm was related to a deep upper-level trough that became stationary over South-Central Texas. Early on in the storm's life span, upper level triggers dominated, possibly reinforced by local factors. Later on, mid-level triggers became more important. Much of the subsequent discussion is based upon the work of Nielson-Gammon et al. (2006), who performed a compositing analysis to determine typical meteorological factors present during Texas storms and particularly the summer 2002 event.

At the 850 mb level, strong trade winds blow across the Yucatan toward Mexico and Texas, bringing moisture into the area. Decreasing wind speed from the Gulf of Mexico to the Great Plains implies low-level moisture convergence over the region. This is most easily seen as a deceleration of winds over eastern Texas. However, this deceleration was less prominent in the 2002 storm compared to other large historical storm events over Texas. Observations several days before the onset of heavy rainfall still show strong southeasterlies over the Gulf of Mexico, prior to their landfall in Texas. Following peak rainfall, observations show weaker winds and less deceleration over Texas.

Mid-level development (500 mb) is dominated by cyclonic circulation in the form of a north-south elongated trough over south Texas. This cyclonic circulation causes a high potential vorticity (PV) anomaly that directs moisture away from Central America and into Texas. Precipitation efficiency is increased by southerly winds blowing into Texas from the Gulf of Mexico. A strong low-level jet (LLJ) feature, defined by Bonner (1968) as a low-level local maximum in the vertical wind profile, is generally observed in Texas nontropical storms during September and October. In summer storm events, the strongest LLJ features are located more to the north in the central Great Plains; the southerly winds present during the 2002 event do not show such localized maxima and are better referred to as a southerly wind event (SWE; Mitchell et al.,1995). However, similar to the Great Plains LLJ, the strong SWE transports vast amounts of moisture into the region and plays a large role in precipitation formation during the storm.

The major upper level contributor, near the tropopause at 200 mb, is a high potential vorticity (PV) anomaly that produces upper-level divergence over Texas, curving anticyclonically to the east as flow moves outward from convective updrafts. This causes an upper-level ridge to develop over the southeastern states, which further prevents movement of the trough. New PV anomalies are continuously created from cutoff lows to the west, creating a cycle of PV formation and destruction that contributes to instability and upward airflow over Texas. As the storm wears on, condensation heating triggers the formation of a quasi-stationary PV vortex in the lower atmosphere at 500mb, further strengthening rainfall intensity by promoting mid-level ascent .

Locally, mechanical lifting is thought to be a factor in storm evolution, demonstrated by the location of Balcones Fault Zone (BFZ) in relation to heavy rain concentration areas. Southeasterly to easterly winds at the 850 mb level over the region imply upward motion due to topography (Patton and Baker, 1977). Many convective cells and high precipitation accumulations were observed in 2002 along the BFZ. In addition to trigger factors for heavy rainfall, basin flooding is aggravated by the shallow soils, karstic terrain, bedrock channels, and increasing levels of urbanization over the San Antonio River watershed.

3. REANALYSIS DATASET AND METEOROLOGICAL MODEL

a. North American Regional Reanalysis

Initialization and boundary conditions were interpolated from the NCEP North American Regional Reanalysis (NARR, Mesinger et al., 2006). NARR is a comprehensive hydrometeorological dataset used to drive regional scale models. Based on the Global Reanalysis (GR) Project that ran 30 years of simulations using the Eta model and assimilated observations, NARR assimilates observational data for analysis, boundary conditions, and execution of the Eta model. Observations taken from the GR include temperature, moisture, and winds, and are derived from rawinsondes, dropsondes, pibals, aircraft, surface, and cloud drift datasets. The Regional Reanalysis improves upon the GR by assimilating datasets such as CONUS (with PRISM) for precipitation over land and the Climate Prediction Center's Merged Analysis of Precipitation (CMAP) for oceanic precipitation, TOVS-1B radiances for winds over oceans, and sea-surface temperatures (SST) from the 1-degree Reynolds dataset. Locations of tropical cyclones are used for blocking of CMAP precipitation, since CMAP is often inaccurate near the centers of storms and areas of intense precipitation. The NCEP land-surface dataset is merged with that of the Model Development Laboratory (MDL) to improve observational coverage. Observations which resulted in poor model accuracy are omitted from the Regional Reanalysis. Daily climatologies of baseline snow-free albedo and green vegetation fraction are used to initialize NARR daily. Additionally, several fixed fields exist in NARR; these include land mask, vegetation/soil type, and surface roughness.

Data are output as 3-hourly files on a 32 km Eta grid with 29 pressure levels, distributed on a Lambert conformal grid. Data are available for free download from the NCAR website in GRIB format. The Regional Reanalysis appears to correctly capture important elements of the hydrologic cycle; NARR streamflow output compares well with measured discharge, and has been shown to perform better than the previous ERA-40 reanalysis (Dery et al., 2005). Although simulations with NARR have been unable to completely balance the moisture budget, summer flux convergence over Texas and the northern Gulf of Mexico is much better represented with NARR than with previous global reanalyses (Nigam and Ruiz-Barradas, 2006).

b. WRF model

WRF version 2 (Michalakes et al., 2005), a nonhydrostatic, mesoscale weather model developed at NCAR, is used in this study. The WRF model structure has many similarities to the MM5 model, but also includes new and modified parameterizations, particularly in regard to cumulus parameterization. Initial conditions from NARR drive the model at the first time step, and boundary conditions (also from NARR) are assimilated continuously at hourly time steps. The preliminary WRF configuration used in this study consists of a 12-km outer domain with a horizontal resolution of 105 x 105 grid points, and a 4-km inner domain with a horizontal resolution of 97 x 94 grid points. The area of interest for flood modeling, the San Antonio River Basin, lies in the center of the inner domain; for reference, the basin area accounts for approximately 1/15 of the inner domain area (Figure 3.1). Both domains have 31 variably-spaced, vertical grid cells in sigma coordinates, $\sigma = (P - P_t)/(P_s - P_t)$, with model top at 100mb. Ten levels reside at or below the planetary boundary layer (1.5 km); high vertical resolution in the boundary layer is thought to improve simulation of the LLJ or SWE (Ting and Wang, 2006), which as mentioned previously is important for moisture transport and storm generation. Model physics are variable and described further in the following section.

The procedures for completing a regional forecast and processing output are as follows:

(1) Apply the WRF Standard Initialization (WRFSI) codes to define simulation domain, define terrain and land cover data over the domains, de-grib NARR files of meteorological data, and interpolate NARR data from 32 km to 12 km and 4 km for domains 1 and 2, respectively.

(2) Execute WRF: initialize model at 0000 UTC 30 June 2002 and integrate for 11 days through the end of the storm, using a maximum time step of 90 seconds (see subsequent sections for alternate initialization configurations).

(3) Process output. After each WRF model run is complete, the NetCDF rainfall grids are processed and utilized in the hydrologic model through a series of conversion steps: conversion of NetCDF to ASCII files, conversion of ASCII to GIS grids, grid definition and reprojection, conversion back to ASCII, and conversion to HEC's Data Storage System (DSS) file format.

(4) Forecast streamflow. The hydrological model (HEC-HMS; HEC, 2000) ingests the precipitation grids and outputs streamflow time series at hourly time steps.

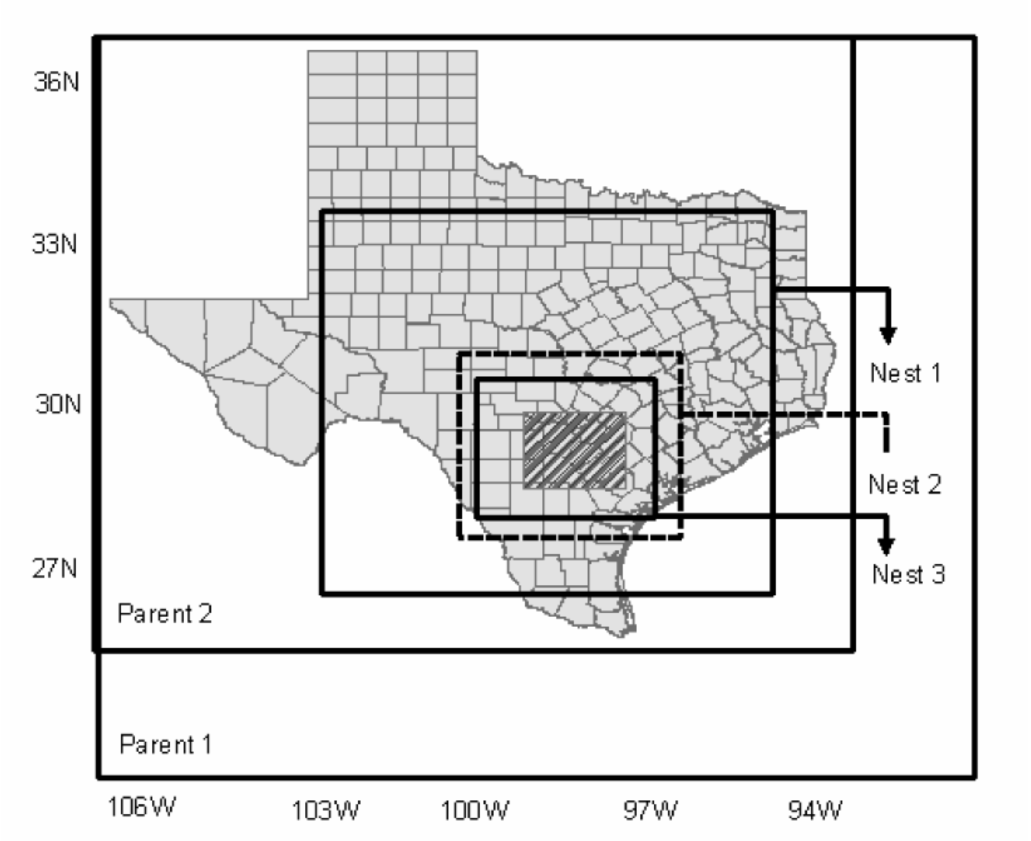

Figure 3.1. Model domains. Control domain configuration includes parent 2 and nest 2 (other domains are referenced in section 4). The region of interest for forecasting (San Antonio River Basin area) is represented by the hatched region.

4. EXPERIMENTAL DESIGN AND RESULTS

a. Physics parameterizations

The WRF model contains multiple options for physics parameterizations. Adjustable physics components include microphysics, cumulus parameterization, longwave radiation, shortwave radiation, boundary layer turbulence (PBL), surface layer, land-surface parameterization, and subgrid scale diffusion. Warm-season precipitation output is especially sensitive to choice of cumulus scheme, and moderately sensitive to microphysics, radiation, and boundary layer scheme (Wang and Seaman, 1997, Liang et al., 2004b, Nielson-Gammon et al., 2006). Warm season convective precipitation is the most difficult variable to model accurately (Olson et al., 1995, Nielsen-Gammon et al., 2006), possibly due to the importance of initial precipitation peak locations in providing feedback mechanisms that dictate the subsequent event evolution. For this study, sensitivity is tested using various combinations of schemes (approximately 40 different combinations); only those combinations which produce significant precipitation are described in this paper. The physics options are combined as shown in Table 3.1, and included the Grell-Devenyi, Kain-Fritsch, and Betts-Miller-Janjic cumulus schemes, Kessler, Lin, Eta, and WRF Single Moment 3-Class (WSM) cloud microphysics, Rapid Radiative Transfer Model (RRTM) and Eta longwave radiation, and Dudhia, Goddard, and Eta shortwave radiation. Several studies have suggested that at high resolutions (< 5 km), a regional model may simulate convective processes equally or better than explicit implementation of convection (Belair and Mailhot, 2001, Smedsmo et al., 2005); hence, the effect of removing convection parameterization from the nested domain is also studied. Each model is run for the entire 11-day storm event using only a single initialization at day 1 of the storm.

Comparisons between observed and modeled rainfall are performed by upscaling from the fine resolution WRF output to the coarser resolution Higgins observed dataset (Higgins et al., 2000). The Higgins dataset is derived from rain gauge records from approximately 2500 stations on a 0.25° longitude by 0.25° latitude grid (about 32 km^2). Regional averages of WRF precipitation output are computed for 32 km^2 regions aligning with the Higgins rainfall grid that intersect the study basin, for a total of twenty-five grid cells. These grid regions are the comparison points for all subsequent analyses.

Precipitation is found to be most sensitive to the cumulus and microphysics schemes used. In Figures 3.2-3.7, the San Antonio River watershed and its gages are superimposed on the WRF rainfall map for the purpose of identifying areas of large errors across the basin. The Kain-Fritch scheme (Figures 3.2 and 3.5) produces spurious locations of high precipitation surrounding the basin, especially in combination with the RRTM shortwave radiation scheme, while underestimating precipitation inside the watershed. The Grell-Devenyi cumulus scheme (Figures 3.4 and 3.7) largely underestimates precipitation, completely missing the large peak over San Antonio. Removing convection from the nested domain, regardless of the cumulus scheme used, results in a gross underestimation of rainfall over the basin (Figure 3.2d). Variation in both the longwave and shortwave radiation schemes appears to have insignificant effects on precipitation forecasts over the basin (Figure 3.3d; others not shown). Overall, the Betts-Miller-Janjic cumulus scheme (Figures 3.3 and 3.6) most accurately simulates precipitations and subsequent river flooding over the SAB; however, this scheme produces a wider swath of peak precipitation than observed on July 3, accounting for the large errors in lower portions of the basin on that day (Table 3.2). Results from experiment MP2CU2 most closely match the observed mean and standard deviation of rainfall for the basin. Despite the emphasis on correct microphysical properties in modeling deep convection (Fritsch and Carbone, 2004, Smedsmo et al., 2005), model runs using varying microphysics schemes produce less striking differences in precipitation. In Figure 3.2b, the Kessler scheme underestimates rainfall over much of the basin, especially the lower portions. In the WSM scheme (Figure 3.2e), the peak rainfall signal is much weaker than observed. The Lin et al. (Figure 3.2c) and Ferrier (Figure 3.2f) schemes produce more accurate rainfall over all areas of the basin, despite both having a peak that is located southwest of the observed rainfall peak. Additional simulations demonstrated that the WRF model is highly sensitive to the atmospheric model time step; in fact, precipitation intensity increased over the SAB for increased time step. The results shown use a consistent time step representing the smallest time step at which all experiments remained stable. It should be noted that in later experiments that use only the BMJ / Lin physics combination, time step is increased to 90 seconds; WRF results correspondingly demonstrate a greater definition of peak rainfall area.

Table 3.1. Various combinations of physics parameterizations used to run the WRF model in this study. Experiments are named based upon the different schemes used in each: MP, CU, NC, and SW refer to microphysics, cumulus, no convection, and shortwave radiation schemes, respectively.

Experiment	Microphysics	Cumulus	Radiation	Explicit Nest Convection
MP1CU1	Kessler	KF	Dudhia	Yes
MP1CU2	Kessler	BMJ	Dudhia	Yes
MP1CU3	Kessler	GD	Dudhia	Yes
MP2CU1	Lin et al.	KF	Dudhia	Yes
MP2CU1NC	Lin et al.	KF	Dudhia	No
MP2CU2	**Lin et al.**	**BMJ**	**Dudhia**	**Yes**
MP2CU2SW2	Lin et al.	BMJ	Goddard	Yes
MP2CU3	Lin et al.	GD	Dudhia	Yes
MP3CU1	WSM	KF	Dudhia	Yes
MP3CU2	WSM	BMJ	Dudhia	Yes
MP3CU3	WSM	GD	Dudhia	Yes
MP4CU1	Ferrier	KF	Dudhia	Yes
MP4CU2	Ferrier	BMJ	Dudhia	Yes
MP4CU3	Ferrier	GD	Dudhia	Yes

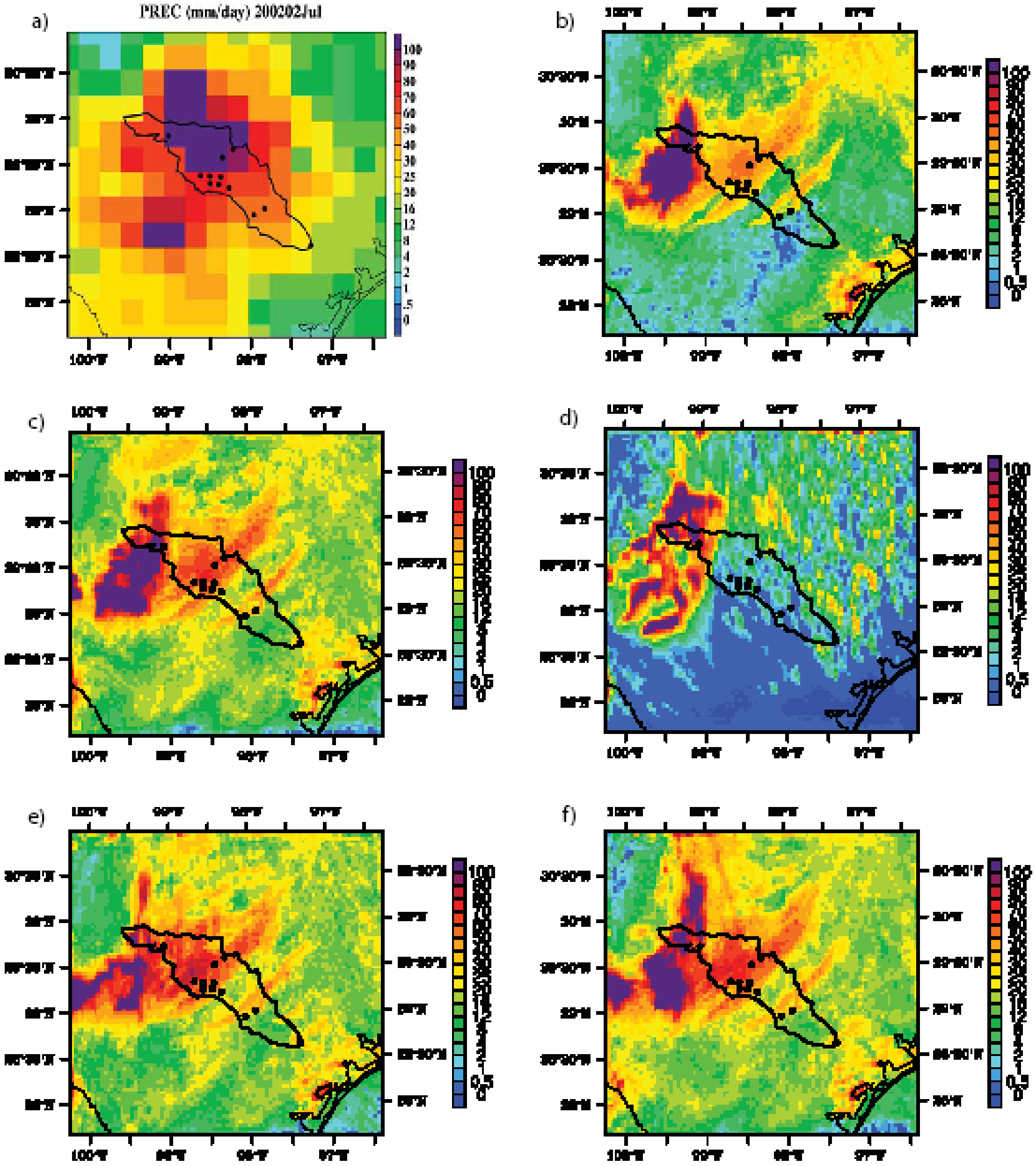

Figure 3.2. Total daily precipitation (mm day^{-1}) for July 2, 2002 compared between a) observations and WRF output using the Kain-Fritsch cumulus parameterization, and various microphysics: b) Kessler; c) Lin et al.; d) Lin et al. with no convection applied to nest domain; e) WSM; f) Ferrier. All model runs shown use RRTM shortwave radiation unless otherwise specified.

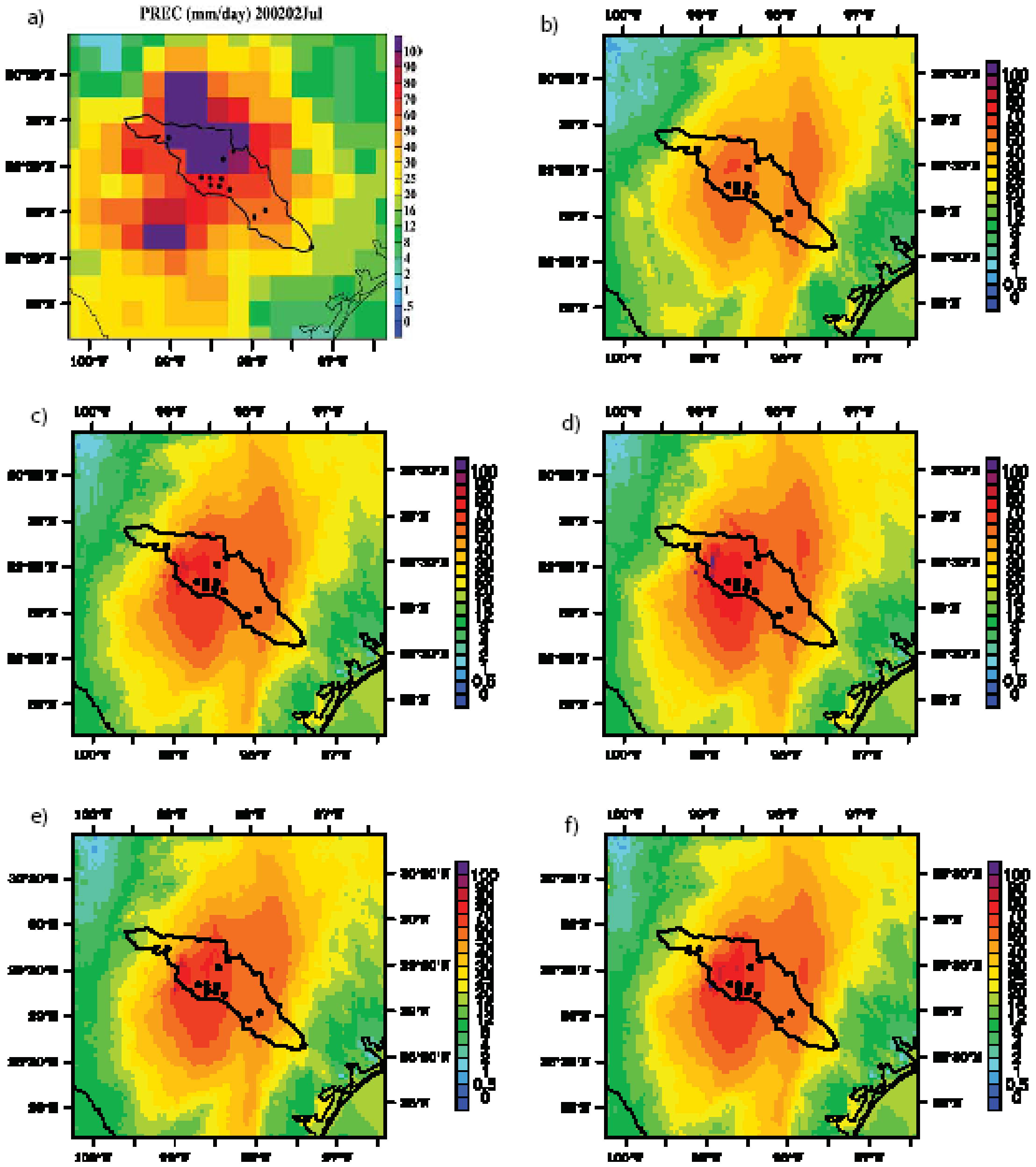

Figure 3.3. Total daily precipitation (mm day^{-1}) for July 2, 2002 compared between a) observations and WRF output using the Betts-Miller-Janjic cumulus parameterization, and various microphysics: b) Kessler; c) Lin et al.; d) Lin et al. with Goddard short wave radiation; e) WSM; f) Ferrier.

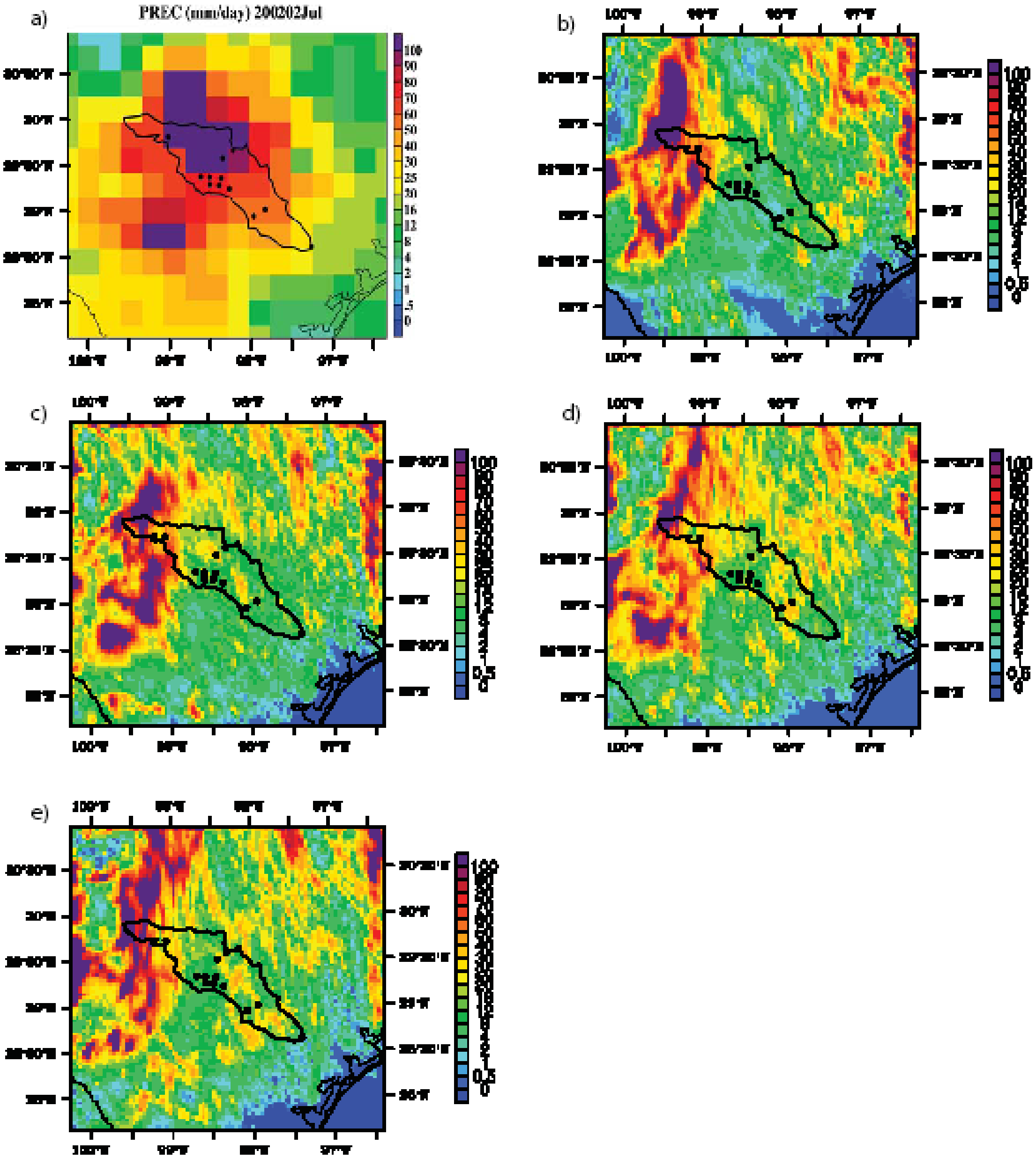

Figure 3.4. Total daily precipitation (mm day^{-1}) for July 2, 2002 compared between a) observations and WRF output using the Grell-Devenyi cumulus parameterization, and various microphysics: b) Kessler; c) Lin et al.; d) WSM; e) Ferrier.

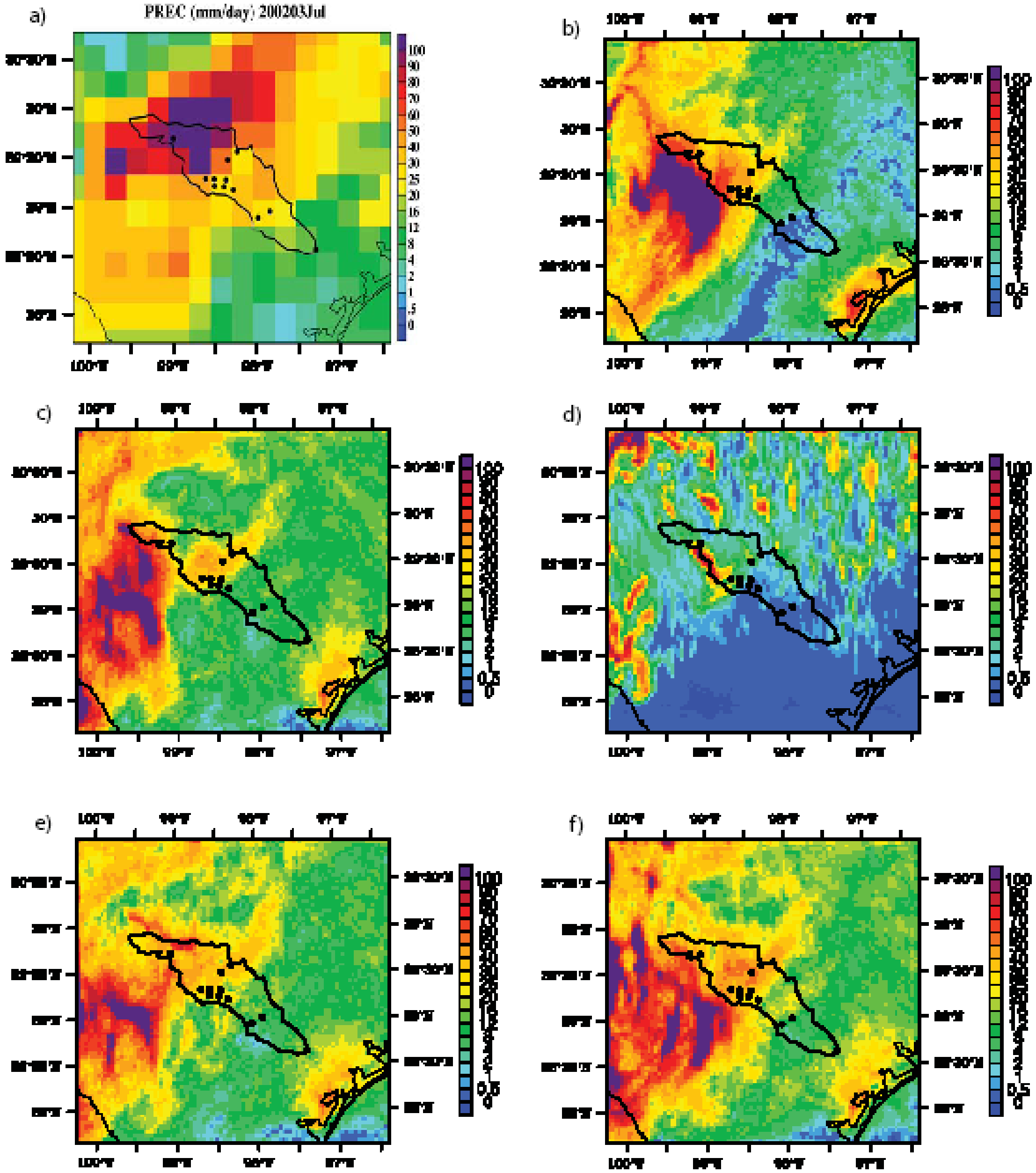

Figure 3.5. Total daily precipitation (mm day^{-1}) for July 3, 2002 compared between a) observations and WRF output using the Kain-Fritsch cumulus parameterization, and various microphysics: b) Kessler; c) Lin et al.; d) Lin et al. with no convection applied to nest domain; e) WSM; f) Ferrier.

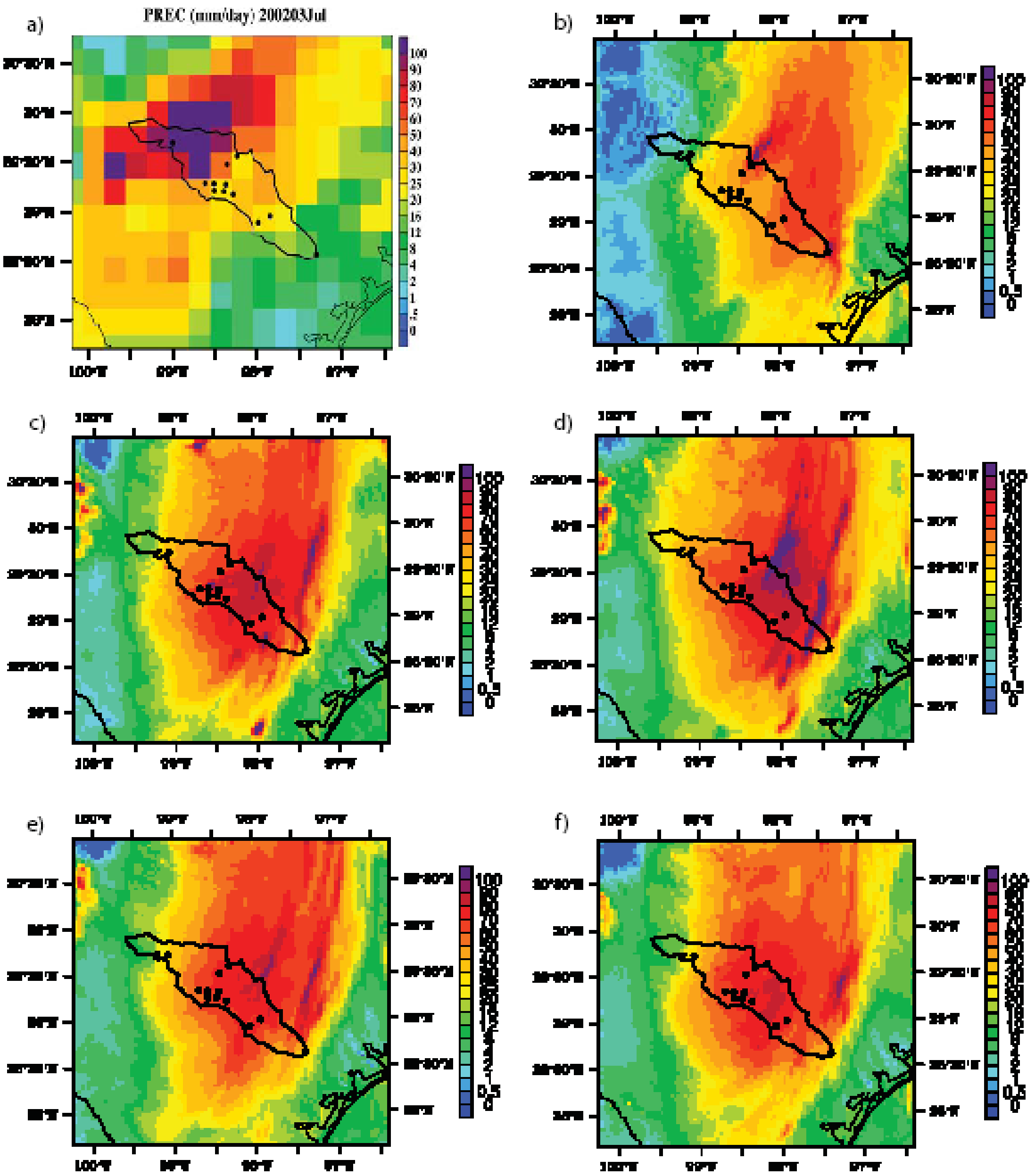

Figure 3.6. Total daily precipitation (mm day^{-1}) for July 3, 2002 compared between a) observations and WRF output using the Betts-Miller-Janjic cumulus parameterization, and various microphysics: b) Kessler; c) Lin et al.; d) Lin et al. with Goddard short wave radiation; e) WSM; f) Ferrier.

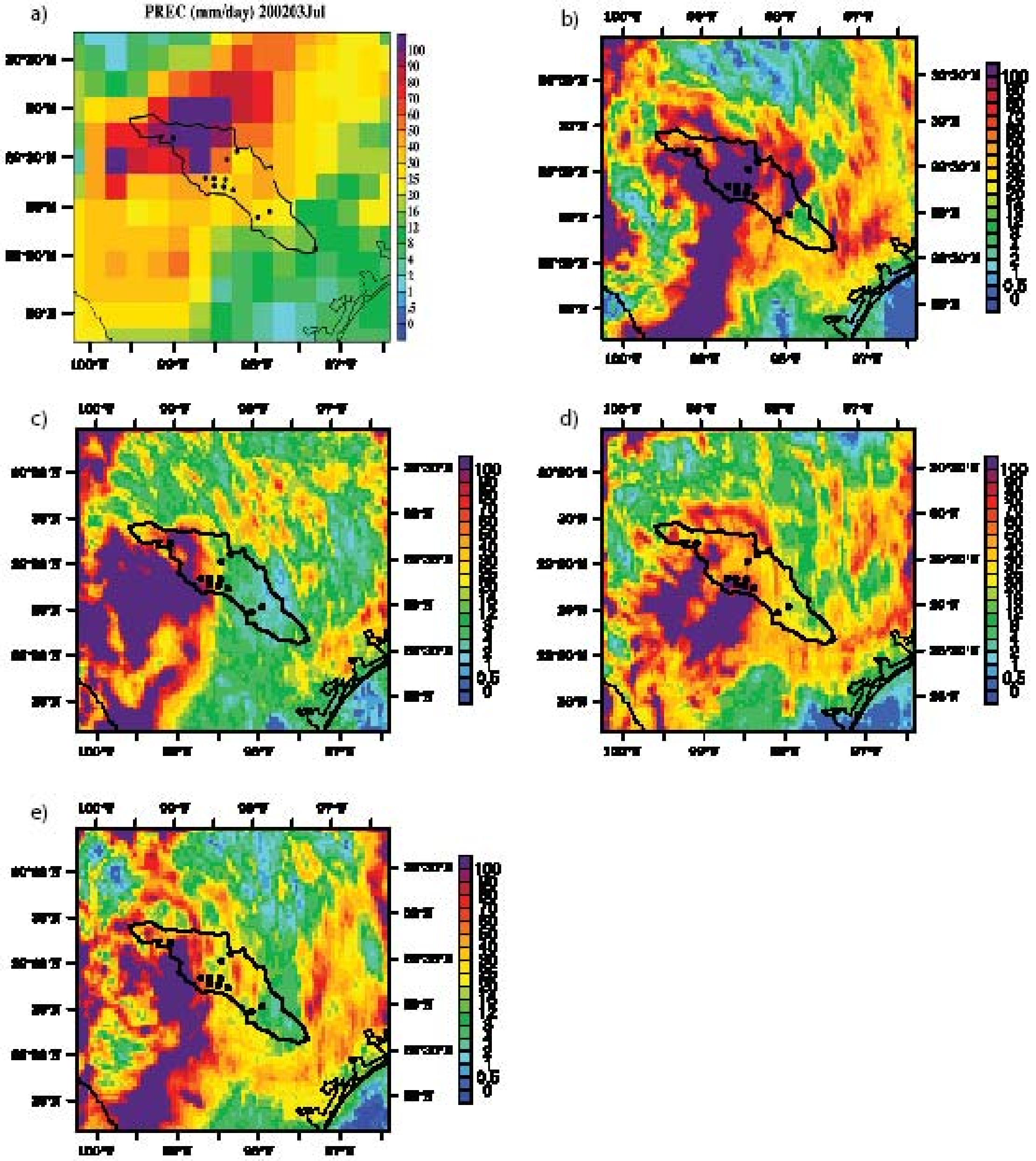

Figure 3.7. Total daily precipitation (mm day^{-1}) for July 3, 2002 compared between a) observations and WRF output using the Grell-Devenyi cumulus parameterization, and various microphysics: b) Kessler; c) Lin et al.; d) WSM; e) Ferrier.

Table 3.2. Mean and standard deviation of precipitation over the San Antonio River Basin during the 48-hour period of peak rainfall, and correlation with observations for each of the physics configurations used in this study. Mean absolute error is shown for both peak days over the upstream, midstream, and downstream portions of the watershed.

	Combined July 2/3			MAE[1] (%), July 2			MAE[1] (%), July 3		
Experiment	Mean(mm)	SD	R	Upper	Middle	Lower	Upper	Middle	Lower
Observed	64	32	-	-	-	-	-	-	-
MP1CU1	22	17	-0.18	69	65	52	68	54	56
MP1CU2	36	16	-0.41	69	36	1	82	23	252
MP1CU3	36	40	-0.36	44	85	67	53	33	98
MP2CU1	25	46	-0.39	61	55	42	73	53	25
MP2CU1NC	13	10	0.27	69	87	83	86	83	72
MP2CU2	**70**	**32**	**0.17**	**69**	**36**	**1**	**4**	**285**	**364**
MP2CU2SW2	49	28	0.15	65	29	10	56	86	374
MP2CU3	24	11	0.19	59	77	62	71	38	9
MP3CU1	27	6	0.60	62	53	41	68	40	9
MP3CU2	45	17	-0.32	69	33	6	61	77	313
MP3CU3	28	9	0.47	55	71	50	67	20	4
MP4CU1	30	9	0.52	52	52	41	67	34	3
MP4CU2	45	16	-0.24	68	33	7	57	74	278
MP4CU3	29	20	0.28	46	74	53	56	44	31

[1] Mean Absolute Error

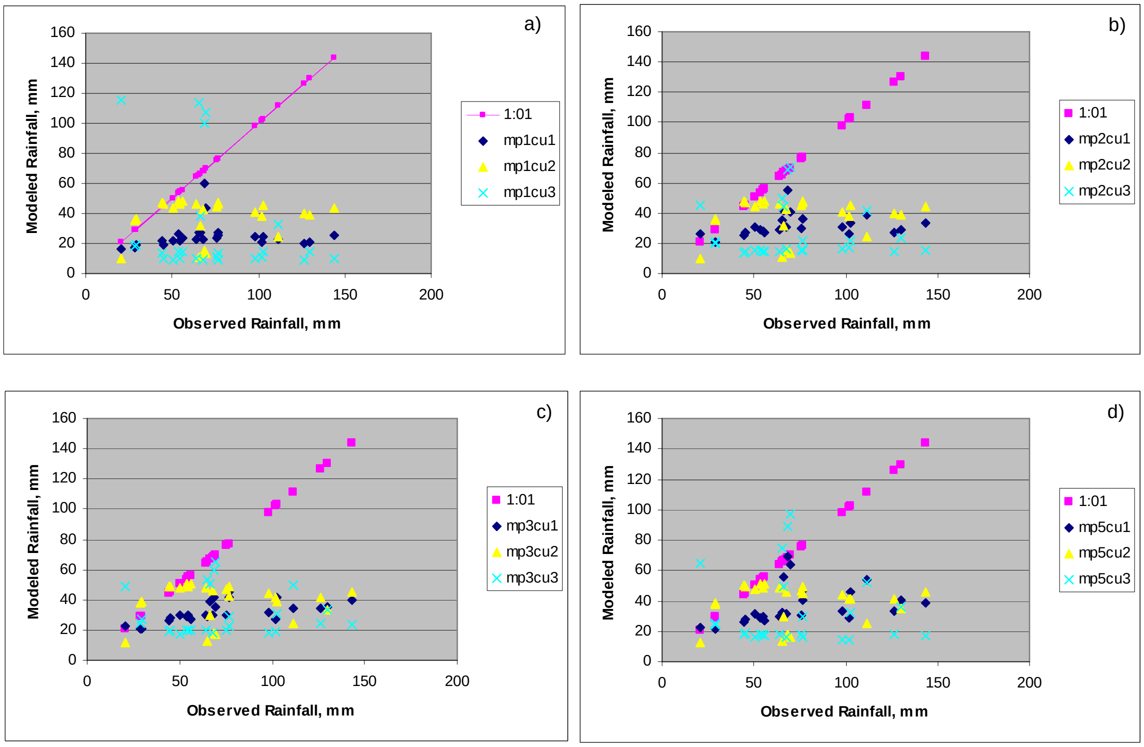

Figure 3.8. Comparison of daily precipitation for July 2, over 25 grid cells for various experiments. A 1:1 line (perfect match with observations) is drawn for reference.

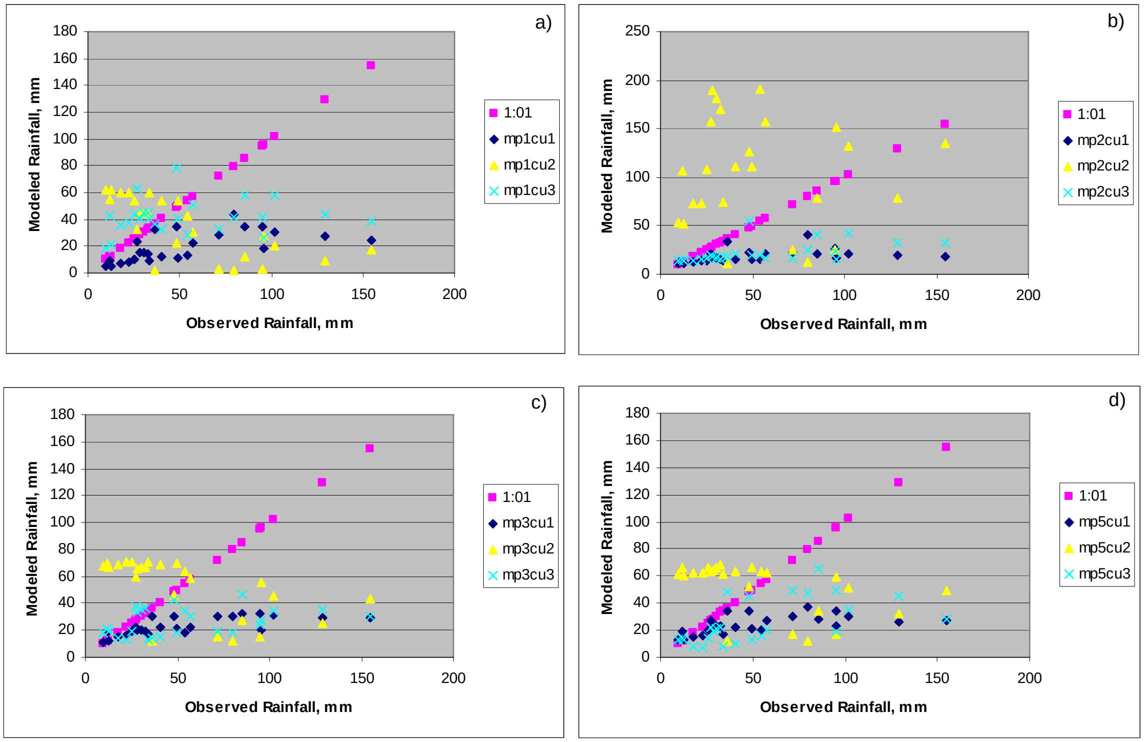

Figure 3.9. Comparison of daily precipitation for July 3, over 25 grid cells for various experiments. A 1:1 line (perfect match with observations) is drawn for reference.

In Figures 3.8 and 3.9, it is clear that most physics combinations underestimate precipitation during the peak days of July 2 and July 3. Experiments utilizing the KF cumulus scheme consistently underestimate rainfall for both days over nearly the entire basin. Experiments with the BMJ scheme tend to underestimate rainfall for July 2 and overestimate rainfall for July 3, which may be attributed to error in the timing of convection. However, the BMJ scheme produces some of the most accurate values over the central basin region. This region contains the city and suburbs of San Antonio, which may imply that the BMJ scheme best simulates the urban heat island effect on precipitation. Experiments using the GD cumulus scheme show sporadic results, with the highest accuracy over the southern portions of the basin on July 3. Daily totals averaged over the upper, middle, and lower basin areas (not shown) further support these characteristics. Physics configuration for the succeeding experiments are as follows: Lin microphysics, BMJ cumulus parameterization, Janjic Eta surface layer scheme, Rapid Update Cycle (RUC) land-surface model, Mellor-Yamada-Janjic Eta boundary layer physics, and RRTM (longwave) and Dudhia (shortwave) radiation.

b. Initialization interval

Decision-making in flood management demands a high accuracy of weather model output, and many weather forecasts are considered impractical for use beyond 36 hours. The potential performance of WRF in modeling future storm events is investigated in this study; in the following experiments, the effect of forecast length on convective rainfall output is addressed through variation of the initialization interval in WRF.

The WRF model is initialized at intervals of 24 hours (1 day), 48 hours (2 days), 72 hours (3 days), 120 hours (5 days), and 264 hours (11 days, covering the entire storm length). A series of model runs are completed with each interval as necessary to cover the 11-day storm (Table 3.3). For example, the 24 hour initialization experiment consists of 11 runs, the 48 hour initialization consisted of 6 runs, etc. Results from the model runs are combined for each interval length and plotted for the entire storm length. Precipitation output grids are then run through the hydrologic model and streamflow output compared between experiments.

Comparisons between precipitation output for different initialization intervals are shown in Figures 3.10-3.15. Experiment results demonstrate that a 48-hour initialization best reproduces observed rainfall (Figure 3.14). The 24-hour run misses or underestimates several precipitation peaks, while the longer forecasts severely underestimate precipitation, and in some cases produce spurious areas of precipitation. The reason that an intermediate initialization interval is most accurate in representing rainfall is likely due to adjustment time in the model, as the model integrates the NARR initial boundary conditions (IBCs) and begins producing grid variables on its own (i.e., the time needed for the model to reach equilibrium). In this particular case, adjustment time may also include adjustment between differences in the Eta land-surface model used in the NARR data and the RUC land-surface model used in the WRF model runs for this experiment.

Table 3.3. Initialization intervals used for WRF experimental runs.

Experiment	Initialization Interval (hr)	# of model runs
1D	24	11
2D	48	6
3D	36	4
5D	120	3
11D	264	1

Table 3.4. Precipitation mean, standard deviation, and correlation values for WRF experiments in which initialization is varied.

Experiment	Storm Mean (mm day^{-1})	Daily Deviation	Correlation with Observations (%)
Observed	31.6	13.6	-
1D	38.8	10.8	0.47
2D	66.8	23.1	0.63
3D	33.4	7.7	0.27
5D	20.6	4.46	0.04
11D	19.9	4.4	0.17

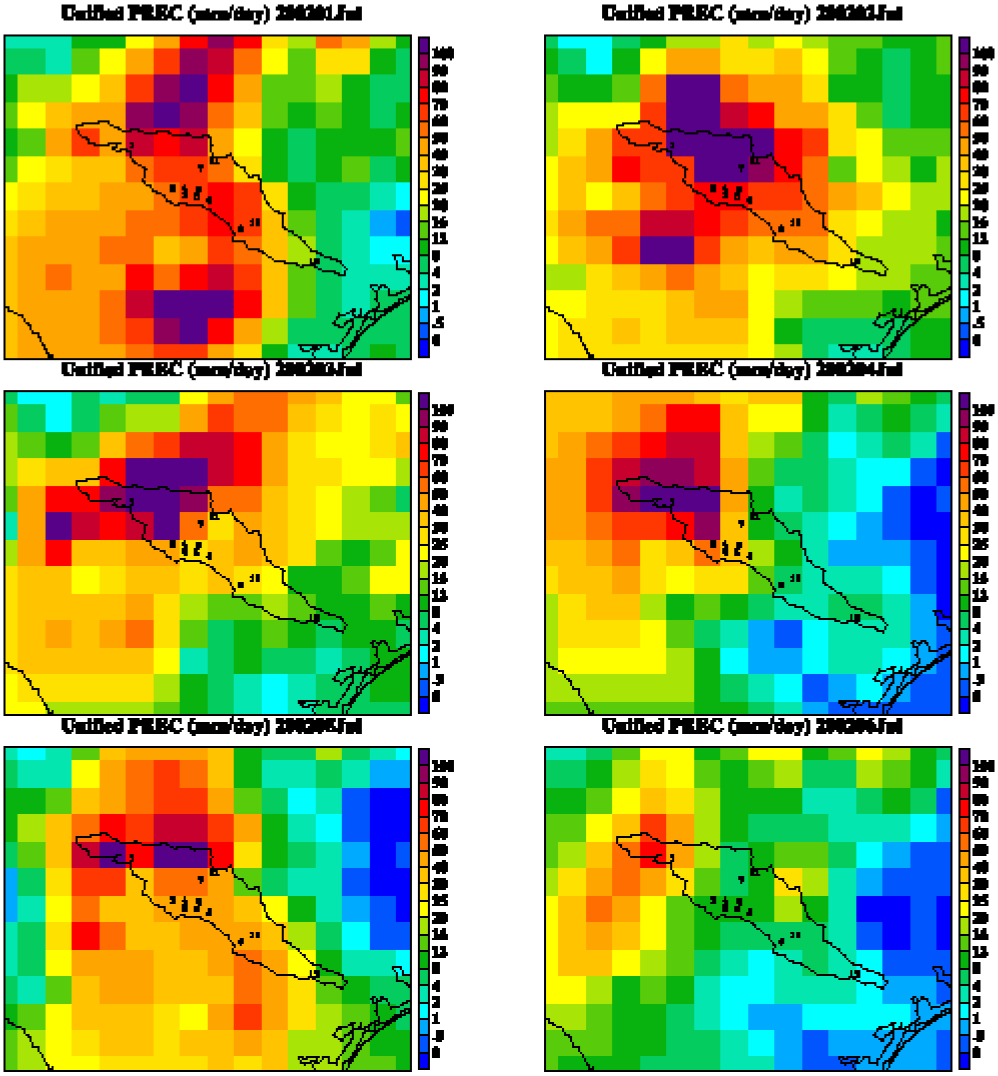

Figure 3.10. Observed total daily precipitation (mm day^{-1}) from Higgins dataset. Days 2-6 of the storm event area shown; upper left = July 1; upper right = July 2; middle left = July 3; middle right = July 4; lower left = July 5; and lower right = July 6.

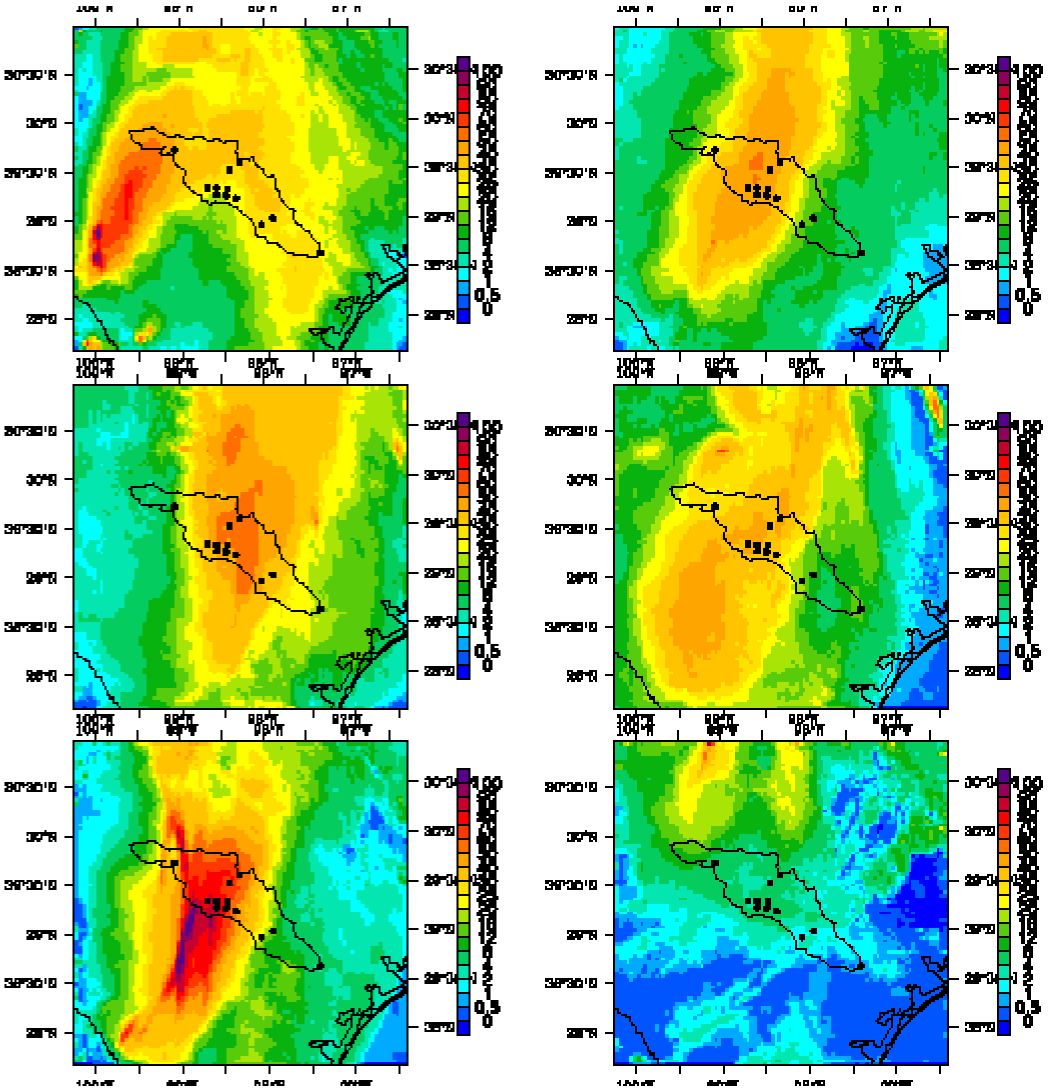

Figure 3.11. Total daily precipitation (mm day^{-1}) from WRF output using 11-day initialization. Days 2-6 of the storm event area shown; upper left = July 1; upper right = July 2; middle left = July 3; middle right = July 4; lower left = July 5; and lower right = July 6.

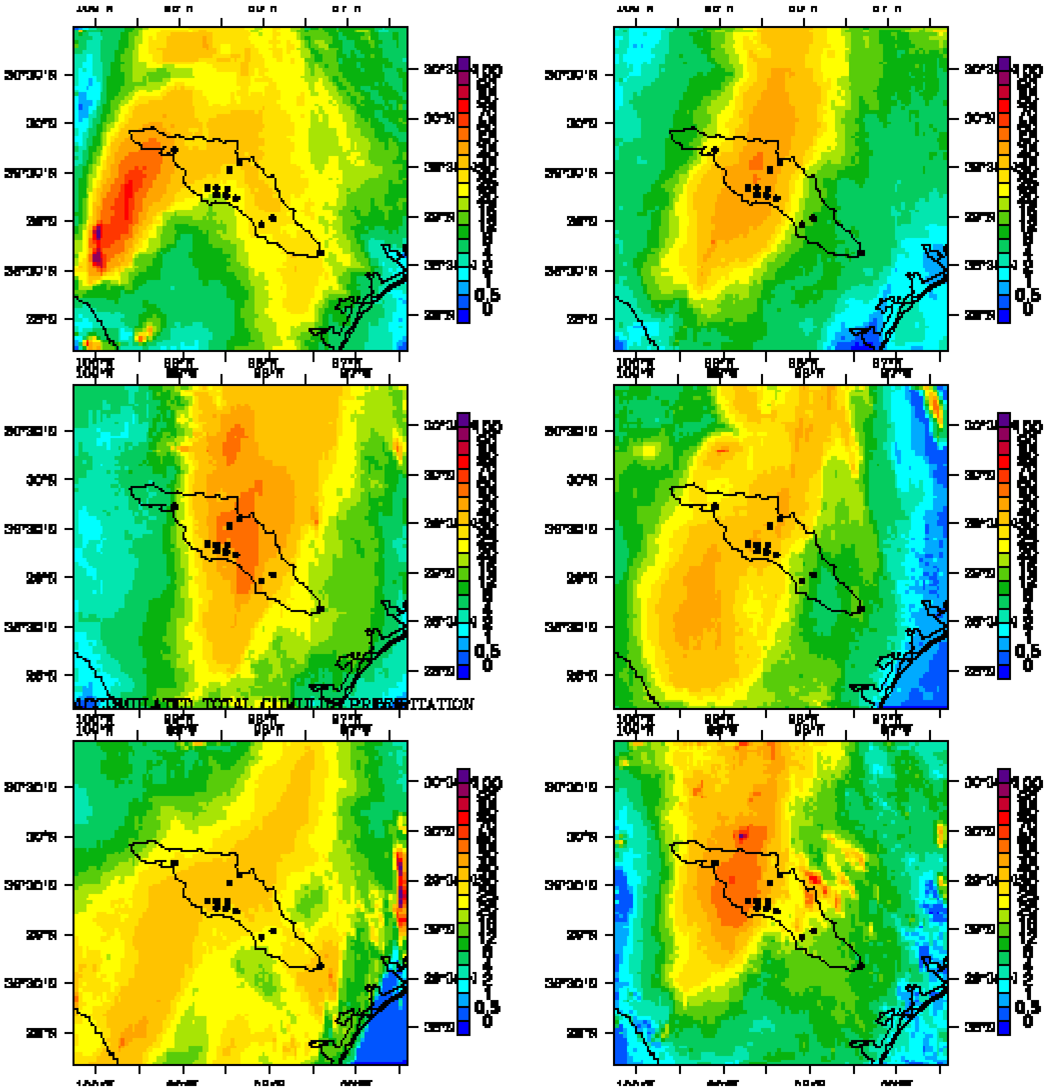

Figure 3.12. Same as Figure 3.11 but for a 5-day initialization.

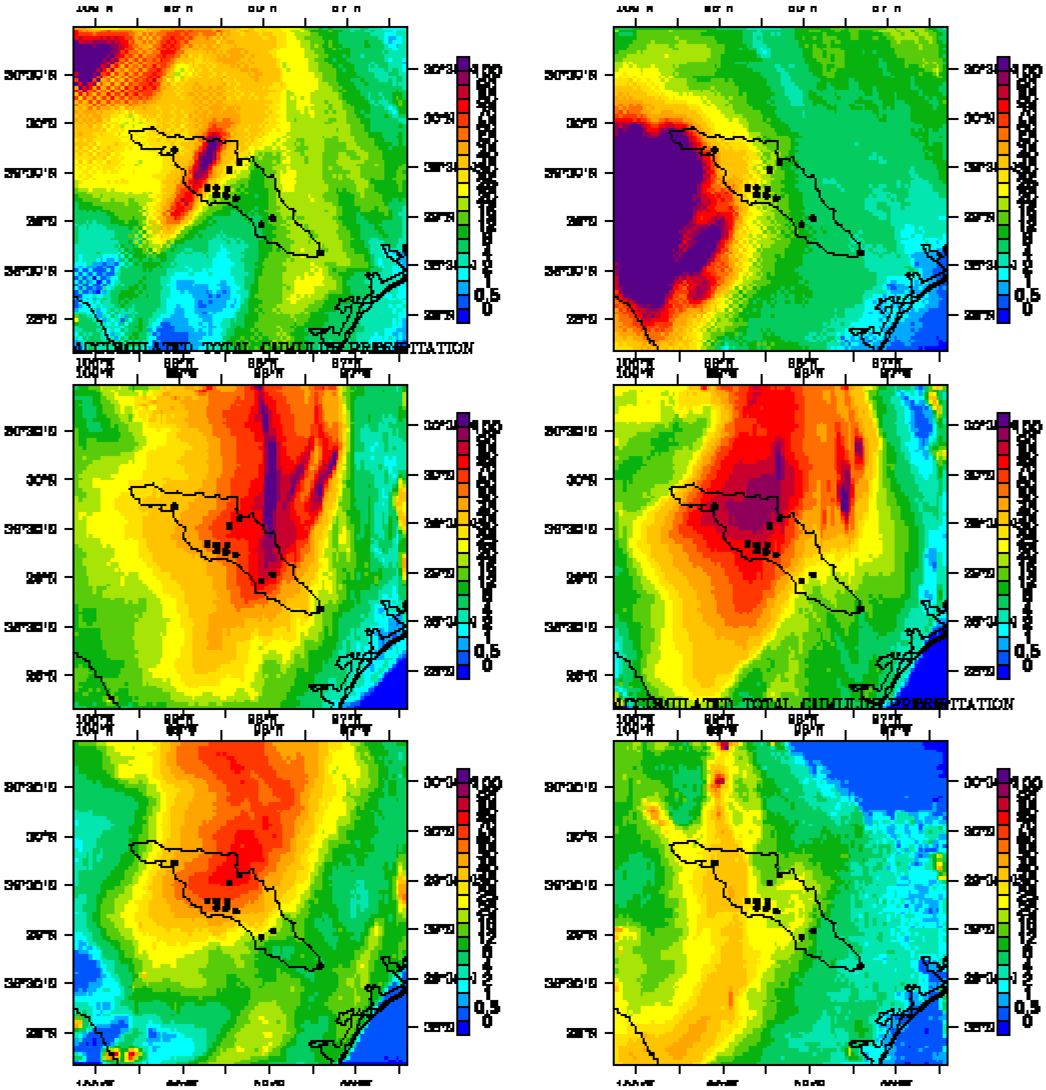

Figure 3.13. Same as Figure 3.11 but for a 3-day initialization.

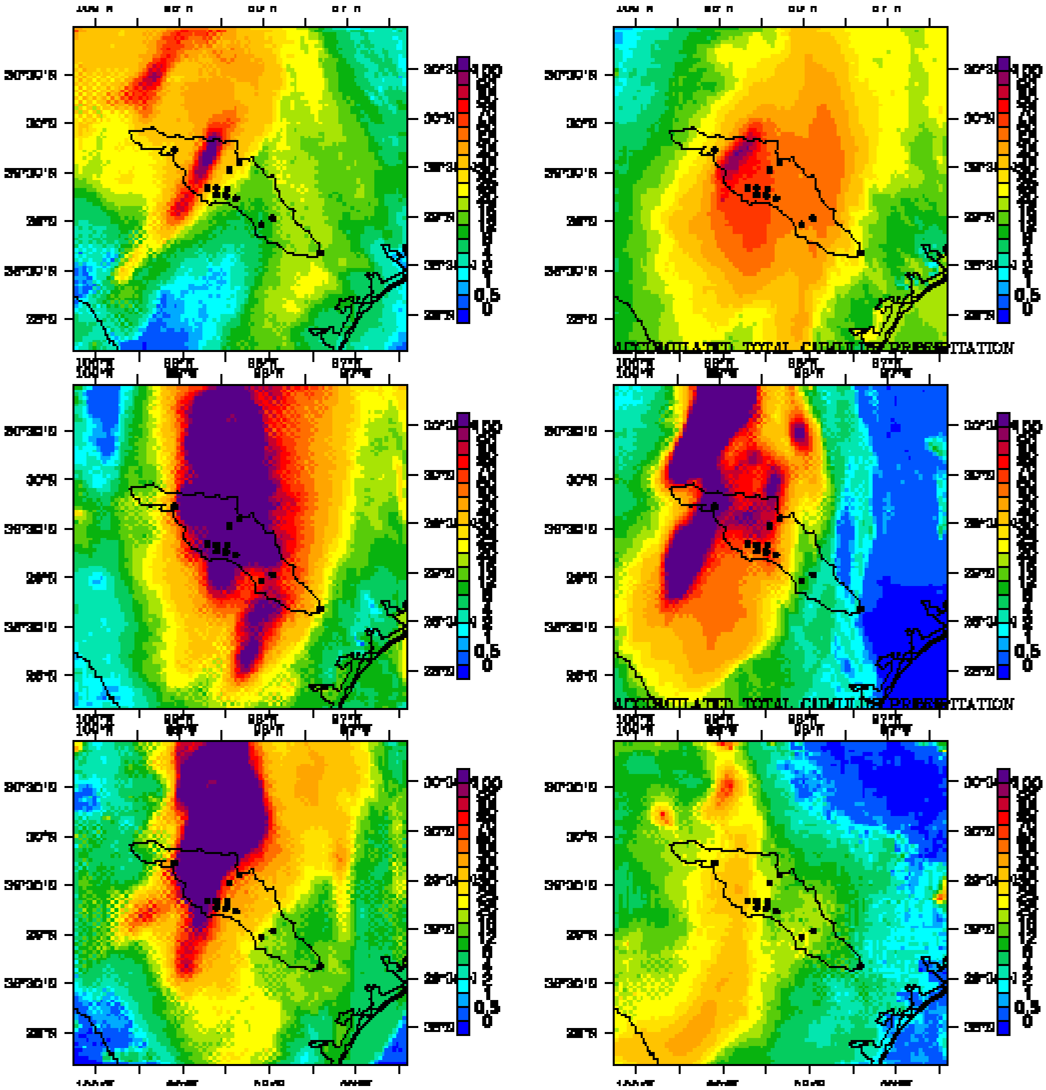

Figure 3.14. Same as Figure 3.11 but for a 2-day initialization.

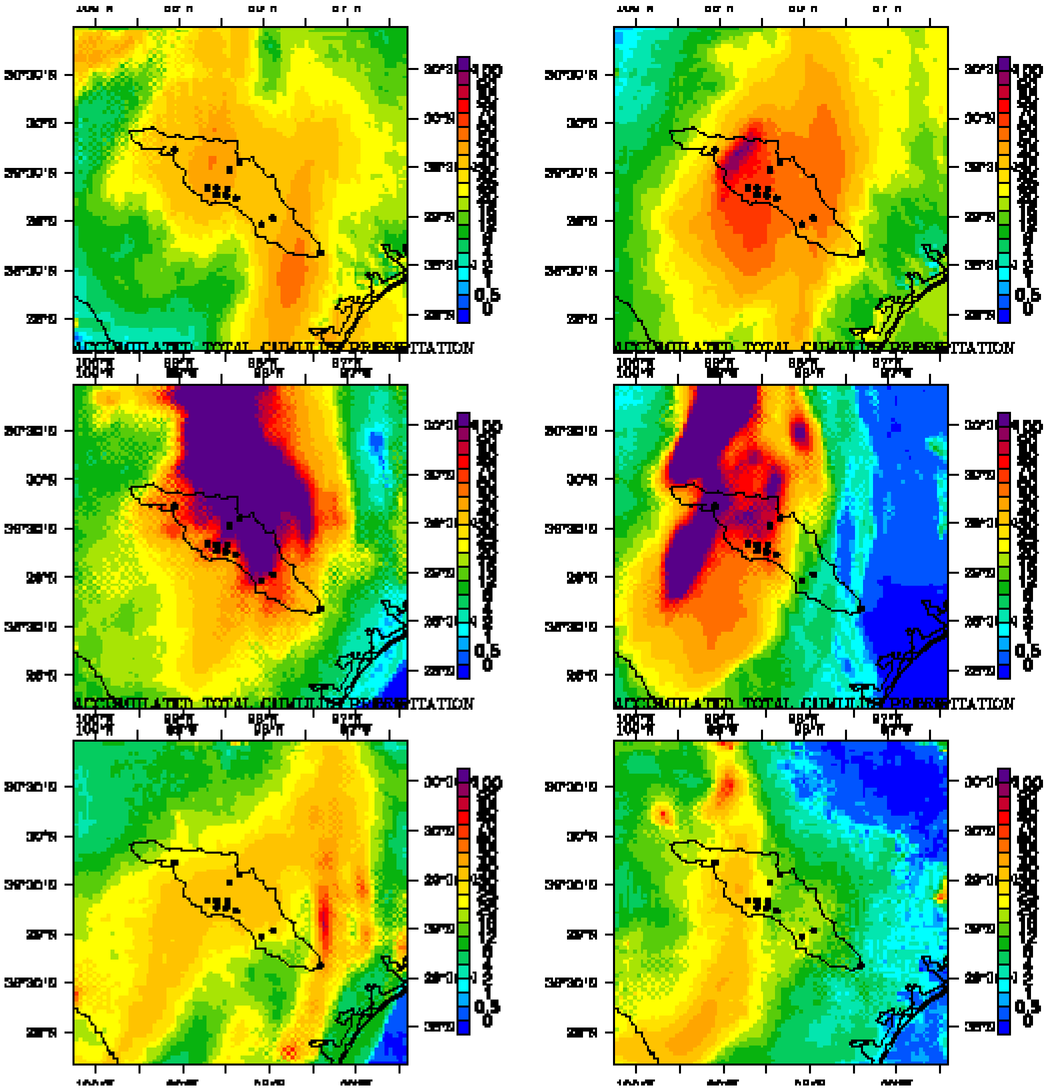

Figure 3.15. Same as Figure 3.11 but for a 1-day initialization.

On a technical note, it is worth mentioning the importance of running the WRFSI program to produce input files at the same interval used to run the WRF model. Due to time interpolation of certain land-surface variables, model input files will vary depending on stated forecast length during initialization. For example, LAI values in NARR are monthly averages; hence during interpolation, the variable LAI is set according to the forecast end date. Therefore, an interpolation through day-of-year (DOY) 180 (June 30) and one through DOY 181 (July 1) will have slightly different LAI values for June 30. Although this difference appears insignificant, slight variations in LAI will affect ET and convection processes, and over time will propagate into significant differences in rainfall over the region. Although this method is the most realistic, it may be more valuable to use an equal forecast length in WRFSI in order to isolate the atmospheric factors in WRF results and to remove the effects of variable land-surface characteristics. Model test runs using a uniform WRFSI forecast length of 24-hours were compared to those using varied WRFSI forecast lengths; it was found that the impacts of LAI and other time-dependent variables are generally small, and for the 2002 storm tend to cause small increases in precipitation intensity with decreased forecast length, while retaining the basic precipitation pattern.

Correlation with observations is significantly higher for smaller initialization intervals, with an r-value of 0.47 for 1-day initialization and 0.63 for 2-day initialization (Table 3.4). The streamflow output shows similar patterns to precipitation (Figure 3.16), with all but the 48-hour run underestimating streamflow. The 48-hour run produces a slight

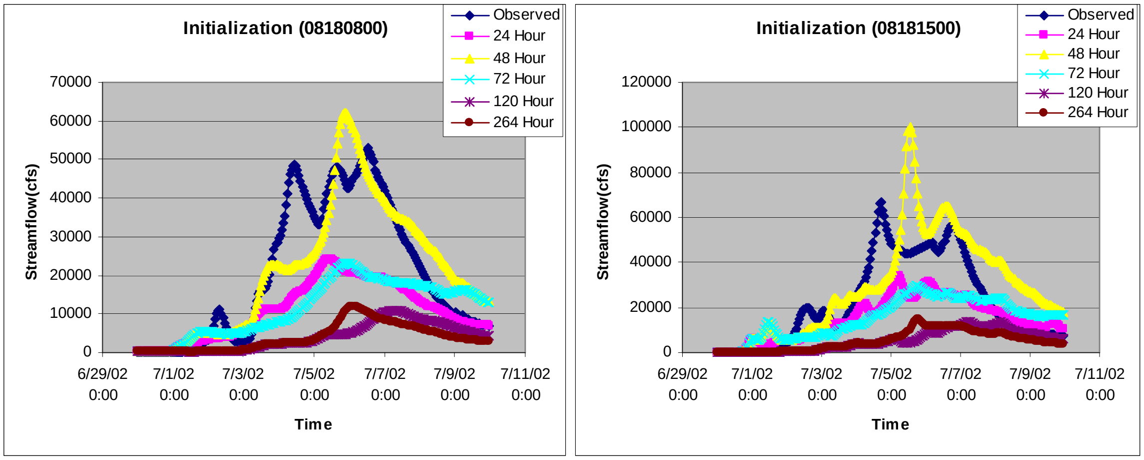

Figure 3.16. Select streamflow output (m^3 s^{-1})at USGS gage locations from the hydrological model, comparing the effects of different driving data (rainfall) from WRF.

Table 3.5. Correlation of modeled streamflow with observations for hydrological model runs driven with gridded precipitation output from WRF model runs of varying initialization intervals. Correlation coefficients at each gage area included to demonstrate the wide spatial variability of error.

Experiment	11D	5D	3D	2D	1D
Correlation : Upstream					
Gage 1	0.89	0.5	0.69	0.7	0.66
Gage 2	0.75	0.5	0.69	0.84	0.9
Gage 3	-0.04	-0.18	-0.06	0.01	0.05
Gage 4	0.26	-0.04	0.26	0.34	0.47
Correlation: Midstream					
Gage 5	0.78	0.55	0.75	0.88	0.93
Gage 6	0.32	0.11	0.23	0.18	0.34
Gage 7	0.73	0.49	0.74	0.78	0.88
Gage 8	0.02	-.01	-0.01	0.04	0.04
Gage 9	0.84	0.6	0.81	0.84	0.92
Correlation: Downstream					
Gage 10	0.94	0.91	0.96	0.96	0.95
Gage 11	0.47	0.16	0.56	0.63	0.78
Gage 12	0.88	0.88	0.94	0.96	0.98
Mean (Basin) Correlation	**0.98**	**0.96**	**0.94**	**0.88**	**0.88**
Mean Bias (cfs * 10^3)	**-11.9**	**-11.7**	**-6.0**	**1.8**	**-5.9**

11-day

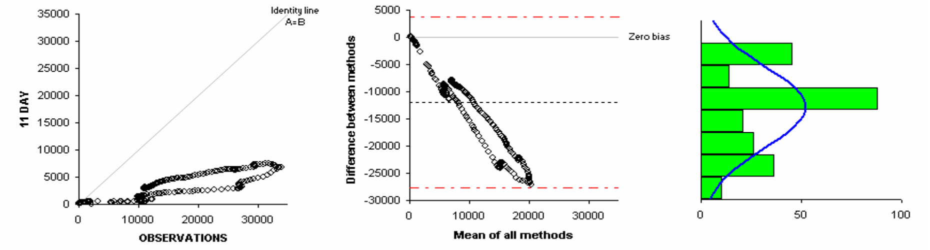

5-day

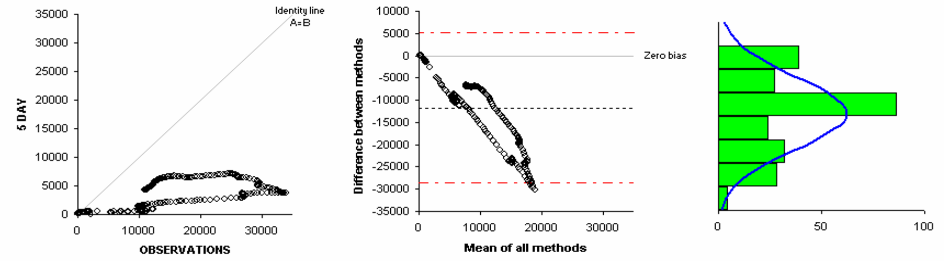

3-day

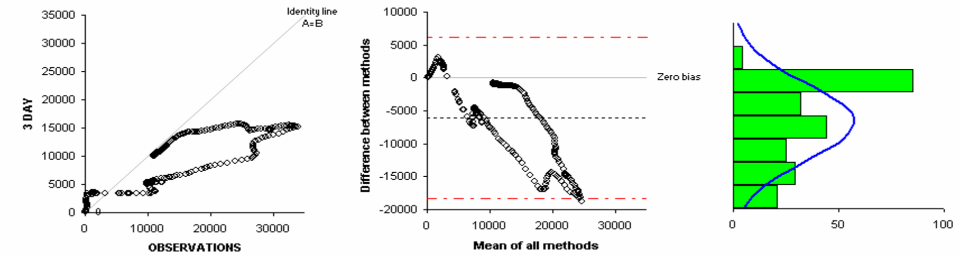

2-day

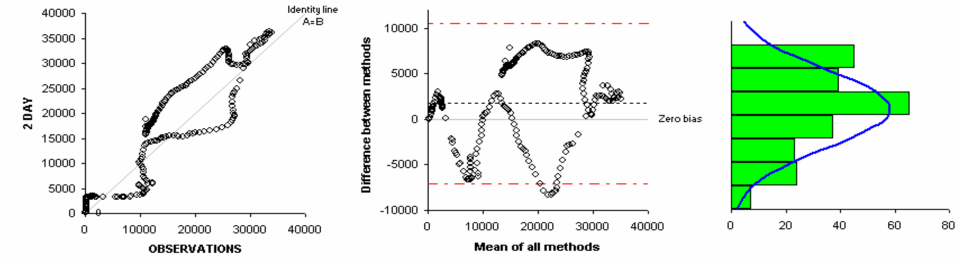

1-day

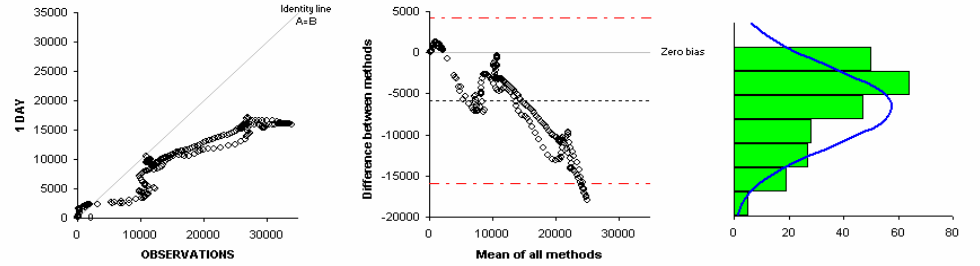

Figure 3.17. Bias plots for streamflow, using WRF output from initialization experiments to drive the hydrological model, averaged over the watershed. Leftmost column compares observed data to modeled streamflow; middle column plots residuals; rightmost column plots distribution of residuals in order to show the relative amount of underestimation and overestimation of streamflow.

time lag compared to observed streamflow, but captures the overall peak intensity and timing of basin streamflow. Correlation values are high for both experiments 1D and 2D. At urban gages, correlation is very low (Table 3.5); this low correlation was also observed when driving the streamflow model with observed radar data (Knebl et al., 2005), and therefore is likely due to error inherent in the hydrological model and not error in WRF output. A comparison of mean bias for each experiment (Table 3.5) as well as analysis of bias distribution (Figure 3.17) clearly demonstrates that the 2-day initialization best represents the entire storm. These results demonstrate that WRF performs reasonably well at producing precipitation on its own (without assimilation of observations) for 48-hour intervals.

c. Domain and boundary size

To study the sensitivity of precipitation forecasts to the size and location of model domain, various domain configurations are designed as shown in Figure 3.1. Six experiments are completed based on the six configurations (Table 3.6). All experiments utilize two domains, and the outer domain is driven by NARR forcing data. Physics and initialization details are dictated by best-fit results from the previous sections. Experiments are named using capital letters for larger domains and lower-case for smaller domains, according to the following convention: P and p, for parent domain 1 and 2, N, n, and nn for nest domains 1, 2, and 3, and BZ for increased boundary zone width. Experiment pn is designated as the control run, with the outer domain covering the entire state of Texas, and the inner domain covering the area of interest (San Antonio Basin), including a wide radius around the basin to allow for adjustment of parameters between the two domains. The outer domain in experiment Pn is enlarged to cover a significant portion of the Gulf of Mexico at its southeast corner (20 points added to the south and east sides). The objective of this configuration is to allow more adjustment time between ocean and land variables. To lessen the boundary effects that may occur when the forecast area is too close to the parent-nest boundary, experiment pN enlarges only the nested domain, approximately doubling its grid points in both directions. Both parent and nest domain are enlarged in experiment PN, to observe the combined effects of the previous two configurations. Experiment pnn shrinks the nested domain 8 points in the north-south direction and 4 points in the east-west direction to singularly model the area of flood interest. Lastly, experiment pnBZ doubles the default buffer zone width from 5 to 10 grid cells in an effort to reduce edge effects from nudging between parent and nest domain.

Qualitative comparison of the precipitation grids appears to demonstrate the control experiment pn as the most reasonable configuration for modeling the 2002 storm event over the San Antonio River Basin (Figures 3.18-3.23). Statistical analysis, however, demonstrates that each configuration has strengths and weaknesses (Tables 3.7 and 3.8). Enlarging the parent domain results in location errors over the basin during times of peak precipitation (experiment Pn; Figure 3.19). This is most likely due to introduction of errors from competition for convection at the land-ocean boundary (Nigam and Ruiz-Barradas, 2006). In experiment pN (Figure 3.20), enlarging the nest domain reduces the effect of synoptic forcing from the parent domain, and rainfall is underestimated. In experiment PN (Figure 3.21), the effects of enlarging both domains are compounded, with large errors in both intensity (underestimation) and location of rainfall. Doubling the buffer zone width in experiment pnBZ (Figure 3.23) diminishes the importance of small-scale mechanisms in producing convective precipitation in the nested domain, resulting in an underestimation of precipitation. Decreasing the area of the nest in experiment pnn (Figure 3.22) has a similar effect to increasing buffer zone width; precipitation patterns remain similar but decreased in intensity, and boundary edge effects are clearly observable. Streamflow hydrographs and bias plots also demonstrate that experiment pn most accurately reproduces observations (Figures 3.24 and 3.25).

Table 3.6. Domain configuration and grid dimensions used for domain experiments.

Experiment	Parent / Nest	Parent grid (i x j)	Nest grid (i x j)
Pn	2 / 2	105 x 105	97 x 94
Pn	1 / 2	125 x 125	97 x 94
pN	2 / 1	105 x 105	193 x 196
PN	1 / 1	125 x 125	193 x 196
pnn	2 / 3	105 x 105	79 x 70
pnBZ	2 / 2 / large boundary zone	105 x 105	96 x 93

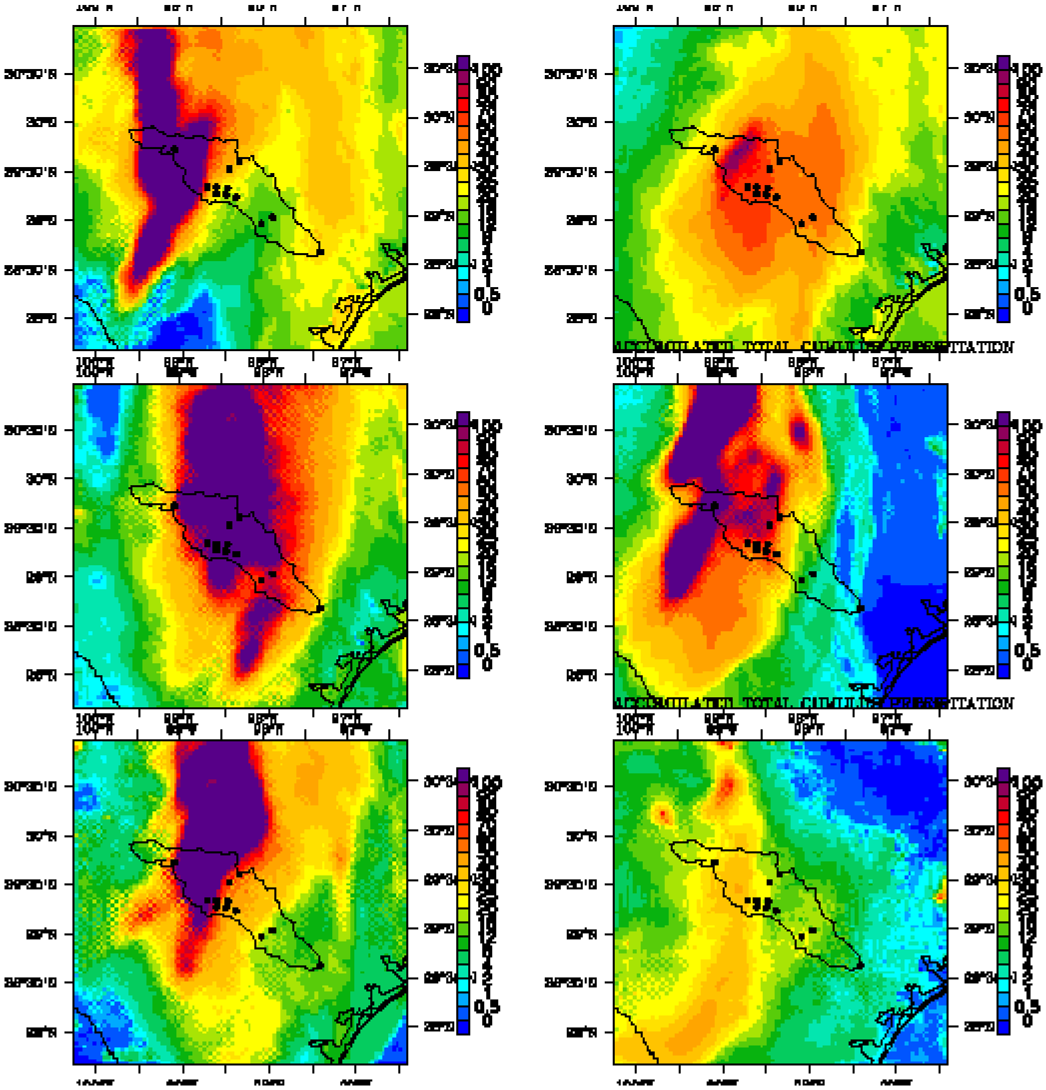

Figure 3.18. Total daily precipitation (mm day^{-1}) from WRF output using domain configuration **pn**. Days 2-6 of the storm event area shown; upper left = July 1; upper right = July 2; middle left = July 3; middle right = July 4; lower left = July 5; and lower right = July 6.

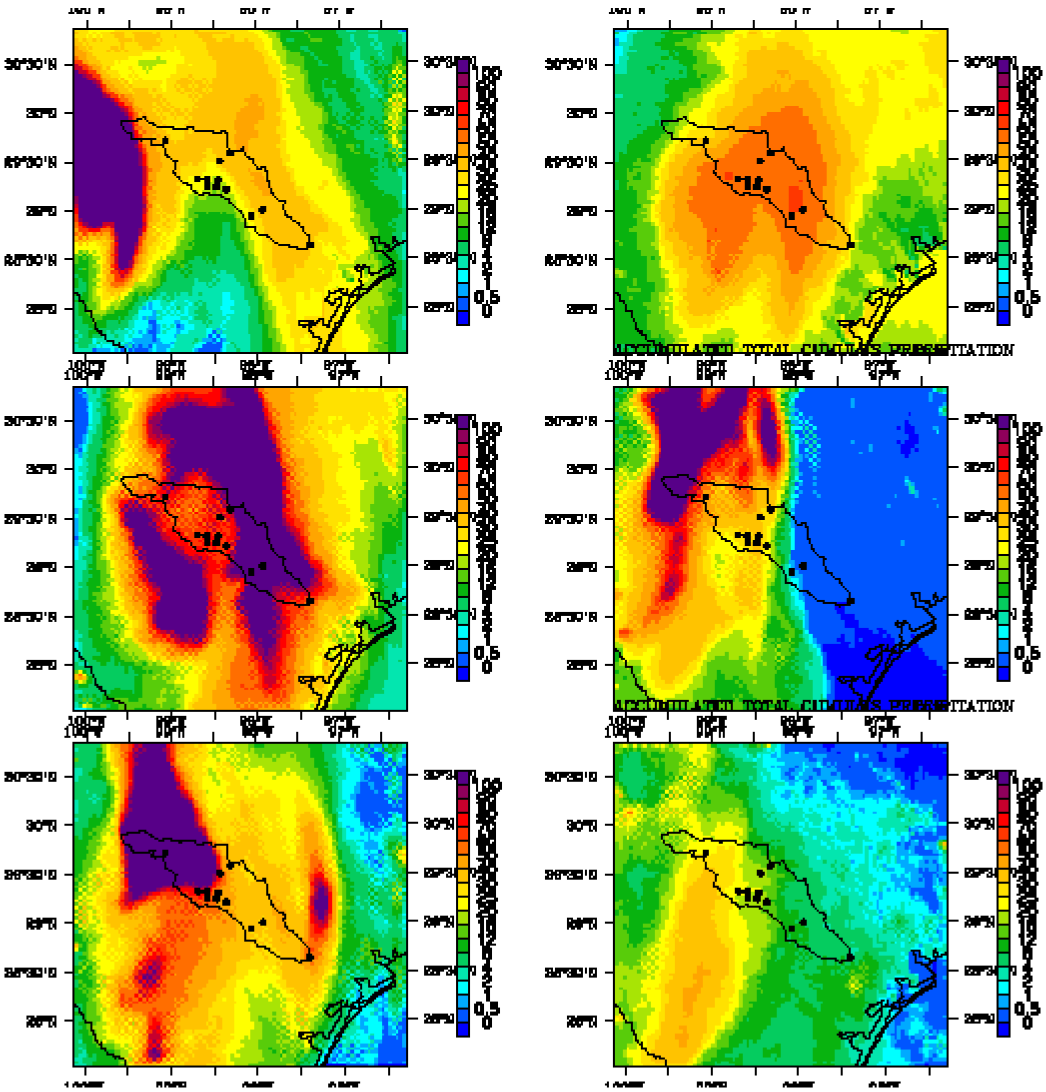

Figure 3.19. Same as Figure 3.18 but for a domain configuration **Pn**.

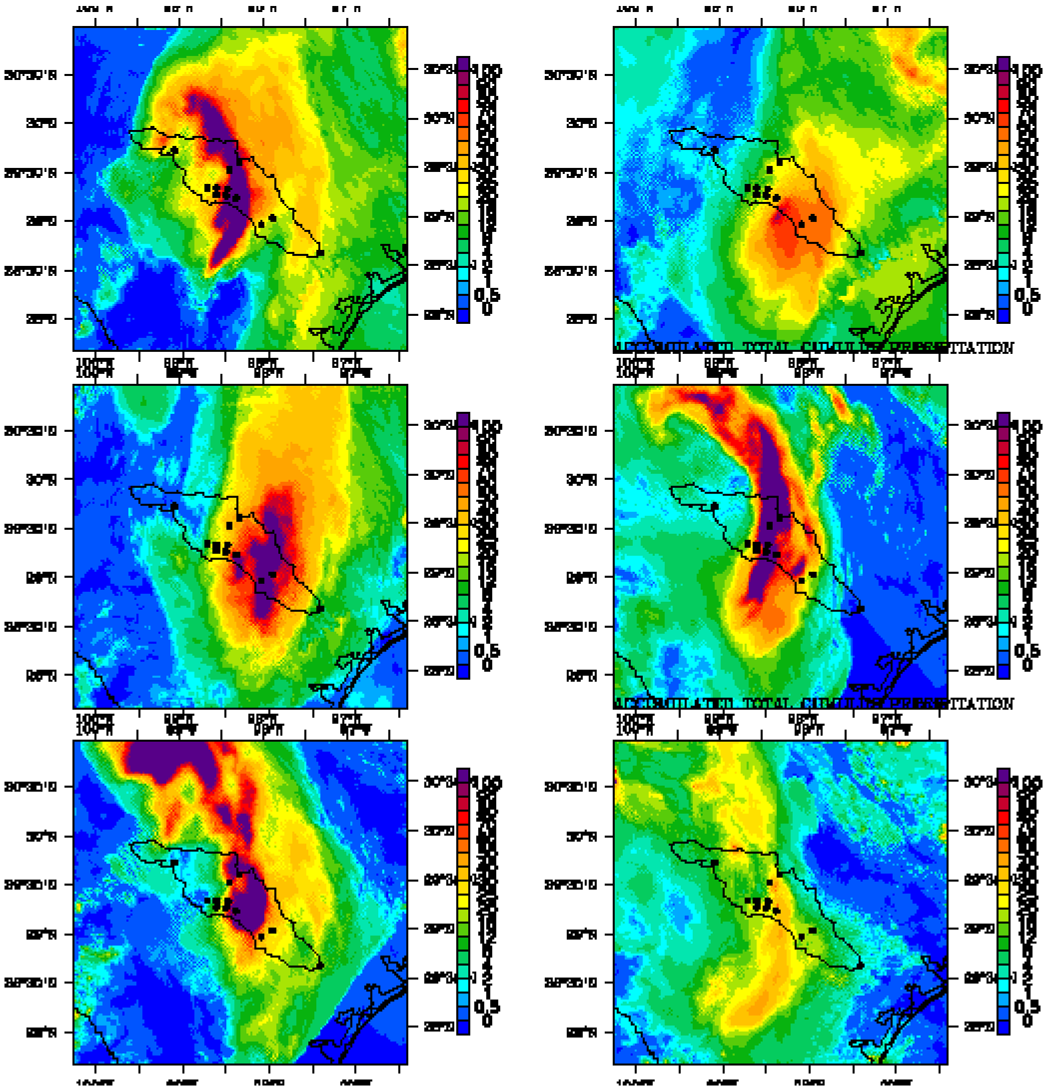

Figure 3.20. Same as Figure 3.18 but for a domain configuration **pN**.

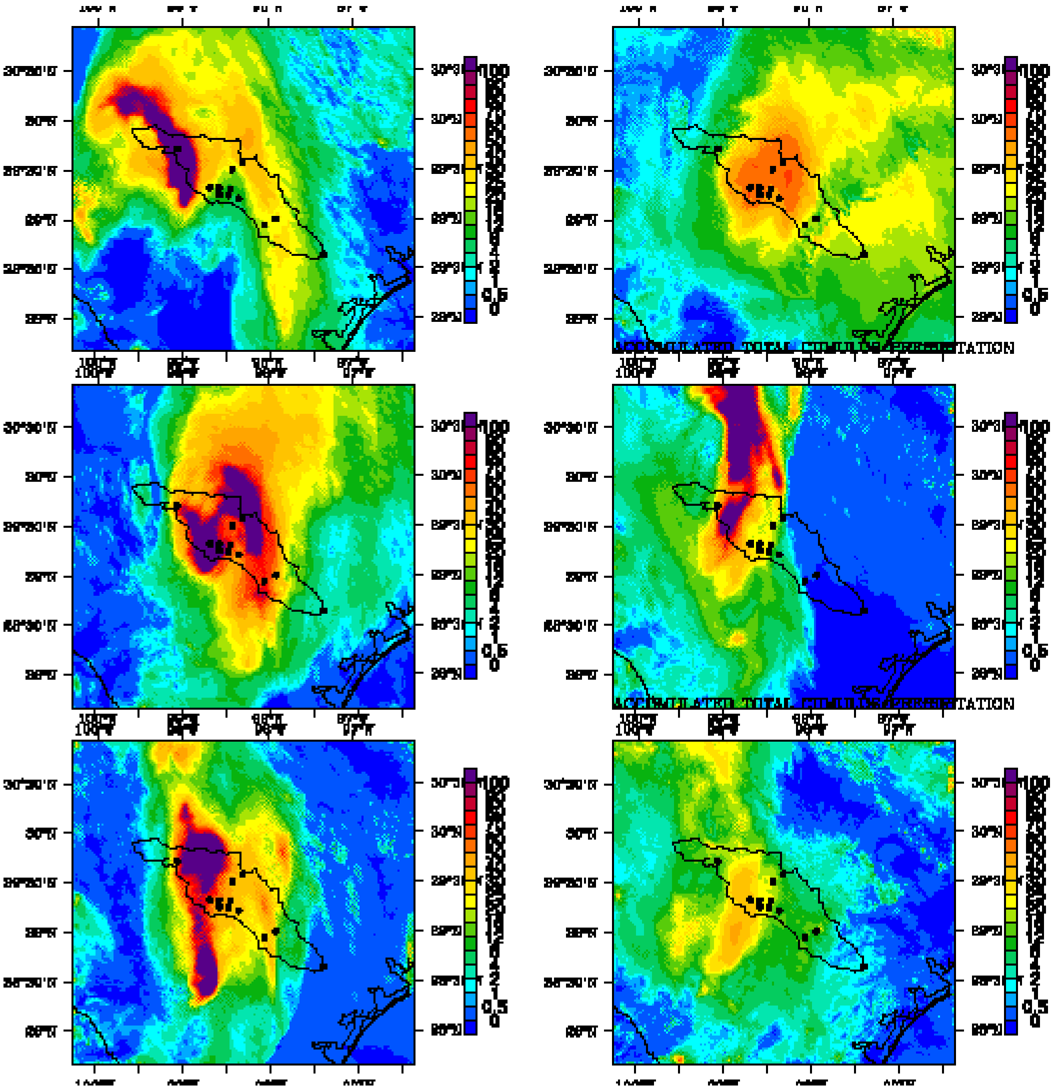

Figure 21. Same as Figure 3.18 but for a domain configuration **PN**.

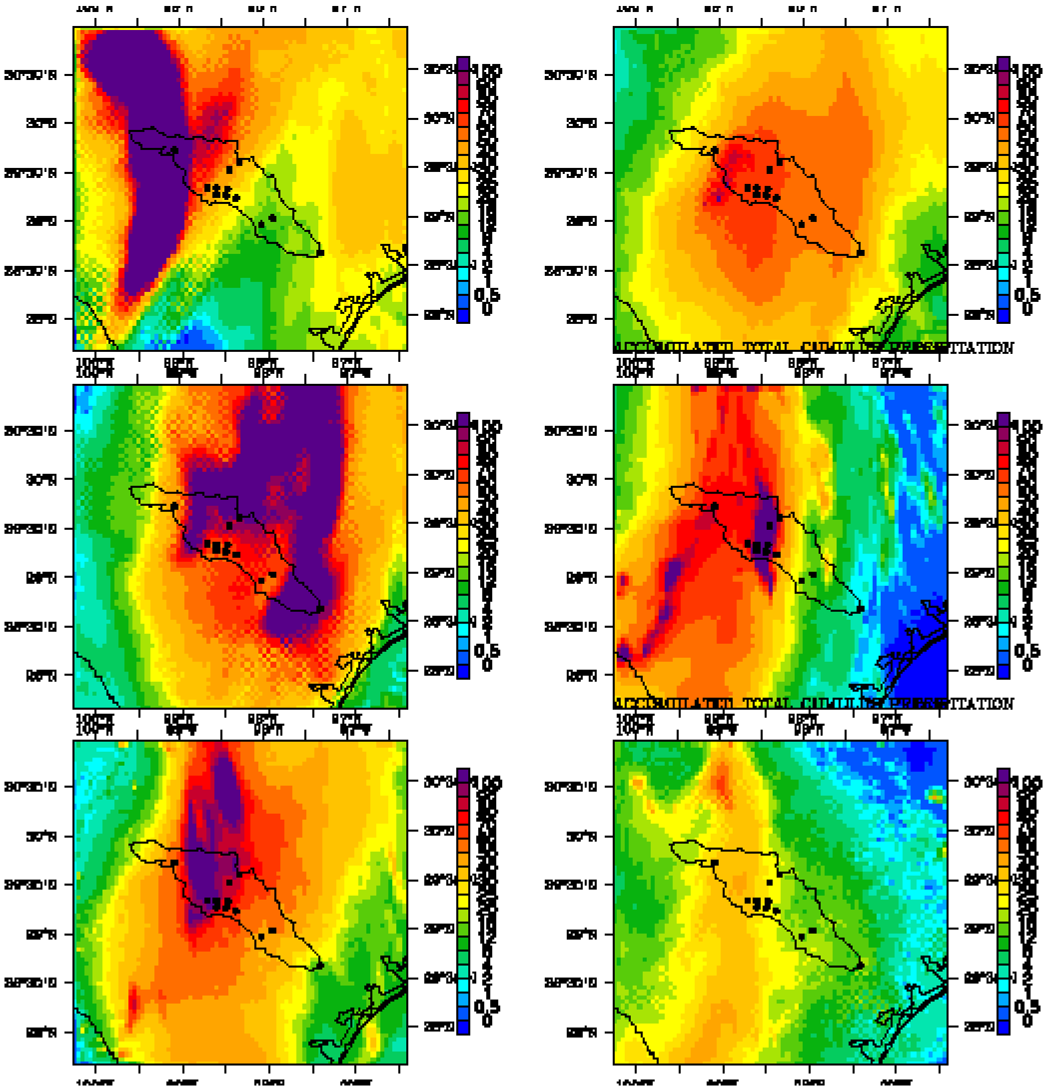

Figure 22. Same as Figure 3.18 but for a domain configuration **pnn**.

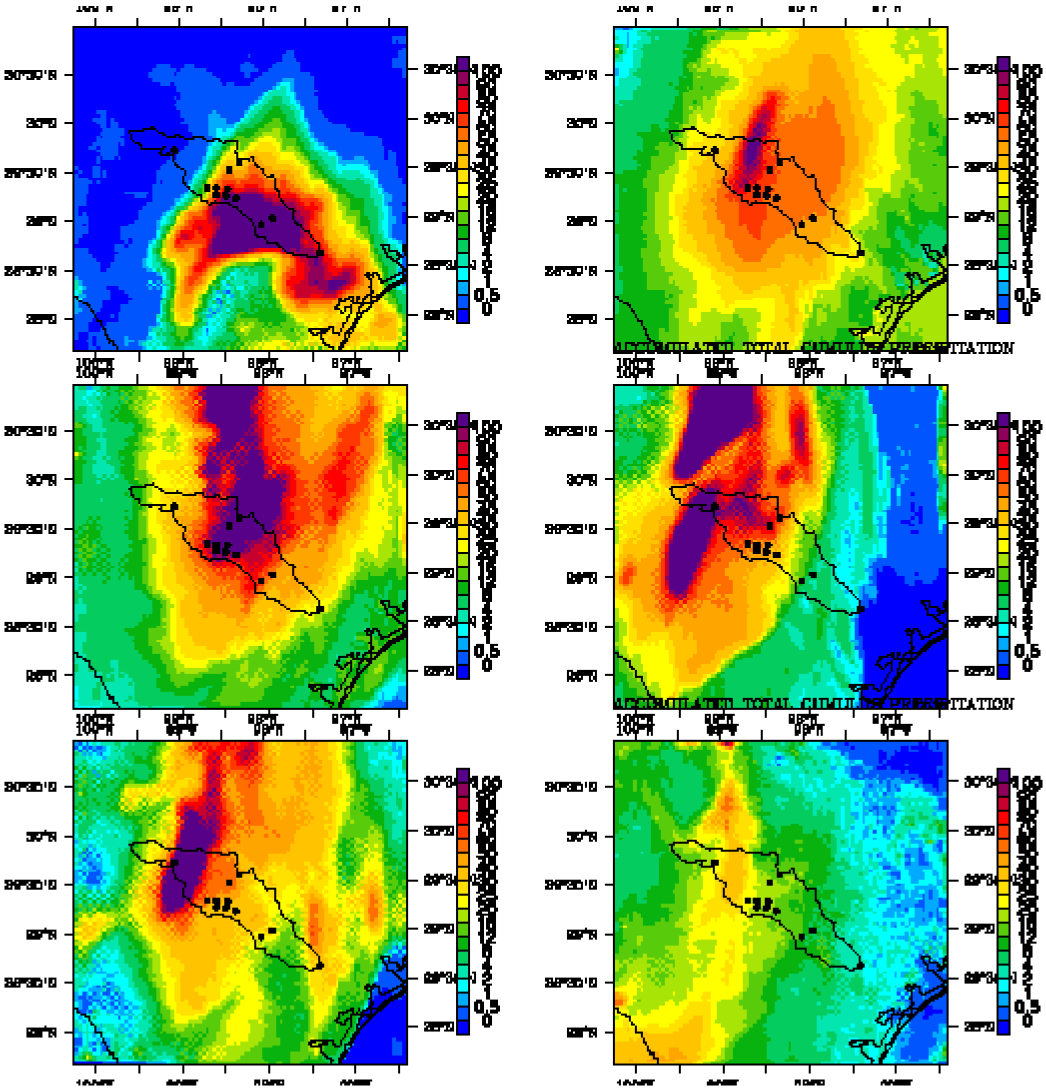

Figure 23. Same as Figure 3.18 but for a domain configuration **pnBZ**.

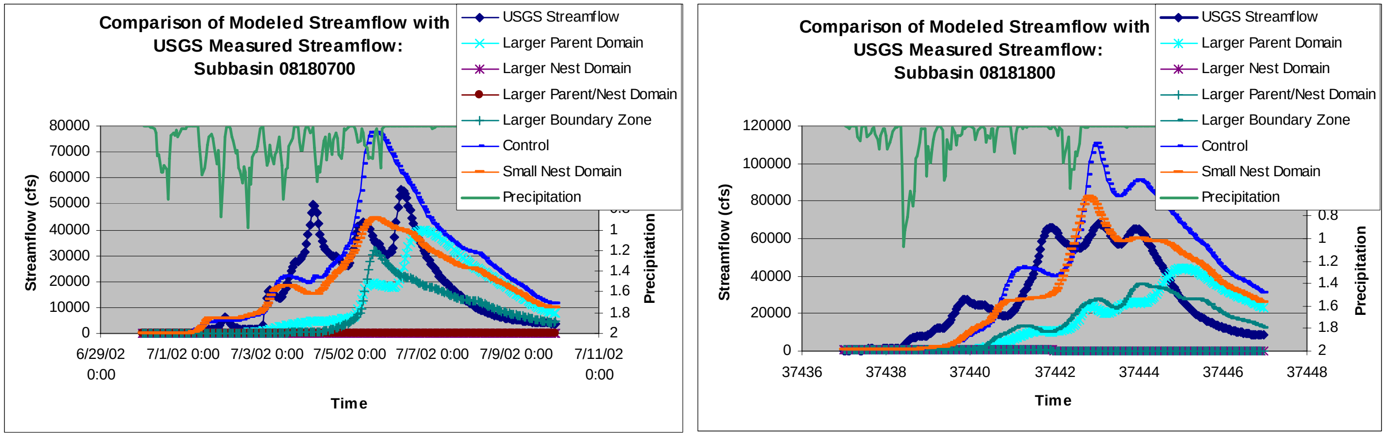

Figure 3.24. Select streamflow output (m^3 s^{-1})at USGS gage locations from the hydrological model, comparing the effects of different driving data (rainfall) from WRF.

Experiment pn: Parent Grid 2, Nest Grid 2

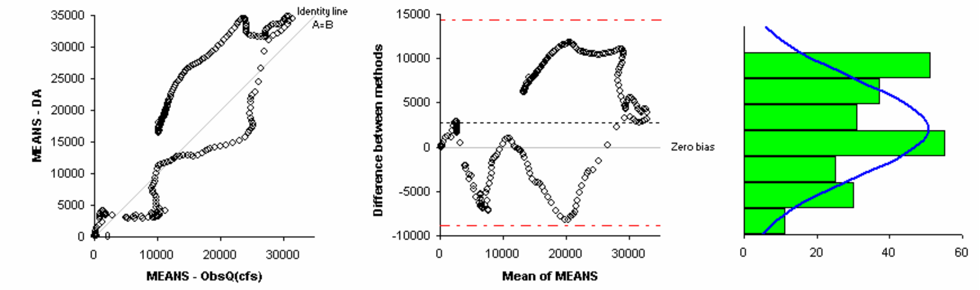

Experiment Pn: Parent Grid 1, Nest Grid 2

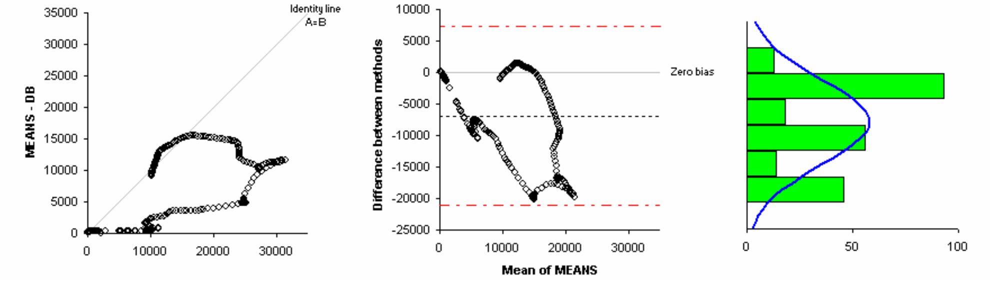

Experiment pN: Parent Grid 2, Nest Grid 1

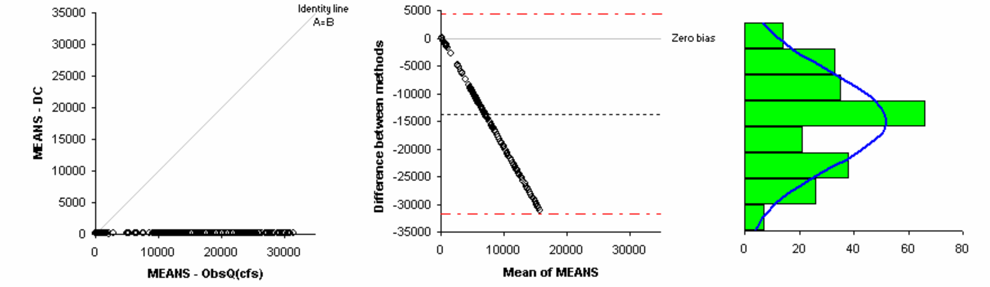

Experiment PN: Parent Grid 1, Nest Grid 1

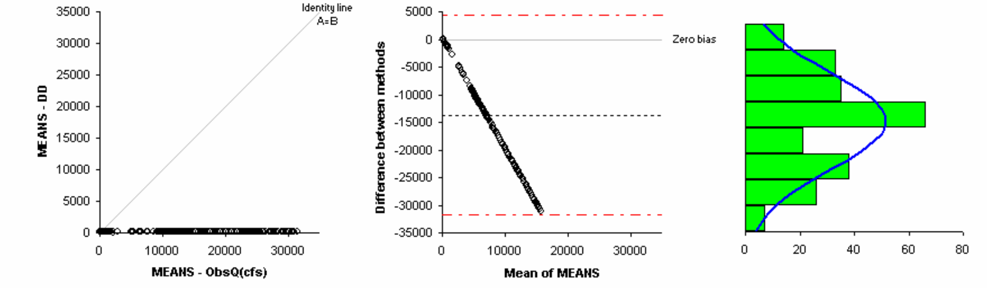

Figure 3.25. (continued on next page)

Experiment pnn: Parent Grid 2, Nest Grid 3

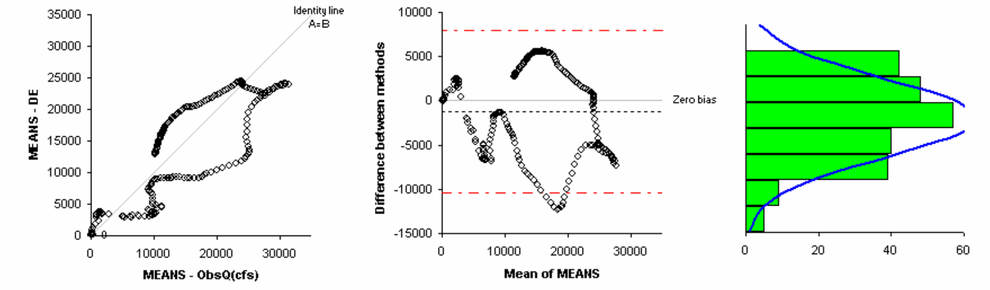

Experiment pnBZ: Parent Grid 2, Nest Grid 2, Large Boundary Zone

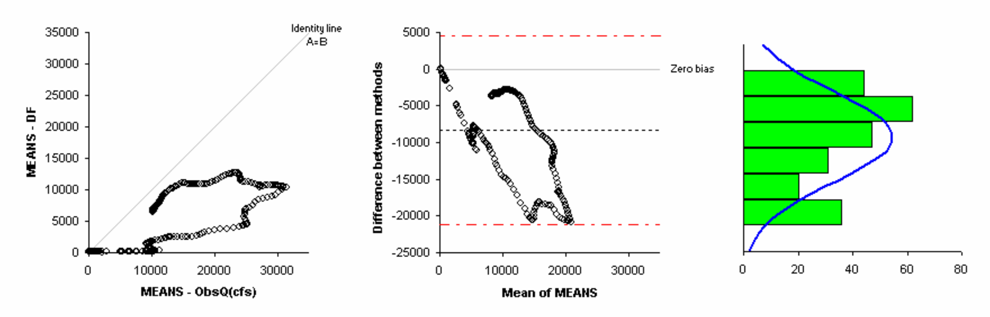

Figure 3.25. Bias plots for streamflow, averaged over the watershed. Leftmost column compares observed data to modeled streamflow; middle column plots residuals; rightmost column plots distribution of residuals in order to show the relative amount of underestimation and overestimation of streamflow.

Table 3.7. Same as Table 3.4 but for domain configuration experiments.

Experiment	Storm Mean (mm day^{-1})	Daily Deviation	Correlation with Observations (%)
Observed	31.6	13.6	-
pn	42.34	14.0	0.72
Pn	42.43	8.1	0.73
pN	25.30	6.4	0.68
PN	22.77	5.4	0.71
pnn	36.06	6.5	0.62
pnBZ	27.26	7.3	0.48

Table 3.8. Same as Table 3.5 but for domain configuration experiments.

Experiment	pn	Pn	pN	PN	pnn	pnBZ
Correlation : Upstream						
Gage 1	0.29	0.94	0.64	-0.09	0.28	0.84
Gage 2	0.8	0.43	-0.34	-0.33	0.8	0.56
Gage 3	-0.02	-0.09	0.0	0.0	-0.03	-0.06
Gage 4	0.27	0.16	-0.11	-0.06	0.25	0.1
Correlation: Midstream						
Gage 5	0.85	0.5	-0.62	-0.49	0.84	0.63
Gage 6	0.18	0.14	0.01	0.2	.019	0.16
Gage 7	0.75	0.27	-0.48	-0.42	0.74	0.53
Gage 8	0.03	0.0	0.27	0.27	0.06	0.01
Gage 9	0.79	0.32	-0.48	-0.46	0.78	0.64
Correlation: Downstream						
Gage 10	0.97	0.8	-0.92	-0.91	0.97	0.94
Gage 11	0.53	0.38	-0.36	-0.36	0.5	0.33
Gage 12	0.9	0.84	-0.96	-0.96	0.93	0.86
Mean (Basin) Correlation	**0.87**	**0.62**	**-0.29**	**-0.52**	**0.86**	**0.75**
Mean Bias (cfs * 10^3)	**2.8**	**-6.9**	**-13.7**	**-13.7**	**-1.2**	**-8.4**

d. Performance of best-fit WRF model

The best-fit WRF model, using a 48-hour initialization, domain pn, and physics as described previously, is investigated in more detail in order to assess its ability to simulate the 2002 storm event. Figure 3.26 compares horizontal winds and divergence between NARR reanalysis data and two WRF configurations: the best-fit configuration and a poor-performing configuration (i.e., one that produces significant precipitation error, domain PN).

Figure 3.26 displays the observed winds (from NARR reanalysis) and modeled wind vectors for upper, middle, and lower levels of the atmosphere. Strong trade winds are apparent at the 850 mb level over the Gulf of Mexico; these winds bring moisture into the Central Texas region, and weaken as the storm progresses. As these southerly winds move across land, they begin to weaken slightly, triggering low-level convergence. Weakening winds are also apparent as air flows over the BFZ in central Texas. Both the best-fit and poor-performing WRF models appear to simulate this near-surface wind pattern quite well (Figures 3.26b, 3.26c).

At mid-levels of the atmosphere, a strong cyclonic circulation, consistent with observations, develops in the best-fit model (Figure 3.26e). The poor-performing WRF places this circulation too far north, over the Texas-Oklahoma boundary, which may contribute to its underestimation of storm extent (Figure 3.26f).

Both upper level divergence and related anticyclone east of the storm are clearly displayed in the WRF best-fit model (Figure 3.26h). The poor-performing model run (Figure 3.26i) demonstrates much weaker divergence and only minimal anticyclonic

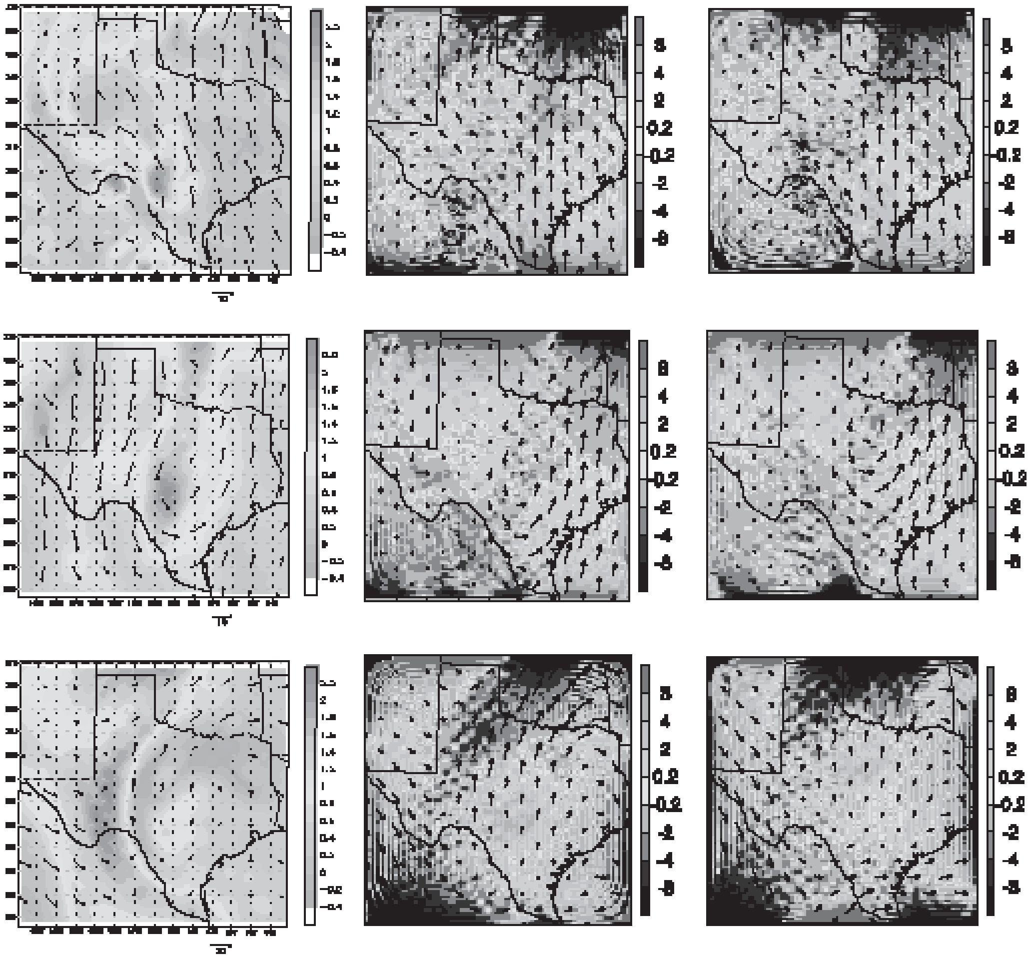

Figure 3.26. Vector winds at three levels in the atmosphere, compared between observed winds (from NARR), best-fit WRF output, and poor-fit WRF (domain **PN**) output: 850mb a) NARR; b) best-fit; c) poor-fit; 500mb d) NARR; e) best-fit; f) poor-fit; and 200mb g) NARR; h) best-fit; i) poor-fit.

winds. This lack of divergence in the upper atmosphere may inhibit convection and contribute to precipitation underestimation.

Additionally, water vapor mixing ratios display patterns consistent with observations (not shown), with increasing values as the storm progresses and significantly decreasing values several days after the storm has passed. The largest variation in moisture occurs at mid-levels of the atmosphere, where cyclonic circulation dominates, and over middle and upper regions of the basin, where convective precipitation is strongest.

e. Small-amplitude random errors

Even after adjusting model physics, initialization and domain configurations, the resultant best-fit model still shows significant errors compared to observations. These errors can be attributed to small inaccuracies in initial conditions that grow exponentially with time. Introducing small perturbations into the model can aid in understanding how these initial errors grow. Zhang et al. (2006) perturbed their model domain using thermal bubbles, and found that nonlinear error growth mechanisms are of secondary importance to practical error such as erroneous physical parameterization. Their results implied that error growth is greatest for high-resolution domains and in regions of high convective activity. Major error types encountered in regional models include intensity, location, and timing errors, with erroneous location shifts most common.

Since precipitation errors are nonlinear, their effect on various hydrologic fluxes may be manifest in either an amplification or a dampening of the variable. To test the effect of common precipitation errors in the WRF model on streamflow output from a surface hydrologic model, WRF output grids were perturbed arbitrarily (in both positive and negative directions) in intensity, location, and timing. Only those grid cells residing in the area of flood interest (Figure 3.1) were perturbed. Intensity error was introduced by adding the following rainfall to each grid cell (in mm/hr): +/- 0.01, 0.05, 0.1, 0.5, 1, 2, 3, 4, 5. Absolute value, instead of percentage, was used to obtain more meaningful results over the basin. Location error was introduced by shifting rainfall amounts 1, 3, 5, and 10 grid cells in each of four directions: NE, NW, SE, SW. Finally, timing errors were introduced in two ways. First, hours were added or subtracted from each rainfall grid cell as follows: +/- 3, 6, 12, 18 hours. This simple shift is not particularly realistic for typical rainfall errors, so additional experiments were run changing the duration of rainfall. Rainfall grid cells during peak times were perturbed to a) widen the peak; b) narrow the peak; and c) extensively narrow the peak (to mimic flash flooding).

Table 3.9 uses a moderate rainfall error of +2 mm/hr to demonstrate the variation in streamflow error with location in the basin, over the 72-hour peak rainfall period. Correlation values over the storm period are high for all locations. The value of CTL/EXP allows study of the relative overestimation and underestimation of precipitation in each subbasin region. As expected, increasing rainfall error in a positive direction results in an overestimation of streamflow in all subbasins, with the exception of the lowermost subbasin. This large subbasin consists of mostly agricultural soils, and may be better equipped to dampen the response to increased rainfall and streamflow upstream. In addition, this subbasin has a long response time; much of the effects from upstream rainfall may be delayed beyond the time scope observed in this study. In subbasins with a shorter response time, such as those with bedrock-dominated streams (Gage 2) or those in urban areas (Gage 7), increases in precipitation are quickly translated to runoff, and hence in these basins streamflow is greatly overestimated.

Statistics for various error types are displayed in Table 3.10 and Figures 3.27-3.29. Positive (negative) perturbations to rainfall magnitude show a comparable increase (decrease) in streamflow. Interestingly, positive rainfall errors are manifested in streamflow error throughout the entire storm, while negative errors result in lower overall streamflow error and are concentrated at the storm peak (Figure 3.27). Intensity errors in precipitation show a linear translation pattern for streamflow, especially for positive rainfall perturbations; intensity errors also tend to retain the shape of the hydrograph. Location shifts in precipitation are a significant error type, because the streamflow response is erratic and difficult to predict. Rainfall location errors to the east, especially the southeast, result in the highest streamflow errors (Figure 3.28). Location errors to the west (NW and SW) appear to retain the correct hydrograph shape and have fewer errors in discharge magnitude. This directional variability of streamflow error is highly dependent on the actual location and size of peak rainfall; glancing back at Figure 3.18 (the best-fit rainfall), it is clear that rainfall changes most rapidly in an ESE direction away from the peak. Lagging or advancing the precipitation peak timing results in a linear lag or advance of the streamflow peak (Figure 3.29a,b); however, the error is significantly larger for time lagged experiments. For example, perturbing the precipitation -12 hours results in a mean absolute error (MAE) of 213.3%, while perturbing the precipitation +12 hours results in only a MAE of 58.4%. In the case of a negative lag, the peak also increases with increased lag time, due to increased time of concentration, which allows the basin more time to accumulate and then translate runoff to the river network. The effect of peak shape perturbations is most pronounced for an erroneously wide peak (Figure 3.29c); in this case the overall volume of streamflow is increased to the extent that the hydrograph peak is not well-defined compared to the best-fit result.

Table 3.9. Spatial variability of streamflow error. A precipitation error in WRF of 2mm hr^{-1} over the basin area is used as an example. The ration of best-fit to modeled streamflow (CTL/EXP) shows the overestimation (CTL/EXP<0) and underestimation (CTL/EXP>0) at various gages across the basin. Time increments are averages during the peak 72 hours of the storm.

Time Increment (hours)	1-12	13-24	25-36	37-48	49-60	61-72	Mean Storm R
CTL/EXP : Upstream							
Gage 1	0.56	0.41	0.30	0.30	0.36	0.31	0.94
Gage 2	0.21	0.09	0.07	0.07	0.11	0.10	0.94
Gage 3	0.99	0.68	0.72	0.78	0.99	0.76	0.96
Gage 4	0.44	0.25	0.20	0.23	0.34	0.29	0.97
CTL/EXP: Midstream							
Gage 5	0.25	0.09	0.06	0.06	0.10	0.08	0.95
Gage 6	0.31	0.59	0.52	0.45	0.62	0.50	0.98
Gage 7	0.18	0.08	0.05	0.05	0.07	0.06	0.97
Gage 8	1.06	0.71	0.70	0.74	0.96	0.75	0.96
Gage 9	0.18	0.07	0.01	0.01	0.06	0.05	0.97
CTL/EXP: Downstream							
Gage 10	0.22	0.10	0.06	0.04	0.06	0.05	0.99
Gage 11	0.79	0.40	0.22	0.15	0.20	0.20	0.98
Gage 12	25.71	13.43	6.23	1.72	0.82	0.34	0.99

Table 3.10. Intensity, location, and timing error characteristics for streamflow: mean absolute error, bias, and standard deviation of streamflow resulting from each of 45 perturbations to the WRF output rainfall grid.

Intensity Error	Basin MAE	Mean Bias[1]	Bias SD	Intensity Error	Basin MAE	Mean Bias[1]	Bias SD
+0.01 mm hr^{-1}	10.1	-0.091	0.058	-0.01 mm hr^{-1}	0.6	0.077	0.048
+0.05 mm hr^{-1}	5.0	-0.455	0.292	-0.05 mm hr^{-1}	2.9	0.383	0.240
+0.10 mm hr^{-1}	10.1	-0.912	0.583	-0.10 mm hr^{-1}	5.6	0.760	0.479
+0.50 mm hr^{-1}	56.7	-4.644	2.909	-0.50 mm hr^{-1}	23.7	3.570	2.303
+1.00 mm hr^{-1}	130.8	-9.472	5.818	-1.00 mm hr^{-1}	40.3	6.605	4.337
+2.00 mm hr^{-1}	342.2	-19.529	11.652	-2.00 mm hr^{-1}	60.6	11.035	7.403
+3.00 mm hr^{-1}	641.8	-29.955	17.481	-3.00 mm hr^{-1}	68.8	13.188	9.040
+4.00 mm hr^{-1}	1023.7	-40.632	23.285	-4.00 mm hr^{-1}	72.1	14.225	9.944
+5.00 mm hr^{-1}	1479.1	-51.475	29.070	-5.00 mm hr^{-1}	73.7	14.743	10.409

Location Error	Basin MAE	Mean Bias[1]	Bias SD	Timing Errors	Basin MAE	Mean Bias[1]	Bias SD
Shift1NE	7.8	1.075	1.022	WidePeak	35.7	-9.897	8.876
Shift1NW	9.7	0.057	0.517	NarrowPeak	15.2	-4.455	4.123
Shift1SE	10.9	0.237	0.545	FlashPeak	10.1	-2.909	2.688
Shift1SW	6.5	-0.800	0.825	+3 hours	27.9	0.430	2.755
Shift3NE	30.6	3.757	3.585	+6 hours	25.1	0.174	2.045
Shift3NW	24.3	1.175	1.598	+12 hours	51.3	0.605	3.797
Shift3SE	44.6	1.173	1.999	+18 hours	85.2	1.064	5.240
Shift3SW	17.6	-1.589	1.936	-3 hours	18.1	0.234	1.041
Shift5NE	73.5	6.239	5.717	-6 hours	49.3	0.506	1.904
Shift5NW	35.1	3.092	2.822	-12 hours	206.7	0.987	3.415
Shift5SE	106.9	2.286	3.185	-18 hours	603.6	1.402	4.607
Shift5SW	25.6	-1.003	2.068				
Shift10NE	227.8	8.815	7.001				
Shift10NW	53.3	7.844	5.897				
Shift10SE	115.6	6.157	6.186				
Shift10SW	40.1	0.755	2.447				

[1] cfs * 10^3

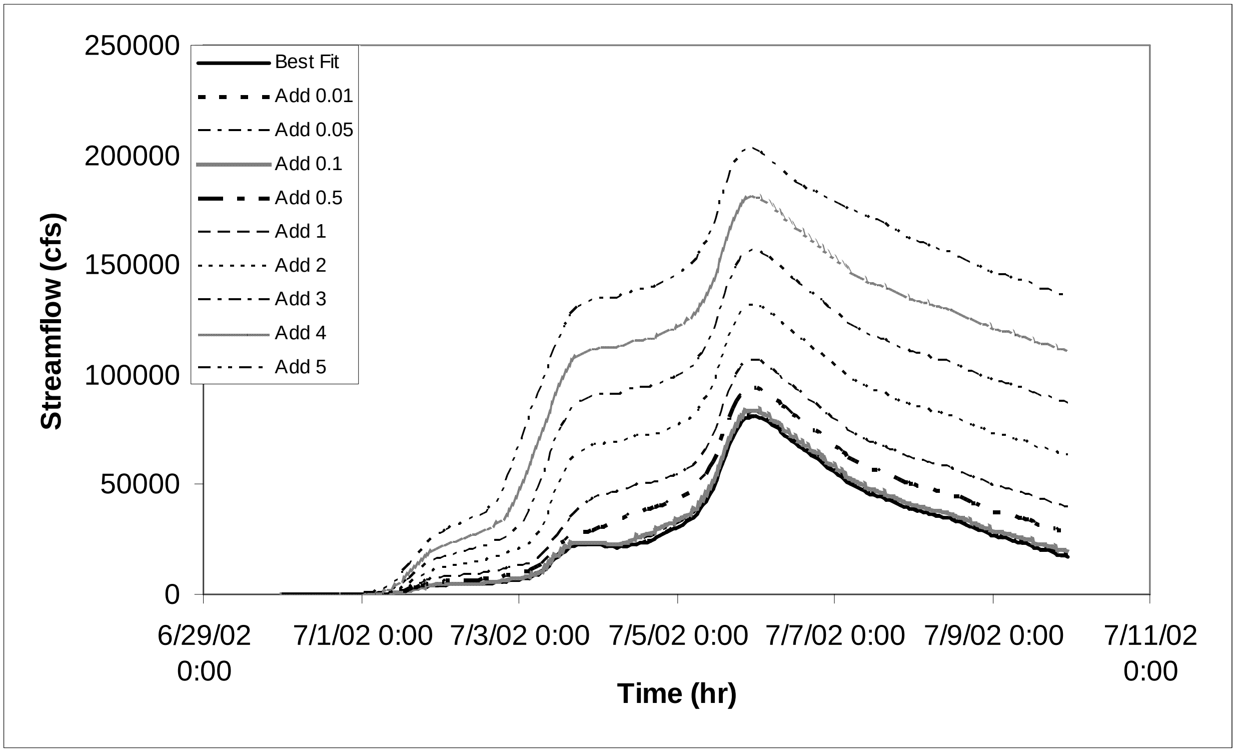

Figure 3.27a. Effect of positive rainfall intensity errors (mm/hr) on streamflow. Bold line is the output from best-fit WRF rainfall grid.

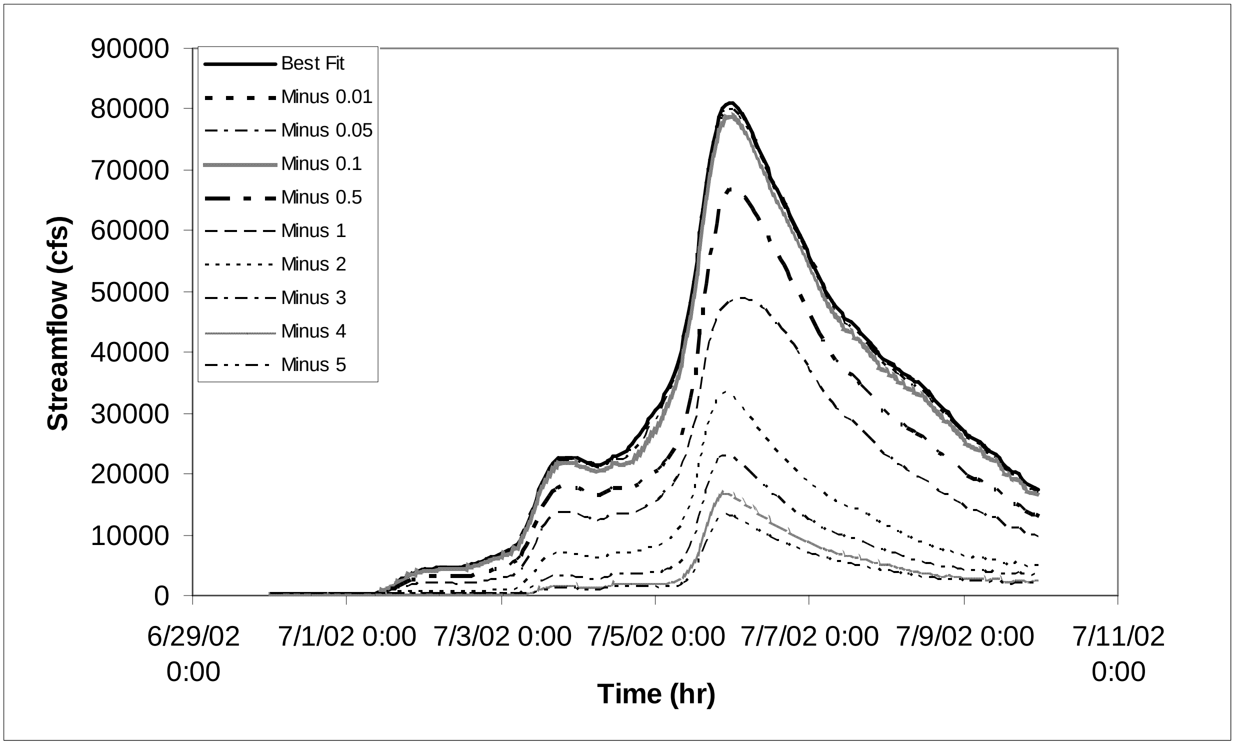

Figure 3.27b. Effect of negative rainfall intensity errors (mm/hr) on streamflow. Bold line is the output from best-fit WRF rainfall grid.

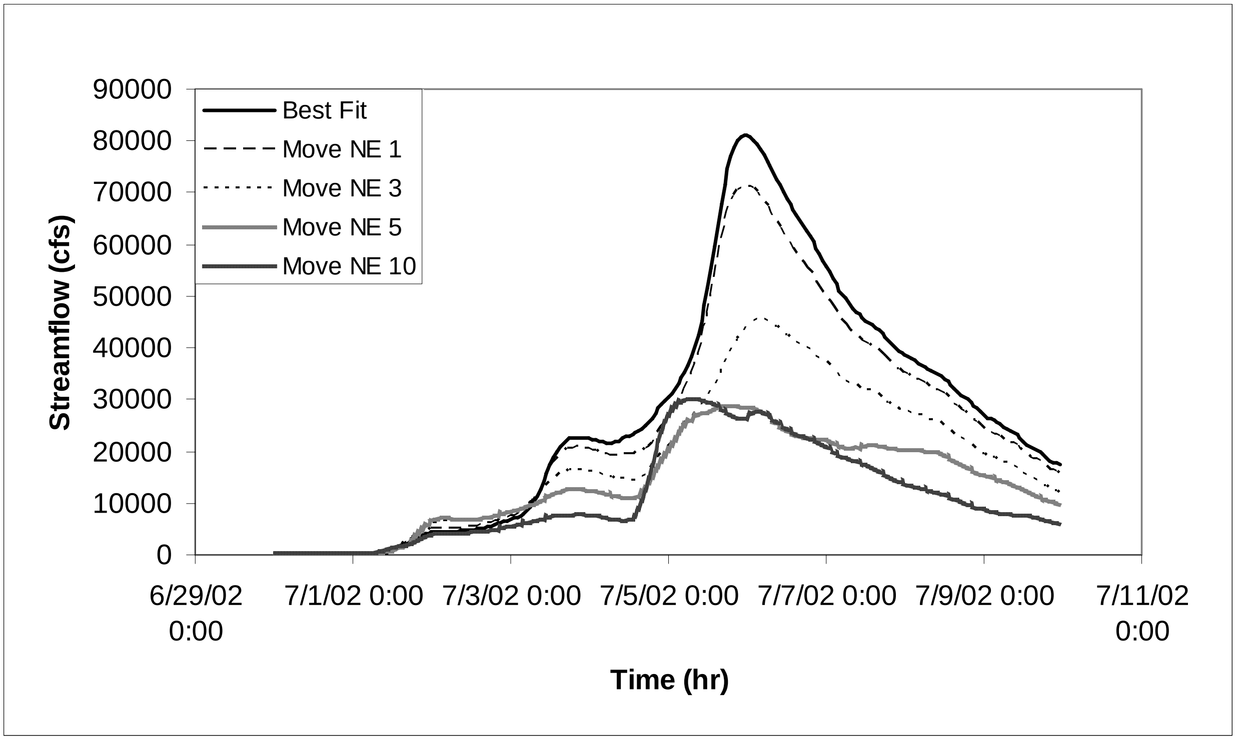

Figure 3.28a. Effect of rainfall location errors on streamflow. Units are number of grid cells that the best-fit output is shifted (a) northeast; (b) northwest; (c) southeast; and (d) southwest. . Bold line is the output from best-fit WRF rainfall grid.

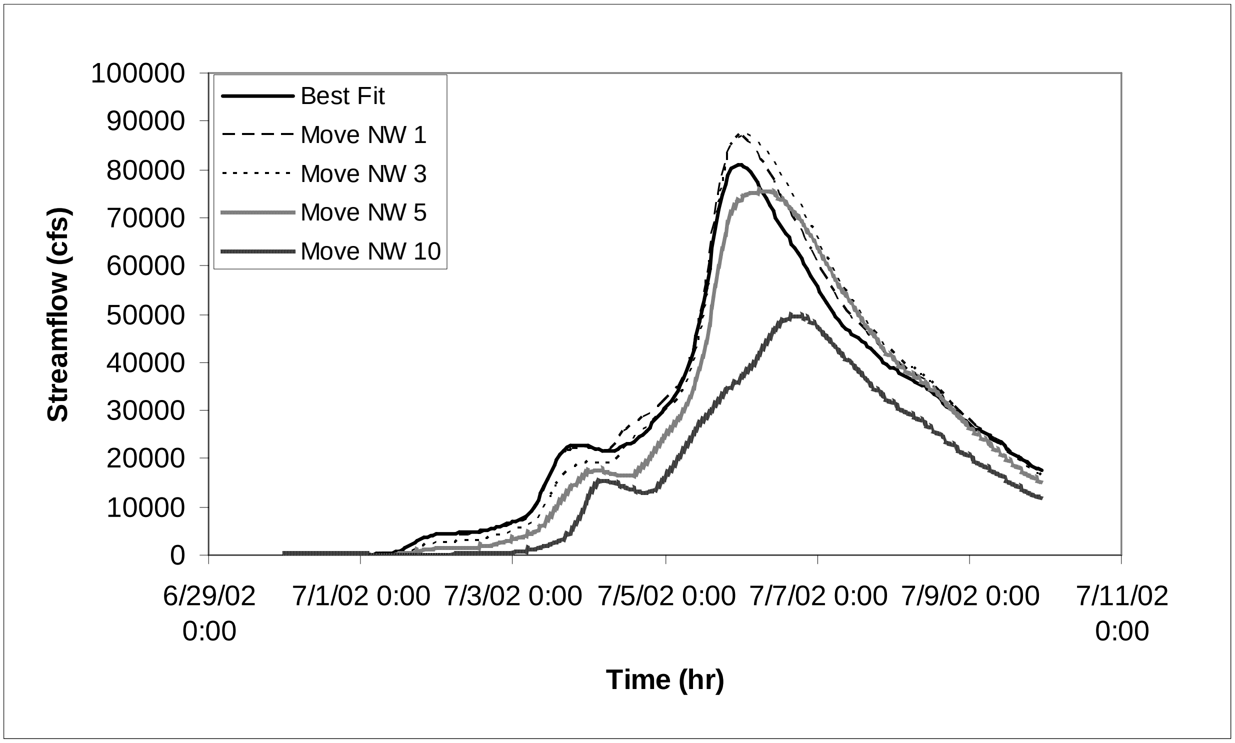

Figure 3.28b. Effect of rainfall location errors on streamflow. Units are number of grid cells that the best-fit output is shifted (a) northeast; (b) northwest; (c) southeast; and (d) southwest. . Bold line is the output from best-fit WRF rainfall grid.

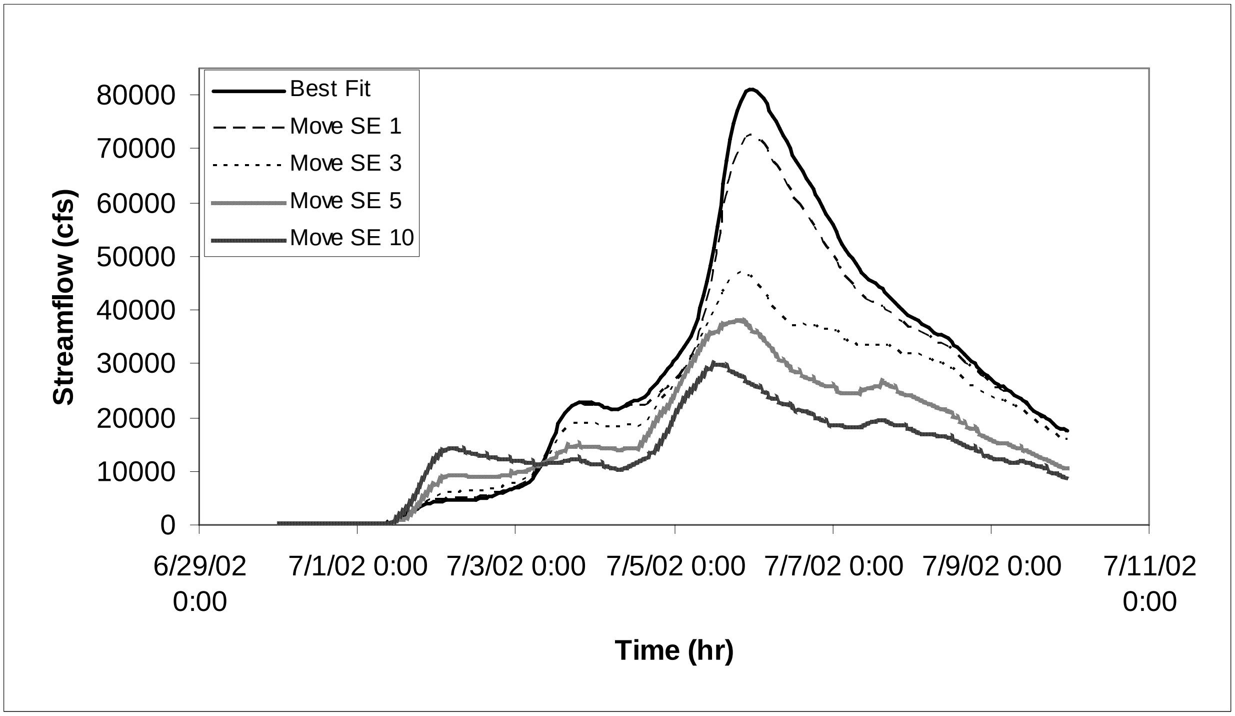

Figure 3.28c. Effect of rainfall location errors on streamflow. Units are number of grid cells that the best-fit output is shifted (a) northeast; (b) northwest; (c) southeast; and (d) southwest. . Bold line is the output from best-fit WRF rainfall grid.

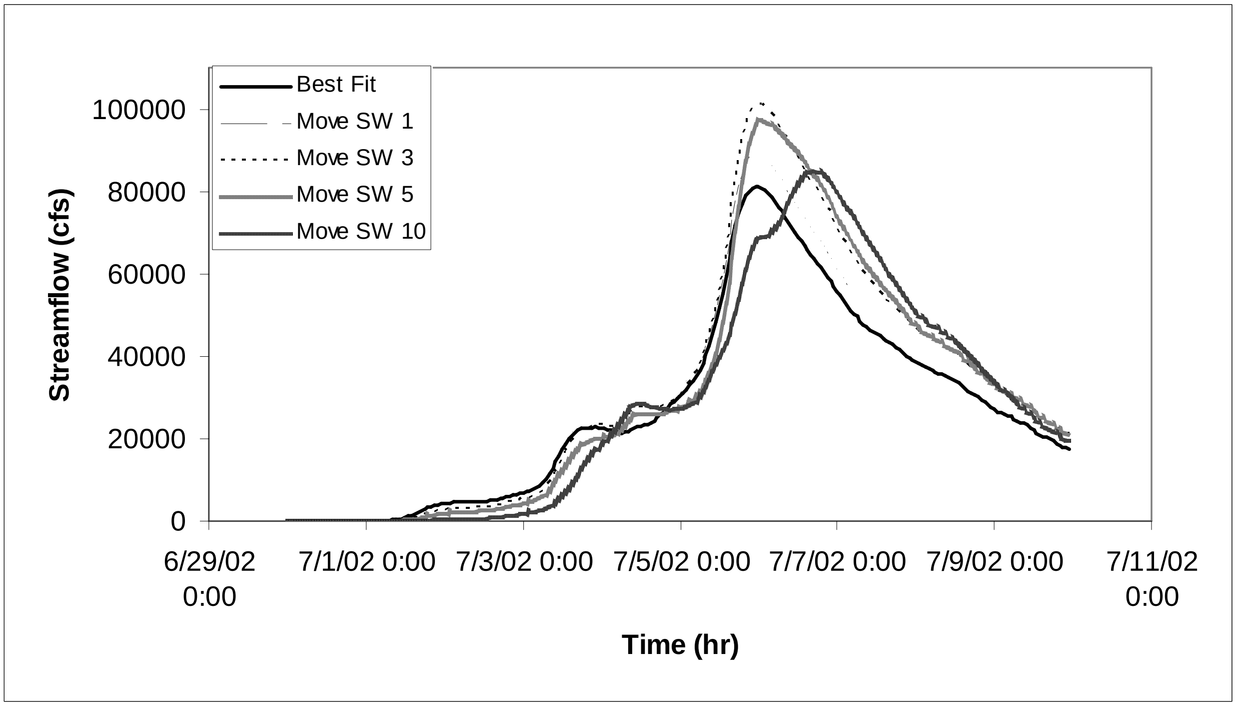

Figure 3.28d. Effect of rainfall location errors on streamflow. Units are number of grid cells that the best-fit output is shifted (a) northeast; (b) northwest; (c) southeast; and (d) southwest. . Bold line is the output from best-fit WRF rainfall grid.

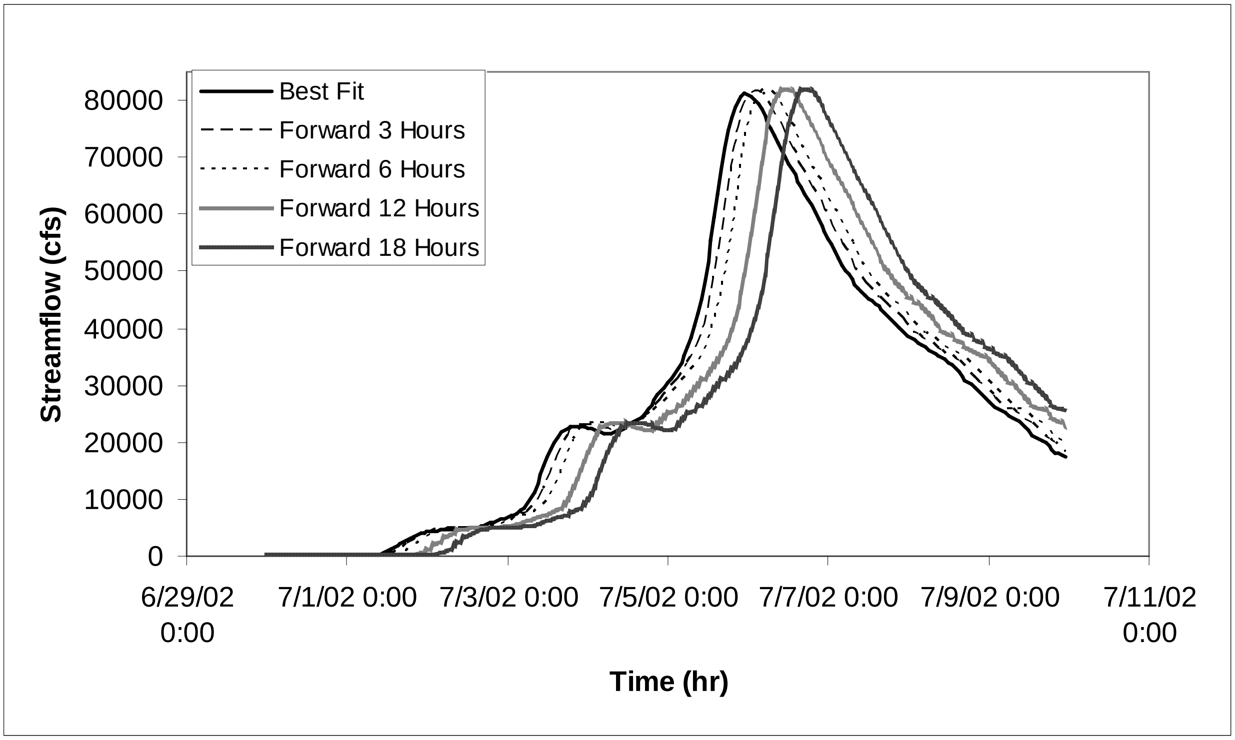

Figure 3.29a. Effect of rainfall timing errors on streamflow: (a) forward time error; (b) backward time error; and (c) peak shape error. Bold line is the output from best-fit WRF rainfall grid.

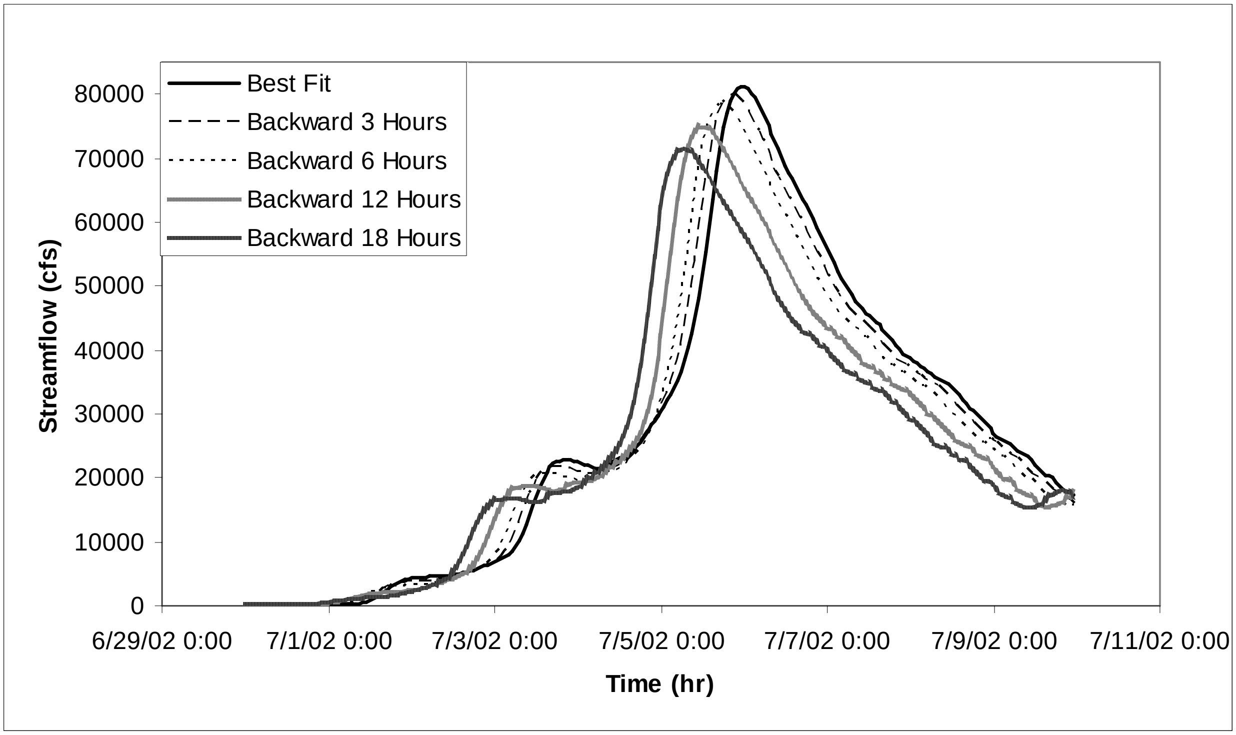

Figure 3.29b. Effect of rainfall timing errors on streamflow: (a) forward time error; (b) backward time error; and (c) peak shape error. Bold line is the output from best-fit WRF rainfall grid.

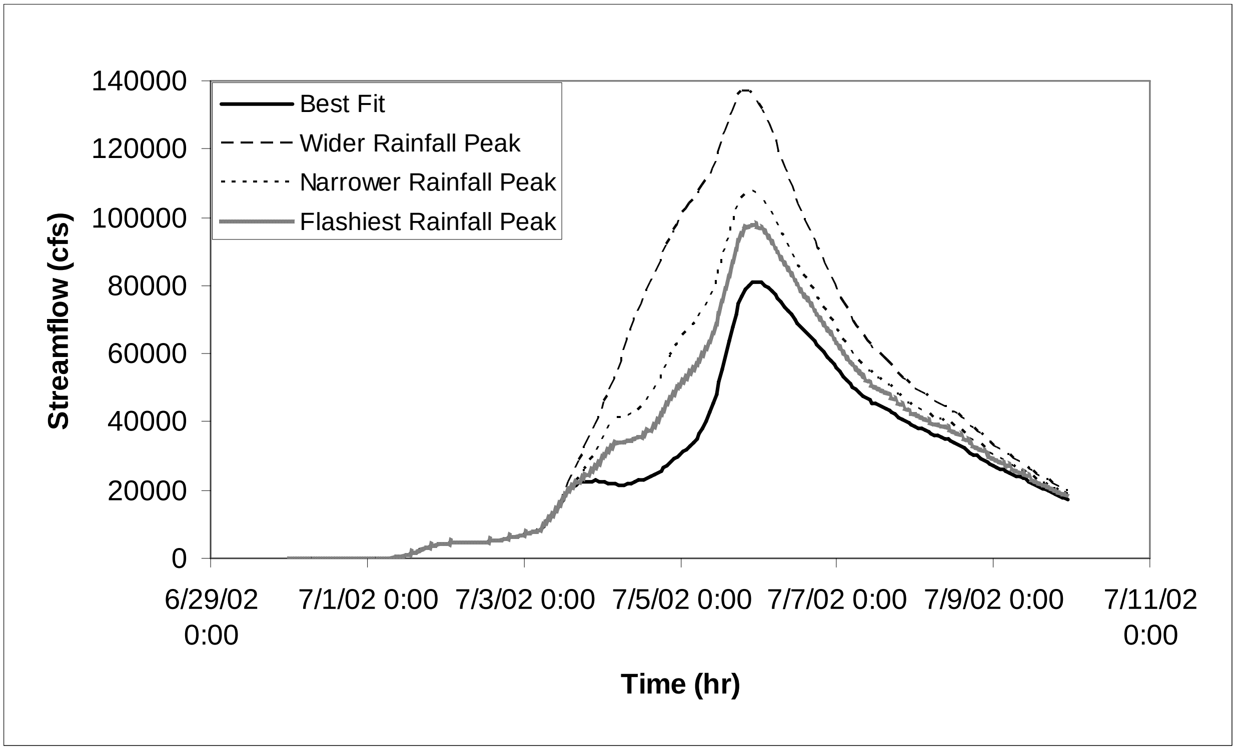

Figure 3.29c. Effect of rainfall timing errors on streamflow: (a) forward time error; (b) backward time error; and (c) peak shape error. Bold line is the output from best-fit WRF rainfall grid.

5. CONCLUSIONS AND IMPLICATIONS

This paper studies the sensitivity of WRF model precipitation forecasts to different physics, initialization, and domain configurations, and examines the ability of WRF to accurately reproduce a summer convective rainfall event. The propagation of error from rainfall to streamflow is investigated by applying a variety of perturbations to precipitation and finding relative significance of each in terms of streamflow.

WRF's ability to accurately simulate the 2002 central Texas storm event is most sensitive to cumulus parameterization, slightly sensitive to microphysics parameterization, and nearly unaffected by the choice of shortwave and longwave radiation schemes. The Betts-Miller-Janjic cumulus scheme combined with Lin microphysics produces the most reasonable rainfall over the San Antonio River Basin. Other cumulus schemes tend to underestimate rainfall intensity and shift the peak away from its true location. Contrary to modeling studies suggesting that high resolution domains have the ability to resolve convective motions on their own, this research found that simulation of the 11-day convective storm requires explicit convection in the inner 4-km domain.

A 48-hour initialization interval produces optimum performance in WRF, as determined by the high correlation values and low biases in both rainfall and streamflow. This interval allows WRF to successfully produce precipitation on its own, and the forecast is not substantially degraded, as in longer forecasts. Investigation of various domain configurations suggest it is best to avoid placing any domain over oceans or other regions lacking sufficient data. The relative size and placement of the parent and nested grid(s) are also important; to best simulate the combined effects of synoptic, mesoscale, and local atmospheric forcing, the nest must be close to the area of flood interest while keeping a significant distance from the parent domain. Results from this study suggest that a ratio of parent area to nest area of approximately eleven (as measured from the best-fit domain configuration) is ideal; of course, many factors influence domain effects and additional research using a multitude of different configurations is necessary to determine if such an ideal ratio actually exists. Additionally, studies of domain resolution should be undertaken; Zhang et al. (2006) found that a high-resolution (3.3-km) nest did not produce the best simulation (using the MM5 model) compared to coarser nest resolutions. It would be useful to test alternate resolutions to determine if forecast degradation occurs at high resolutions in WRF.

The best-fit WRF model accurately reproduces precipitation patterns and intensity over the warm-season, convective central Texas storm. Comparison of observed and modeled wind vectors at three different atmospheric levels suggest that errors in horizontal winds for the poor-performing WRF configurations may be a major factor in producing insufficient precipitation. There are several implications from the success of WRF in simulating the 2002 storm and subsequent streamflow. For data-sparse areas or International River Basins (IRB) nations that do not have access to upstream data, due to either lack of infrastructure or to lack of data-sharing between coincident riparian nations, WRF output can provide a proxy for such data. However, WRF may not increase lead-time enough to significantly improve flood forecasting in these regions. Additionally, WRF output can be used as the driving meteorological forcing data for regional and watershed-scale hydrological models.

Current numerical weather models categorically contain small errors associated with initial and boundary conditions, which result in errors in the precipitation forecast. This research investigates numerous perturbations to the WRF rainfall grid and their effects on streamflow output after running through a hydrological model. Results indicate that: 1) error dampening from rainfall to streamflow is greatest when the initial rainfall perturbation caused an increase in rainfall relative to the control; and 2) translation of error from precipitation to streamflow is strongly affected by surface characteristics such a topography, land use, and soils. Intensity and timing errors propagate fairly linearly to streamflow error, which therefore may be simpler to predict. Simulations that result in location error are most important because the effects of erroneous precipitation location on streamflow is dependent on the pattern of observed precipitation. Streamflow effects from these errors are nonlinear and difficult to determine for operational flood prediction.

The study of error in WRF may help to establish limits on acceptable rainfall error for flood forecasting of large events. For example, WRF rainfall errors less than or equal to +/-0.5 mm/hr appear to have a negligible effect on the quality of streamflow forecast, as do timing errors of 6 hours or less. This type of research can serve as a guideline to error estimation and correction in operational modeling with the WRF model. Further research is necessary, using a wider range of perturbation experiments, to better define the relative effects of different error types. Future publications on this subject should include more quantitative analysis, such as the growth rate of error for each perturbation type.

Chapter 4: Investigation Into the Geomorphic Variability of the San Antonio River Basin Floodplains, Texas, and its Effects on Watershed Hydrologic Response

ABSTRACT

Hydrological modeling begins with a thorough understanding of the watershed system. Geology, hydrology, geomorphology, topography, and land use combine to produce unique hydrologic responses at different parts of the system. In order to identify the variability in hydrologic response and understand the interconnections with basin geomorphology, hence improving modeling capability over the San Antonio River Basin, a detailed study of basin heterogeneity is undertaken.

The San Antonio River Basin is a 10,000 km^2 watershed located in South Central Texas. It receives frequent intense rainfall that periodically floods the basin's two principal rivers, the San Antonio River and the Medina River, and the many smaller creeks which comprise the watershed. The watershed is large but very well connected; rainfall on the northern portions of the basin can quickly cause excessive streamflow and flooding on the downstream portions of the basin, as was displayed in the July 2002 storm event, in which numerous gage heights exceeded historical records.

The variability of river and floodplain types and their possible effects on watershed response to rainfall over the San Antonio River Basin has not yet been studied. Damage incurred from flooding in this region is very great and both the natural and modified

floodplains need to be further investigated. Fluvial geomorphology, the study of floodplain structure and features, may be an important key to understanding floods at the watershed scale. Geomorphology can impart critical insight into: 1) river system responses to natural hazards; 2) river system responses to human-induced stresses, i.e., development and river modification; 3) river and floodplain evolution with time. This research is therefore important not only for classification purposes, but will aid in assessing flood impact for the region, and will provide a more thorough understanding of the system necessary for floodplain managers and scientists working on river modification or restoration.

The goal of this research is to use existing datasets to evaluate the variety of floodplains and rivers within the basin, and to then investigate possible impacts of these differences on hydrologic response. Differences across the basin in geology, soils, land use, land cover, topography, vegetation, climate, and floodplain structure are assessed. In addition, channel type and geometry are used in conjunction with the above data to extract information about levels of floodplain and river stability across the basin. The San Antonio Basin is divided into broad areas with similar geomorphic characteristics, and correlations are drawn between different areas and their respective responses to precipitation events. Finally, implications and suggestions for improved watershed modeling are introduced based upon the geomorphic analysis.

INTRODUCTION

Much of the elemental literature on basin response to a storm pulse surrounds small basins with very similar land characteristics across the catchment. Small basins were used to derive many of the hydrology equations used today in water resources engineering and planning (Chow, 1964). However, applicability and modification of these relationships requires knowledge of the unique characteristics of the particular basin under study. For many larger basins, there exists a wide variability in land characteristics; it is imperative that water resources managers and scientists understand this variability and its impacts on the hydrological system before attempting to begin a floodplain modification or restoration project.

The sizeable catchment area of the San Antonio River Basin contains both forested hills and coastal flatlands, urban and rural environments, and a complex pattern of soil and rock cover including the outcrop of a karst aquifer. The complex, heterogeneous nature of the area has not been addressed from a watershed perspective in previous studies (Abbott, 1975, Abbott and Woodruff, 1986, Sieh, 1975, Twidwell and Davis, 1987). Identification of similar floodplain and channel areas is necessary across the basin in order to identify areas that may behave similarly in response to a storm event; this knowledge is also extremely helpful for floodplain management and restoration.

Numerous datasets describing terrain and stream characteristics are available over the San Antonio Basin. This research delineates broad areas of the watershed according to spatial location relative to the drainage outlet (i.e., upper, middle, and lower river reaches), and based upon land cover characteristics and relative hydrologic behavior.

The results of this research allow a more thorough understanding of the interconnections between watershed characteristics and hydrologic response.

Previous Research

Researchers have classified floodplains and river systems in various ways, mostly dependent on the goals of the particular study (Table 4.1). One dominant classification scheme is simply the division of a watershed into the uplands and tributary reaches, the midstream reaches, and the downstream reaches (Jain and Sinha 2004, Knox 1977, Knox 2001). However, other characteristics such as stream order (Garnier et al. 2002), land use (Bryant and Gilvear 1999), soil texture (Descroix et al. 2001, Phillips et al. 2001), and vegetation (Detenbeck et al. 2005, Muller 1997) are valuable tools for identifying similar floodplain regions.

Aerial photography is useful to identify characteristics not available from outside datasets, or to validate existing data. It is ideal for examining floodplain characteristics over an entire watershed. For example, Ekwoanya and Ojanuga (2002) used aerial photography to recognize differences in upland and floodplain soil condition through evaluation of crop performance. Aerial photos allow analysis of channel type, the existence and location of abandoned channels, features such as terraces, fans, and deltas, and floodplain vegetation type and diversity, which implies the level of soil drainage (Marston et al. 1995). Vegetation type varies with different stream orders (Acker et al. 2003, Barker et al. 2002) which may aid in stream classification. The extent of overbank deposits and flood levels can be obtained from aerial photography not only directly after the overbank event itself (Colby et al. 2000), but the deposits and erosion patterns of floodplains can be mapped from photos of the area through change detection analysis (Nakamura and Kikuchi 1996). The San Antonio River Basin has not yet been studied for variability in floodplain and channel characteristics using aerial photography.

The history of floodplain evolution is evidenced in the modern floodplains and channels. For example, the existence of cutoff lakes implies a historical change of river course due to rapid bank erosion of bends, possibly catalyzed by a large flood event (Hooke 2004). Spatially, the variance in the amount of alluvium deposited (overbank sedimentation) is largely explained by valley width, stream power, and the presence of meander belts (Lecce 1997), given similar vegetation and climate regimes. Hence it is possible to infer information about floodplain evolution and previous conditions based upon existing data. Land use change is an important issue in current hydrological research, and abundant literature exists describing the effects of land use change on the rainfall-runoff response (Groffman et al. 2003, Harden and Matthews 2000, Leopold 1968, Wolman 1967). By understanding the relationships between land use changes and floodplain modification, evolution of the floodplain from a natural to developed state can be traced based on land cover data before and after cultivation.

Table 4.1. Classification of Various River Basins

Study	*Location*	*Division*	*Findings*
Bryant and Gilvear (1999)	River Tay, Scotland	Land use categories (18 classes)	Airborne remote sensing is a valuable tool for detecting geomorphic and riparian changes due to large flood events.
Descroix et al. (2001)	Western Sierra Madre, Northwest Mexico	Climate and relative water supply and consumption; surface textural features	Surface gravel crust greatly increases runoff and erosion.
Detenbeck et al. (2005)	Lake Superior, Minnesota	Hydrogeomorphic region, mature forest, watershed storage	Correlated fraction mature forest and storage with flow indices to clarify threshold values for flow metrics.
Garnier et al. (2002)	Danube River, Europe	Stream order	Geomorphological analysis by stream order aided in modeling of river nutrient delivery.
Jain and Sinha (2004)	Baghmati River, India	Upstream, midstream, downstream reaches; channel type	Characteristics of lower reaches are related to anabranching and frequent avulsions (such as a flood-induced levee break) in these reaches.
Jiongxin (2004)	North China	Perennial, seasonal, and anthropogenic seasonal (ASR) rivers	A combination of natural and human factors converts perennial streams to ASR streams, partially due to excessive water diversion by humans.
Knox (1977)	Platte River system, Wisconsin	Upland streams and tributaries, middle reaches, downstream reaches	Post-Urbanization: Upland streams became much wider, more bedload sediments, greater erosion. Lower reaches showed narrower cross-sections, increased deposition due to low gradient and backwater effects, and a larger suspended load.
Knox (2001)	Upper Mississippi River	Headwater tributaries, down-valley tributaries, main valley	While small headwater tributaries have undergone decreases in flood frequencies in recent years, the main valley has experienced increased frequency of large floods.
Leopold (1968)	Various USA (combination of studies)	Percent impervious area Percent sewered area	Areas with at least 20% imperviousness and 20% sewered more than doubled the pre-urbanization peak discharge (when compared to post-urbanization peak discharge)
Muller (1997)	Various	Riparian vegetation types	Aerial photographs provide representation of riparian vegetation classification.
Phillips et. al (2001)	Bear Creek, Tennessee	Soils and slope (of floodplain and nearby areas)	Slopes and soil features such as clay plugs (aquicludes) affect the basin runoff response, which then affects the level of weathering.
Rosgen (1994)	Various	Entrenchment, gradient, width/depth ratio, and sinuosity	Development of a stream classification system with implications for channel stability, form, and process.

Many factors contribute to the hydrologic response of watersheds. Soil and rock texture is a major control; coarse gravelly or sandy soils promote infiltration, while silt and clay rich soils increase runoff (Dingham 2002). Descroix et. al (2001) described the main control on erosion and runoff as the presence of an embedded soil crust at the surface in the Western Sierra Madre, Mexico. Karst systems are generally controlled by conduit and fracture porosity during precipitation events (Halihan et al. 1999, Halihan et al. 1998, Mayer and Sharp 1998) and therefore these areas are dominated by flashy hydrologic responses. Topography also exerts control on floodplain response, as steep slopes tend to increase runoff while decreasing infiltration (Phillips et al. 2001). These factors combine to produce the dampening response of streamflow to precipitation demonstrated in all basins; variability in these basin characteristics will manifest a different streamflow for the same precipitation (Smith et al. 2004).

At the stream channel scale, factors such as the shape and geometry of a channel/floodplain system may affect flow and sediment transport. For example, narrow floodplains (low valley width) confine the channel, increasing velocity and sediment transport. Wide floodplains allow significant overbank sedimentation during flood events, which may result in lateral migration and the formation of meander belts, which in turn increases the system's capacity to contain large floods (Lecce 1997). Drainage density describes the relative timing of storm response in the system, and may increase with urbanization (Paul and Meyer 2001). Development of an area also has shown to increase channel width in the uplands and tributary streams, while causing increased sediment deposition and in some cases a narrowing of streams in downstream areas of the basin (Knox 1977, Wolman 1967).

Land use and cover has a striking effect on runoff response that has been well-documented. Knox (2001) found that for all spatial scales in a watershed, agricultural land use increased runoff from events of various recurrence intervals, and increased erosion and sediment yield to rivers. Tree cover, surface litter, and organic matter in the soil intercepts precipitation and decreases runoff (Descroix et al. 2001, Harden and Mathews 2000). Detenbeck et al. (2005) found that the loss of mature forest increased the range between peak flows and baseflows, and decreased baseflow values. Similarly, the presence of impervious cover such as concrete and rooftops increases flood discharges during high-flow periods and reduces baseflow during low-flow periods (Leopold, 1971). The location of impervious cover is also significant. Impervious surface cover (ISC) concentrated in the lower portions of a catchment drains more quickly (than forested uplands regions), lowering the flood discharge and duration (Hirsch et al. 1990, Paul and Meyer 2001). One negative feedback mechanism due to urbanization is the proliferation of dams, which has reduced discharge magnitude and frequency beyond historical climatic alterations (Magilligan et al. 2003).

A common consequence of urbanization is a concept known as hydrologic drought, where high levels of development decrease infiltration while increasing stream incision (Groffman et al. 2003, Schilling et al. 2004). As the channel water elevation decreases and baseflow is also reduced, the riparian water table lowers, disconnecting (part of) the riparian zone from the floodplain system. This disconnect is important in altering soils,

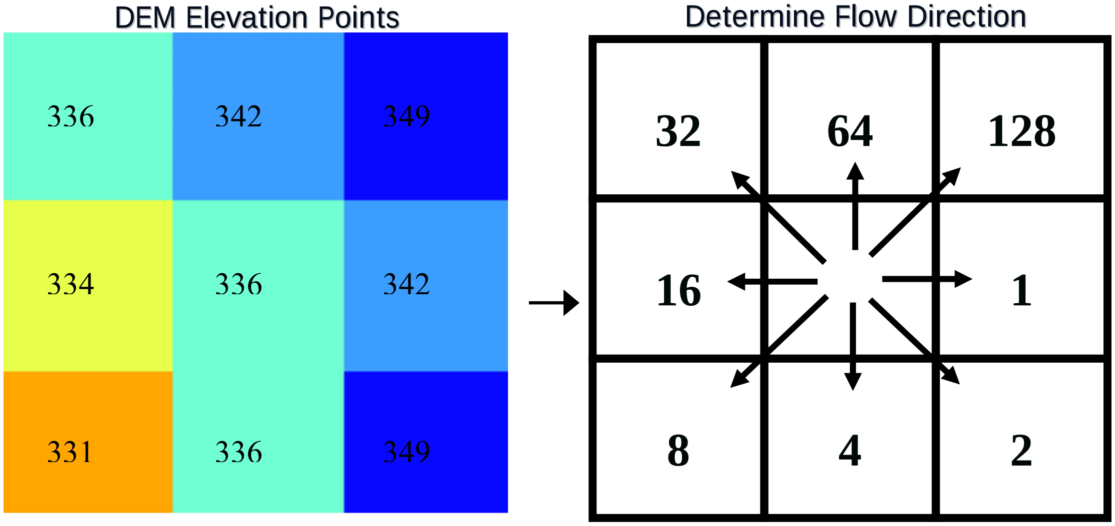

DEM Elevation Points

336	342	349
334	336	342
331	336	349

Determine Flow Direction

32	64	128
16		1
8	4	2

Source: D. Maidment

Figure 4.1. Eight-direction pour point model for stream and subbasin delineation, based on DEM. Elevation values are shown in meters above sea level.

vegetation, and microbial processes, and may be identified by the presence of upland vegetation in riparian areas. Riparian vegetation thrive in a shallow water table environment; increased depth to water table results in the replacement of riparian vegetation with deeper-rooted trees and brush normally confined to upland areas.

DATA AND METHODS

The main investigations for the study area are as follows: 1) broad identification of river system into uplands/tributary, midstream, and downstream areas based on cursory descriptive data such as channel type, drainage density, and topography; 2) investigation of geology, land use, soils, and vegetation over these different areas; 3) attainment of key geomorphic measurements (bankfull/floodplain widths, slope, sinuosity); 4) geomorphic description of floodplain and channel characteristics; and 5) correlation of hydrologic response to the variable characteristics of these identified areas.

Numerous data were available for the above investigations. Terrain data were obtained as a Digital Elevation Model (10 meter resolution) and USGS 1:24,000 topographic maps, which were analyzed in GIS to derive floodplain slope and, to a more limited extent, channel slope (%). DEM data were used to derive the stream and subbasin network in the San Antonio River Basin using the eight-direction pour-point model, where water in each grid cell is allowed to flow in one of eight surrounding cells (Figure 4.1; see also Chapter 2), and streams are defined by a threshold cell accumulation (in number of cells). Soil/rock texture and properties were determined using STATSGO and SSURGO datasets. These soil datasets are hydrologically relevant databases containing over six rock and soil layers and numerous soil properties such as permeability (ms^{-1}), organic matter content (%), and clay content (%).

Additional soil data was obtained via individual soil maps and drilling logs from the Texas Water Development Board, as necessary. Vegetation data was obtained from the National Land Cover Dataset (30 meter resolution), as well as more detailed observations from aerial photographs. The vegetation and soil datasets were combined with additional data on karst features from the Texas Speleological Society to identify areas of similar infiltration and runoff capacities, using a modified curve number method (U.S. Soil Conservation Service 1986; see also Chapter 2). In addition, relevant literature on the Central Texas area was perused for pertinent information.

Aerial photographs downloaded from the Texas Natural Resource Information Service (TNRIS 2005) provided valuable information along the floodplain. Approximately 250 aerial photographs, of one meter resolution, were downloaded and merged in ArcGIS 8.3. Cursory analysis consisted of large-scale identification of geomorphic change across the basin. Initial observations included channel type and channel density. Based upon these observations and geologic setting, the watershed was divided into upland, midland, and lowland regions (see below for further detail). Six representative aerial photos were chosen for further analysis: Medina River Uplands, Medina Lake Outlet (upstream); San Antonio River near downtown, San Antonio River at its confluence with the Medina River (midstream); San Antonio River at its confluence with Cibolo Creek, and San Antonio River at Goliad (downstream).

In addition, floodplain and channel stability was observed through analysis of existing scour, erosion, and depositional features, abandoned channels, and modification structures such as dams. Vegetation differences along the floodplain as observed in the aerial photographs may provide indicators of hydrologic drought due to development. Finally, geologic features such as the Balcones Fault Zone and the Edwards Aquifer outcrop were considered when classifying and analyzing the various basin areas.

Watershed Subdivision

Although there exists a number of possible criteria by which to subdivide the San Antonio River Basin (Table 4.1), ultimately it was decided that the presence of the Balcones Fault Zone and coincident Edwards Aquifer was the most significant geologic and geomorphic characteristic of the basin. The Balcones Fault Zone, located in the middle of the basin just north of San Antonio, impacts numerous aspects of the watershed, including basin recharge, infiltration, topography, precipitation, and water quality (Abbott and Woodruff, 1986, Abbott, 1975, Arnow, 1959, Maclay and Small, 1984, Senger and Kreitler, 1984, Puente, 1978, Walker, 1979, Woodruff and Abbott, 1979). Hence, basin subdivision was centered on these two features.

Table 4.2. Calculation of Geomorphologically Significant Variables

Variable (units)	Method of Determination
Bankfull Width (m)	Estimated from aerial photographs; determined from vegetation lines.
Floodplain Width (m)	Estimated from aerial photographs; determined from slope lines.
Channel depth (m)	Measured from cross-sections perpendicular to streamflow
Width-to-depth ratio	Bankfull Width / Channel Depth at thalweg (deepest part of channel)
Drainage Density (1/m)	Total length of streams / drainage area
Channel slope	Change in distance / change in elevation; parallel to stream.
Floodplain slope	Change in distance / change in elevation; perpendicular to stream.
Sinuosity	Length of stream (thalweg) / straight line distance

Geomorphology

Geomorphic measurements (Table 4.2) were obtained both through topographic data and aerial photos. Bankfull width is the top width of the channel when water depth is great enough to inundate both left and right banks; this width generally corresponds to a streamflow with a 1.5 year recurrence interval. Bankfull width is a significant parameter because the 1.5 year storm event is widely believed to shape the channel more than any other event (Wolman and Miller 1960). Floodplain width describes the extent of flood effects in terms of ecologic support; riparian vegetation and organisms in this area depend on periodic inundation and overbank deposits for habitat support. The location and density of features such as oxbow lakes, abandoned channels, crevasse splays, cutoffs, channelization structures, devegetation and scour were recorded in order to develop a description of geomorphology and anthropogenic disturbance.

The width-to-depth ratio was used to measure the level of incision in a stream reach. The more incised a channel, the more likely that the channel bed will intersect the water table, which may create a drain or sink for groundwater, depending on the local hydraulic gradient (Abbott and Woodruff, 1986, Chen and Chen, 2003). Sinuosity measurements enabled the determination of flood response characteristics; straight channels are often bedrock-controlled and therefore tend to incise vertically to create room for more discharge. Highly sinuous reaches, however, tend to erode laterally into alluvium during periods of high discharge, resulting in lateral movement of the meanders within a larger meander belt (Wolman and Miller 1960).

Although geomorphic forms generally control fluvial processes, during large flow events, fluvial processes control and shape channel form (Graf, 1983). One way to quantify this impact is through measurements of stream power. Stream power can be defined as the rate of energy supplied by flowing water per unit length of a channel. Using Bagnold's (1966) approach, it is calculated as

$$\omega=\rho gQS/w \tag{1}$$

where ω = unit stream power in W/m^2, ρ is the density of water (kg/m^3), g is the acceleration of gravity (m/s^2), Q is the discharge (m^3/s) of a given return period or geometric level, S is bed slope (dimensionless), and w is channel width (m). For this study, bankfull discharge was chosen as a representative discharge because it is assumed to have the greatest impact on channel formation, and hence may be most important to quantify the work done on a channel by streamflow. Since discharge is the product of velocity and area, it can be indirectly calculated using the Manning equation,

$$V = n^{-1} R^{0.67} S^{0.5} \tag{2}$$

where V is the channel velocity, n is the roughness coefficient, and R is the hydraulic radius, calculated as the cross-sectional area divided by wetted perimeter. The calculation of stream power assumes a steady uniform flow, which is a reasonable assumption for mean flow conditions.

Stream power and its variation along a river network are the driving force for sediment transport, and affect channel shape, erosional capabilities, bedrock channel incision, and riparian habitat development (Jordan and Fonstad 2005). Stream power distribution can be related to the distribution of accumulated sediment (Graf 1983). For example, in a depositional setting, stream power decreases in the downstream direction, depositing more overbank sediments downstream and retaining channels at a relatively shallow depth. Large flow events cause erosion of channel beds, deepening the channel and increasing stream power in the downstream direction.

Channel geometry measurements were obtained from cross sections, while slope and roughness coefficients were derived from GIS-based topography and land use coverages.

Hydrology and Hydrogeology

Once the available datasets were applied in order to characterize similar areas of the San Antonio River Basin, hydrologic data over the region were studied to characterize the rainfall-runoff responses of the areas as a function of their distinctive traits. Data obtained for this purpose included historical hydrograph and stage data from the USGS, hyetographs from the various weather sources, and water levels as recorded in Texas Water Development Board (TWDB) wells. These datasets aided in studying the variability of hydrologic response in terms of flow magnitude, volume, and lag time between precipitation and streamflow pulses. Low flow time series data were extracted and analyzed to observe changes in the system induced from climate and human influence.

RESULTS AND DISCUSSION

Aerial photographs over the basin, in combination with relevant literature and other GIS datasets, allowed a clear delineation of the watershed into upstream, midstream, and downstream sections, as discussed subsequently.

Geologic History

The formation of the Edwards Aquifer (Figure 4.2) greatly altered the hydrology of the region by modifying the landscape into a complex system of recharge and discharge points, incised streams, and cavernous porosity. The aquifer and corresponding fault zone separates the region into three distinct areas: the Edwards Plateau and Hill Country to the north, the Gulf Coastal Plain to the south, and the intermediate Balcones Fault Zone. During the Early Cretaceous, vast amounts of clastic and carbonate rocks were deposited onto the shallow seas then covering Texas. This solid Edwards limestone had a low primary porosity. In the Middle and Late Cretaceous, the San Marcos Platform was uplifted, followed by the erosion of more than 30 meters of the Edwards Limestone (Abbott and Woodruff, 1986). Meteoric water began circulating through the underlying Glen Rose formation, enhancing porosity via carbonate dissolution. During the Miocene, a period of severe faulting occurred, resulting in a series of en echelon, down-to-the-coast faults along a NE-SW line known as the Balcones Escarpment. This fracture-enchanced porosity further concentrated dissolution and increased storage in the limestone. South of the escarpment lies the artesian zone, where the Edwards is covered by aquiclude layers such as the Del Rio Clay.

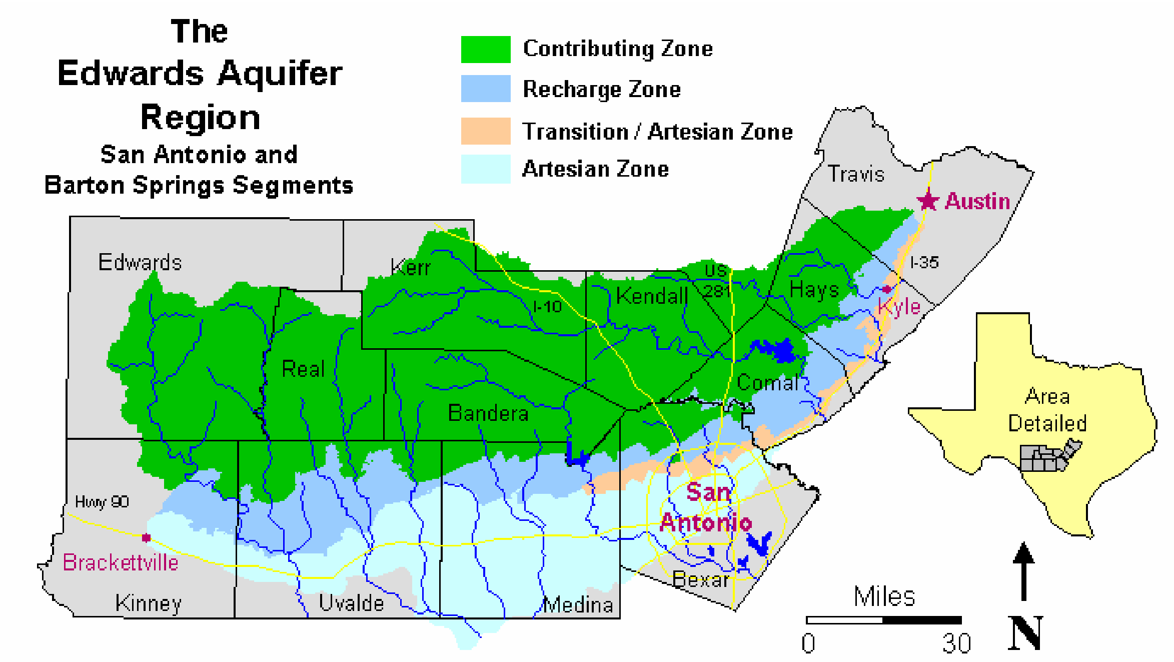

Figure 4.2. Edwards Aquifer crossing the San Antonio River Basin, showing the contributing, recharge, and artesian zones. Source: G.Eckhardt

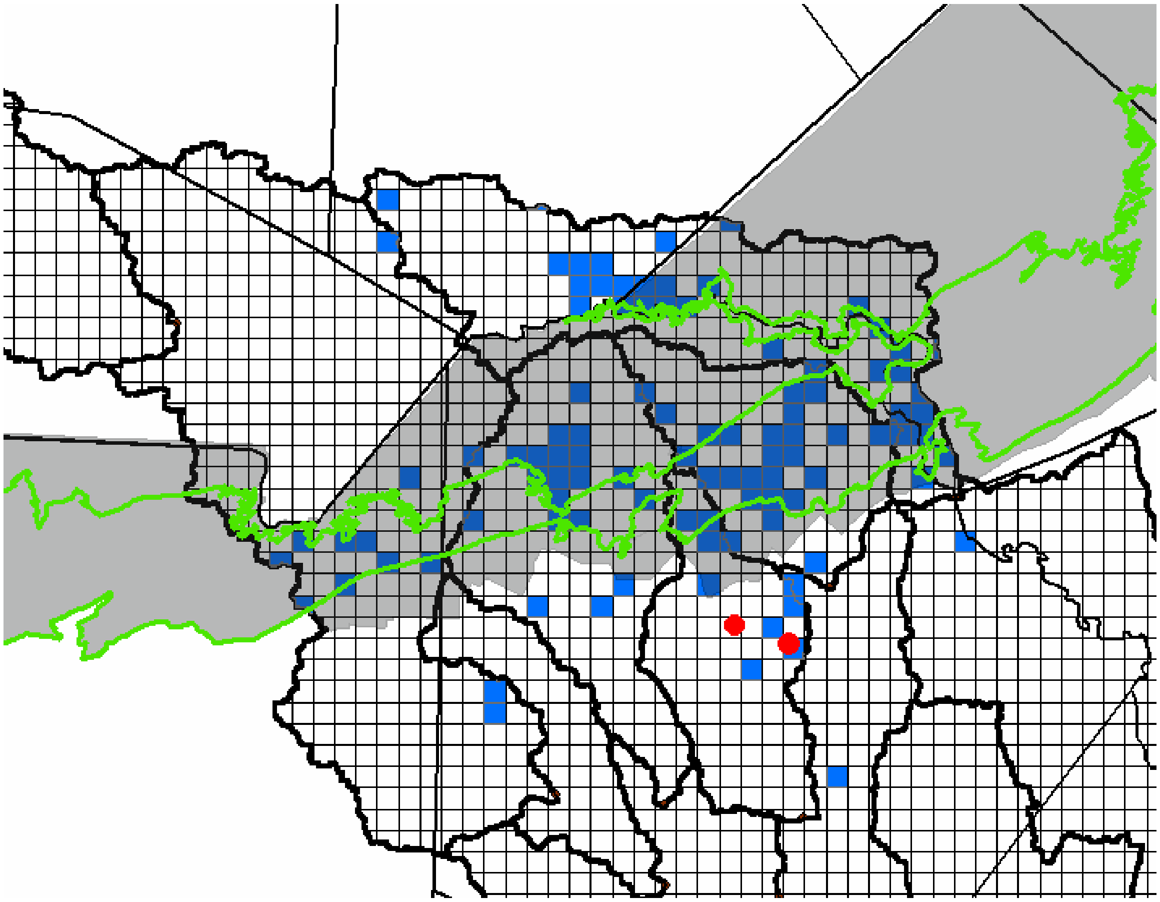

Figure 4.3. Balcones Fault Zone region of the watershed, showing major recharge points (caverns; blue) and discharge points (springs; red). Shaded area represents the Edwards Aquifer. Aquifer recharge zone is outlined in green.

The Balcones faulting event displaced streams and caused numerous cases of stream piracy along the escarpment. These pirate streams eroded existing fine-grained alluvium, exposing limestone and downcutting the rock to create recharge/discharge points for the underlying aquifer (Figure 4.3). The Edwards Aquifer runs 280 km from higher elevations at Brackettville in the SW to lower elevations at Kyle in the NE. The contributing zone consists of dissected Hill Country terrain where streams cross over the Glen Rose limestone. The recharge zone occurs in the Balcones Escarpment vicinity, and is characterized by an abrupt flattening of topography, and numerous recharge points.

Climate

Weather and climate in the Central Texas region is unique from any other part of the country. The frequency of severe floods along the Balcones Escarpment is the highest in the nation (Abbott and Woodruff 1986). Both geology and climate play a role in creating flood conditions. Orographic uplift of air masses at the escarpment induces condensation and intense rainfall. Additionally, Central Texas is a zone of convergence for large-scale air masses (Figure 4.4). Some of the most intense precipitation-inducing storms occur during the summer, when a maritime tropical (mT) air mass from the Gulf of Mexico moves inland over the state. This Gulf air can stall over Central Texas for a week or more, depositing heavy, prolonged rainfall as during the July 2002 storm. Hence, changes in weather and climate patterns modify the region’s susceptibility to flooding. Large-scale climate patterns such as El Nino-Southern Oscillation can greatly affect streamflow and water balance in river systems (Miles et al., 2000); several research efforts have been directed at predicting streamflow from climate data (Garen, 1998, Hamlet and Lettenmaier, 1999).

Local climate varies within the basin as well, largely as a function of proximity to the Gulf Coast. Climate is semi-arid to subhumid, with temperatures ranging from a high of 35 degrees Celsius in July to a low of 1 degree Celsius in January. Southeastern portions of the basin receive greater average monthly rainfall, especially during the wet season, from the frequent influx of moist Gulf air (Figure 4.5). Monthly average temperatures remain relatively consistent across the basin, showing a slight increase from the northwest to the southeast. During the summer months, San Antonio maintains a higher average temperature than areas south of the city. One possible explanation for this reversal is the urban heat island effect, where the increased absorption of solar radiation by dark surfaces and lack of vegetation cause urban areas to have temperatures 6-8 degrees warmer than surrounding regions (Pomerantz et al. 2000). Lake surface evaporation increases from the more humid eastern region to the drier western region, where surface-air moisture gradients are large.

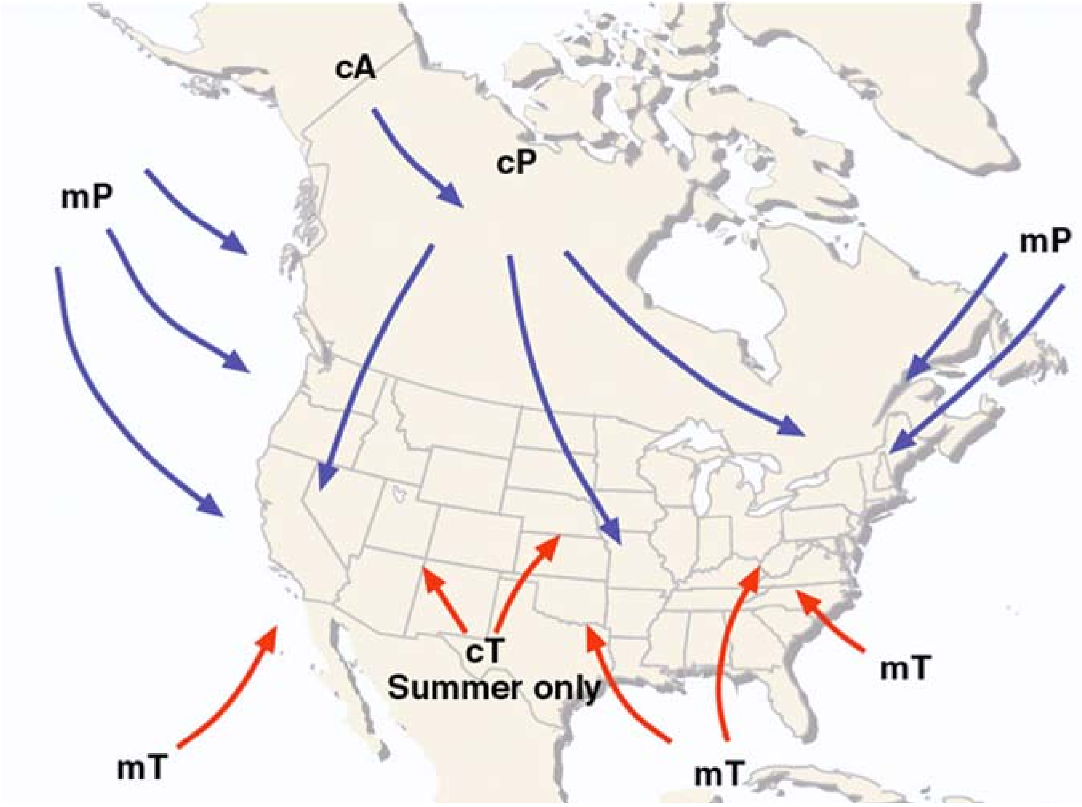

Figure 4.4. Generalized diagram of large-scale air movement over the North American continent. mP = maritime polar air mass; mT = maritime tropical air mass; cT = continental tropical air mass; cP = continental polar air mass; and cA = continental arctic air mass. Source: Ahrens 2005.

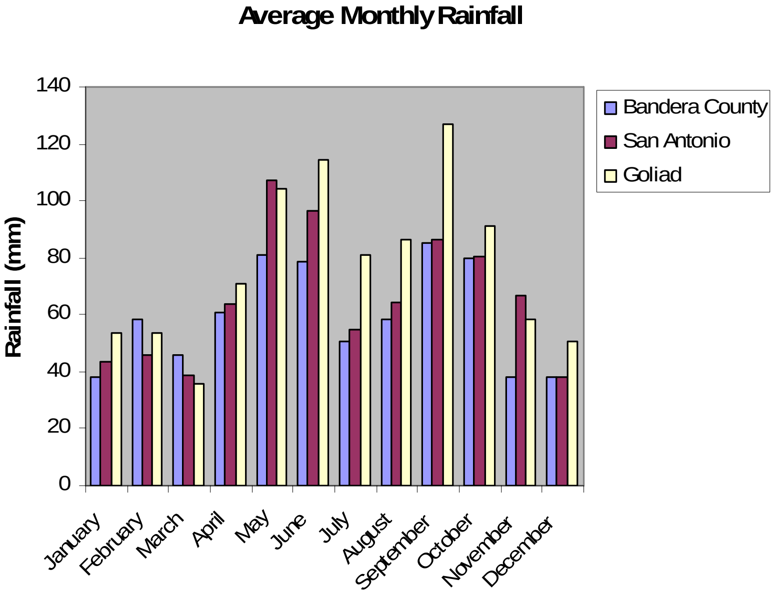

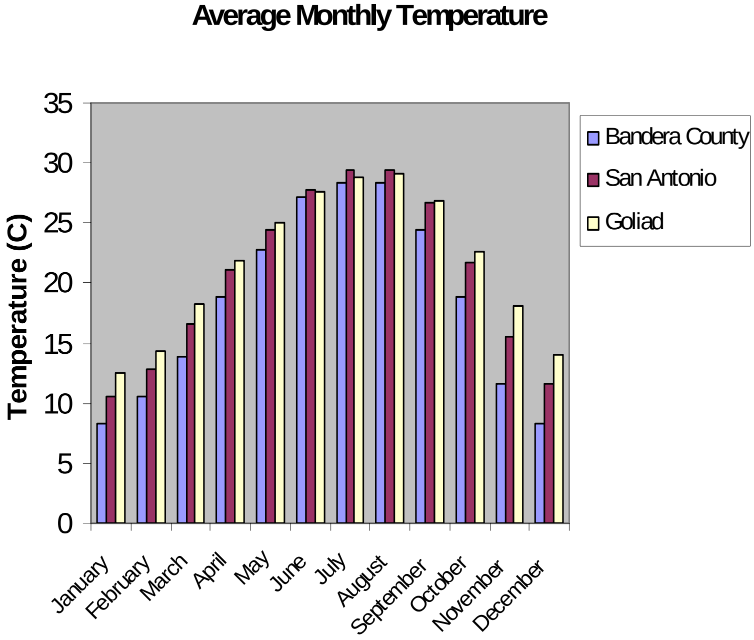

Figure 4.5. Average monthly precipitation and temperature for the upstream (Bandera County, blue), midstream (San Antonio, red), and downstream (Goliad, yellow) basin regions.

Land Use, Vegetation, and Soils

The San Antonio River Basin extends from the Hill Country area near Bandera to the town of Goliad in the coastal uplands region. Land use in the uplands portion of the basin is dominated by rangeland, as well as forested riparian areas (Figure 4.6). Table 4.3 and Figure 4.7 compare land use (percent area) for the three basin areas. This Texas Hill Country, an area of undulating hills, woodlands, savannah, and grassland, lies at relatively high elevations (250-750 meters above mean sea level), and has soils consisting of coarse textured sands and alkaline soils underlain by limestone and limy soils. The thin soils of the region are not conducive to farming and hence much of the region remains undisturbed, as is apparent in aerial photos. The dominant riparian corridor vegetation is ash juniper, which flourishes in the Hill Country's calcareous soils.

The midstream reaches of the basin are characterized by the strongly dissected Balcones Fault Zone, and the city of San Antonio, a sprawling urban center lying in the middle section of the basin just south of the Balcones Escarpment. This highly developed landscape is underlain by a wide variety of juxtaposed soil and rock layers due to fault displacement. Limestone to the northwest is juxtaposed with chalk, marl, and claystone to the southeast, including the agriculturally rich Blackland Prairie soil. Karst terrain in the Balcones Fault Zone vicinity consists of abundant sinkholes, artesian springs, and underground caverns (Figure 4.3). The vegetation is mostly mixed-oak woodlands such as post oak, live oak, cedar elm, and Texas oak. Southeast of the escarpment lies widely-spaced trees in a mixed grassland, including oak, elm, hackberry, pecan, ash, and cottonwood (Abbott and Woodruff, 1986).

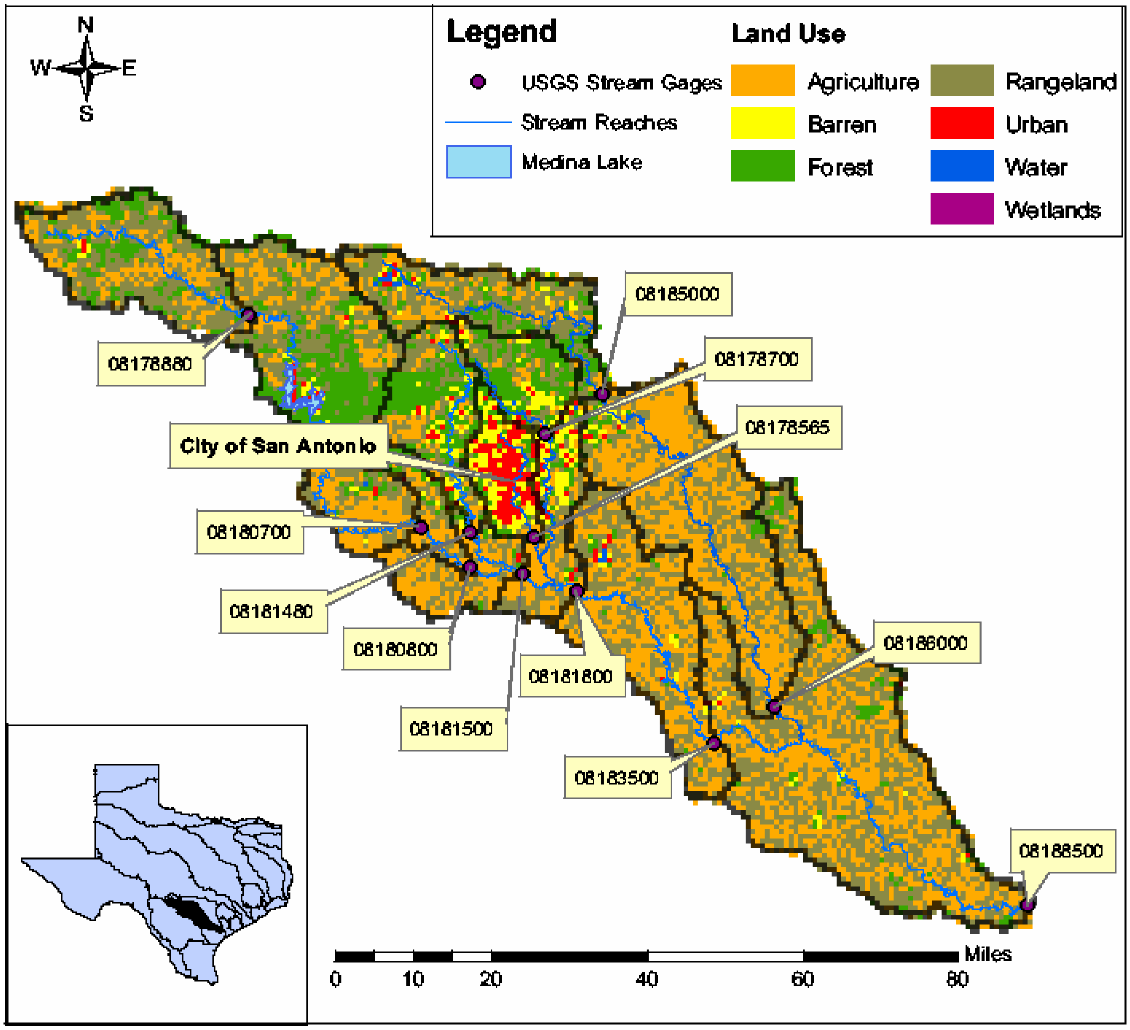

Figure 4.6. Map of the San Antonio River Basin, Texas, demonstrating the large variety of land cover in the watershed.

Table 4.3. Comparison of land cover between basin regions, in percent.

Basin Region	Upstream	Midstream	Downstream
Residential	2	14	< 1
Commercial	< 1	6	< 1
Deciduous Forest	4	10	13
Evergreen Forest	58	13	6
Shrubland	12	13	24
Grassland	17	6	18
Pasture/Hay	2	21	23
Row Crops	1	11	13

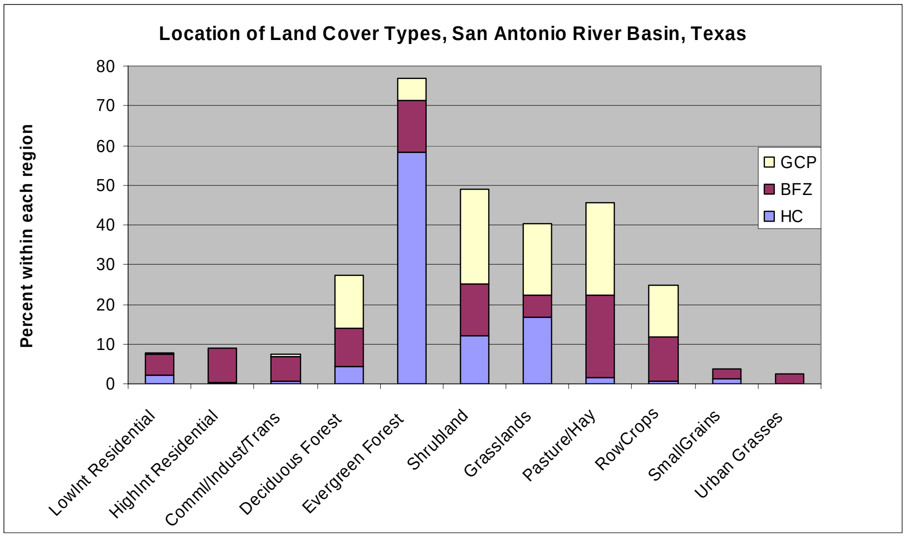

Figure 4.7. Comparison of land cover types for the various basin regions: Hill Country (blue); Balcones Fault Zone (red); Gulf Coastal Plain (yellow).

The downstream portions of the basin reflect a more coastal origin, with lower slopes and a dominantly agricultural land use. Soils of the region include light to dark loamy soils, some sandy and clay loams, and reddish to black clayey subsoils with high shrink-swell potential. Vegetation includes grasslands, mesquite, post and live oak, pecan, and brush.

Geomorphology

The uplands of the Medina River (Figure 4.8a), near the river (and basin) origin, display a strongly dendritic (branching) channel pattern. Braided channels (Figure 4.9) are observed occasionally, signifying a high energy flow. The channel is valley-confined, surrounded by limestone bedrock. Erosion-resistant limestone walls inhibit lateral incision, so the stream erodes vertically, cutting down into the riverbed. Hence, slopes are moderately steep (Table 4.4), and drainage density is very high. Little or no sediment is carried in suspension, which is apparent in the aerial photographs by the lack of significant overbank deposits. There is little evidence of human disturbance over the area; several small roads course the region, but no bridges or dams are present. Vegetation over the area is mostly forest, with continuous patches of small trees and brush.

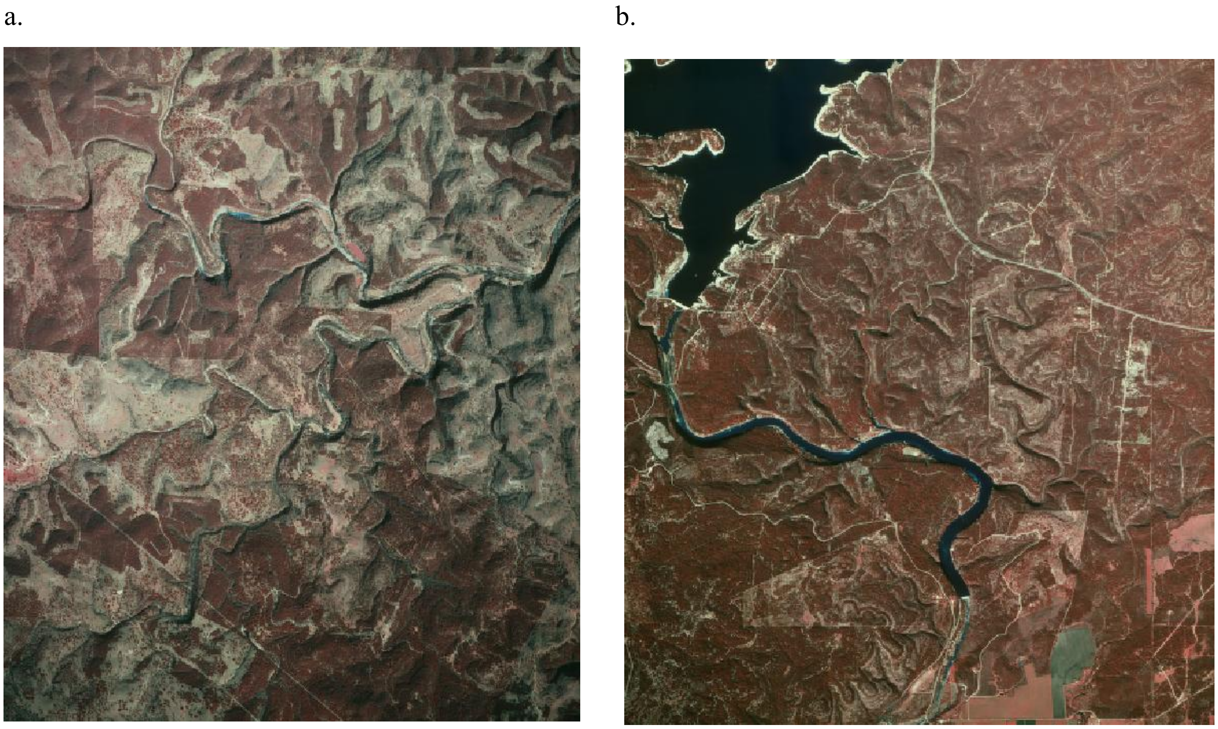

Figure 4.8. Upstream: Aerial photographs from a) Medina River Uplands; b) Medina Lake Outlet. Refer to Chapter 2, Figure 2.2 for stream network configuration.

Figure 4.9. Example of a braided channel pattern, found frequently in the uplands portion the San Antonio River Basin. Braided channels consist of many connected smaller channels separated by small islands, and are common in the hilly areas below headwater zones.

In the Medina Lake Outlet photograph (Figure 4.8b), several kilometers downstream of the uplands, a dendritic pattern is still evident. However, the large Medina Lake Reservoir and its outlet dam have increased the channel energy and thus a single outlet channel becomes the dominant, meandering channel in the photo. Further downstream, one dominant channel is still visible. Many of the streams just south of this area appear structurally controlled, likely due to their coincidence with the Balcones Fault Zone, which crosses the basin below the Medina Reservoir. Streams are valley-confined, topography is moderate, drainage density high, and there is moderate evidence of disturbance in the system. Although the flow appears very low in the photo, scour and erosion of the channel are perceptible south of the dam. Sporadic farms dot the landscape, separated by areas of dense trees and brush.

The downtown area of San Antonio lies in the midland portion of the basin (Figure 4.10a), and is characterized by a clearly urban system. The channel is fairly straight, confined by concrete lining and the surrounding development. Drainage density and topography are both low. Streamflow disturbances are apparent in the numerous dams and navigation structures present. The lack of a floodplain and coincident loss of floodplain vegetation further demonstrate human impacts on the system. Erosion is limited in concrete lined channels. Water flowing through these urban channels is termed ‘hungry’, or devoid of sediment, which increases flow energy and poses greater risk to flood-prone areas. However, unlike previous findings (Knox 1977, Wolman 1967), channel width does not appear to have increased during urbanization of this mid-to-

Figure 4.10. Midstream: Aerial photographs from a) San Antonio River near downtown; b) San Antonio River at its confluence with the Medina River. Refer to Chapter 2, Figure 2.2 for stream network configuration.

Figure 4.11. Meander cutoff and infilled oxbow lake.

upstream region, as the natural channels in the region have greater widths than the developed areas. The reason for this discrepancy is most likely due to the impact of human modification and channelization of the river, regulating flow and preventing migration or enlargement, as well as vegetation encroachment inhibiting lateral migration of the banks. These confined channels are geomorphically unstable due to their inability to migrate freely within the floodplain; river reaches that cannot migrate laterally tend to incise vertically, undercutting the banks and potentially causing bank failure. The majority of the area consists of impervious cover, with some brush and farmland further south (Figure 4.10b).

The non-urban midland regions of the basin demonstrate many distinguishing characteristics, most notably active channel migration, in which the streams are attempting to establish equilibrium. Figure 4.10b represents midland non-urban regions, and consists of a meandering channel with tight meander bends, a narrow meander belt with well-defined floodplain boundaries, moderately low topography, and low drainage density. Most of the area consists of farmland; this region lies just south of the Balcones Fault Zone and includes Blackland Prairie soils and other soils suitable for farming. Many of the meander bends appear near cutoff stage; due to the presence of relic oxbow lakes (standing water formed when a meander loop is cutoff from the main stream; Figure 4.11), it may be inferred that past flood events have carried enough energy to cutoff many of the meander bends; future flooding will likely further straighten the channel.

Downstream areas of the San Antonio River Basin demonstrate a much flatter, almost negligible topography and low drainage density (Figures 4.12a, 4.12b). At this lower region of the basin, the meander belt has widened to nearly twice its upstream width, creating a large floodplain with distinguishing vegetation. The meandering channel has very large bends, none of which appear to be active cutoffs. However, evidence for lateral migration in the recent past is apparent in the many oxbow lakes and abandoned channels. Figure 4.13 demonstrates some of these features. Many of the oxbow lakes currently contain water, implying an active and connected floodplain (although the presence of a high water table may be another explanation, area well logs do not show evidence of such). Strong lateral migration is possible in this region because the rivers lie in erodible alluvium, mainly loamy soils. These soils allow underflow and floodplain storage to occur during high river stage, supporting the dense floodplain vegetation noticeable in the aerial photographs. Thus, the floodplains of the lowlands are well-developed, wide, periodically saturated areas that act as storage and buffer zones, lowering the energy of the passing flood wave. The land around this area is mostly used for agriculture, which increases the sediment load of the river, further decreasing flow energy. The small city of Goliad (pop. 2,041) does not appear to influence the river system, despite its close proximity to the stream.

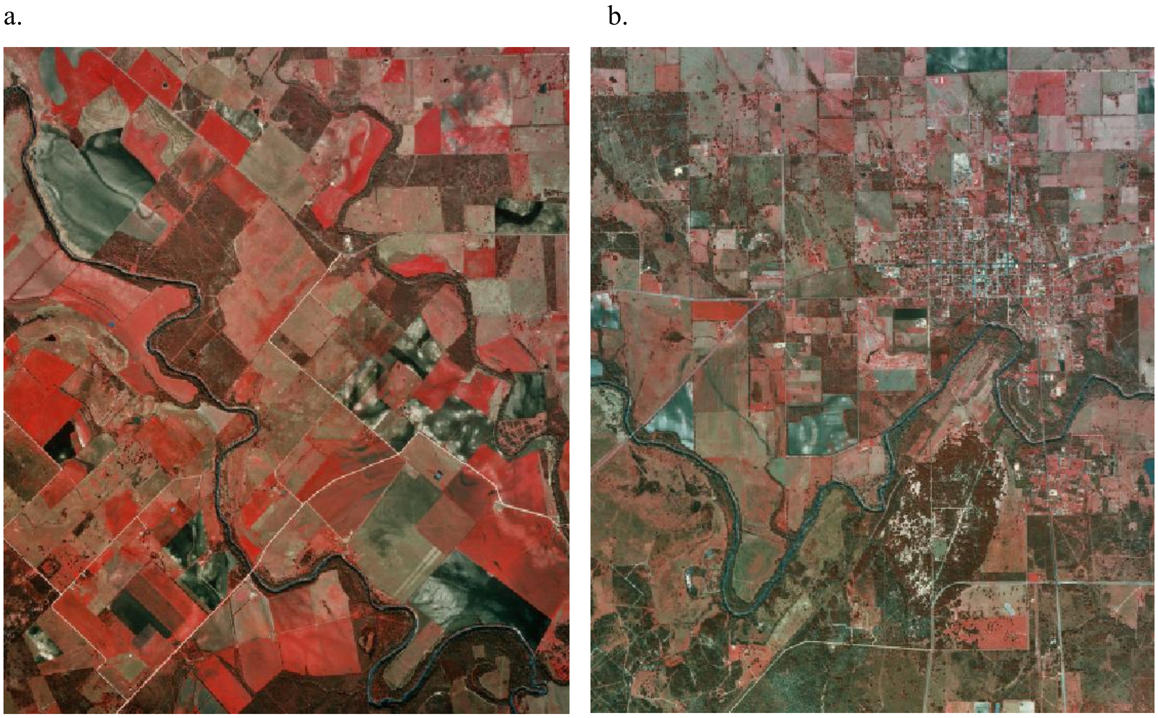

Figure 4.12. Downstream: Aerial photographs from a) San Antonio River and Cibolo Creek, upstream of their confluence; b) San Antonio River at Goliad, upstream of the basin outlet. Refer to Chapter 2, Figure 2.2 for stream network configuration.

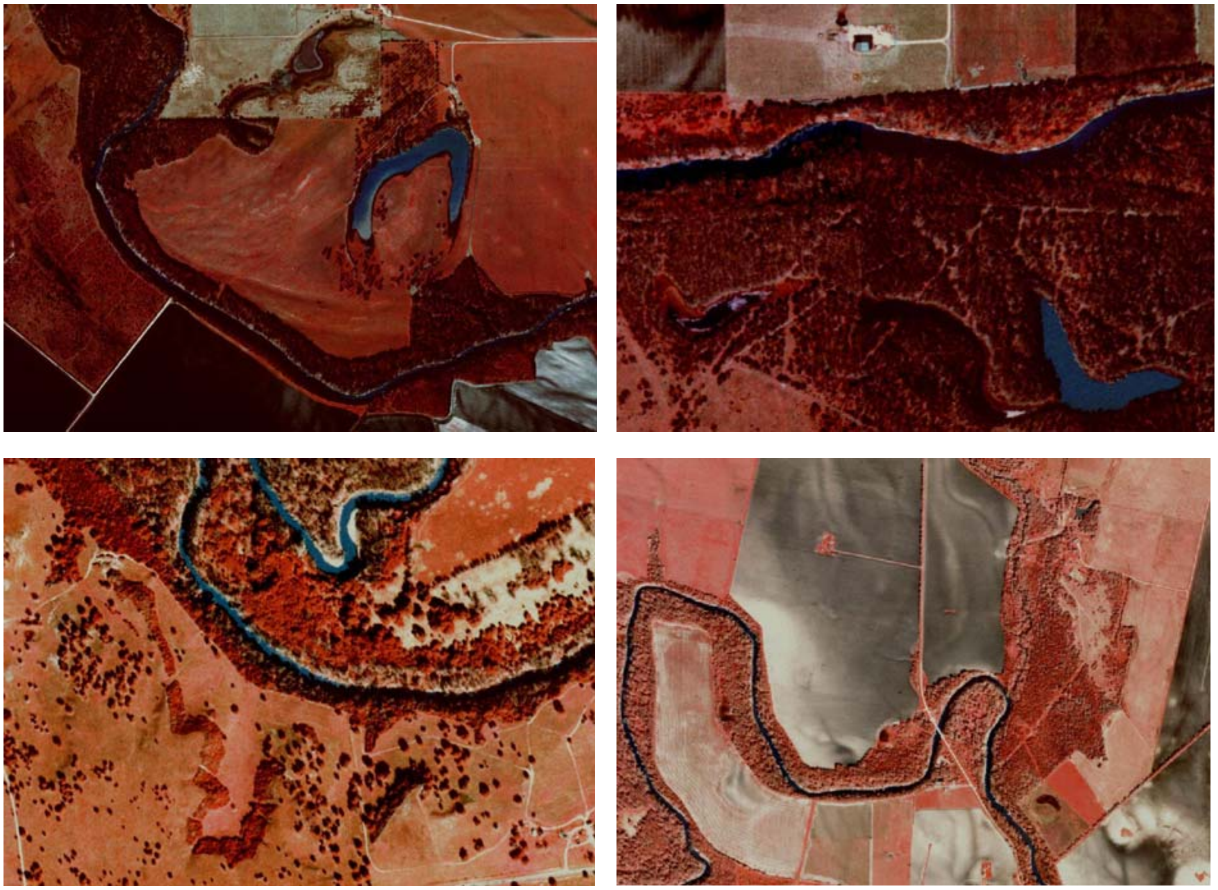

Figure 4.13. Examples of (clockwise from top left): oxbow lakes; oxbow lakes; crevasse; abandoned channel and buried paleochannel; located in the lowermost downstream portion of the basin.

Table 4.4. River measurements taken for the six representative reaches.

River Segment	Bankfull Width (m)	Floodplain Width (m)	Channel Depth (m)	Channel Slope (%)	Floodplain Slope (%)	Sinuosity
Medina R. Uplands	23	79	24	1.0	11.0	1.65
Medina Lake	87	197	23	0.2	6.0	1.74
Downtown San Antonio	43	99	6	0.2	3.3	1.14
SA/Medina R. Confluence	32	478	18	Negligible	5.0	2.21
SA/Cibolo Ck Confluence	41	135	12	Negligible	3.0	1.58
Basin Outlet	54	171	7	1.0	2.0	2.00

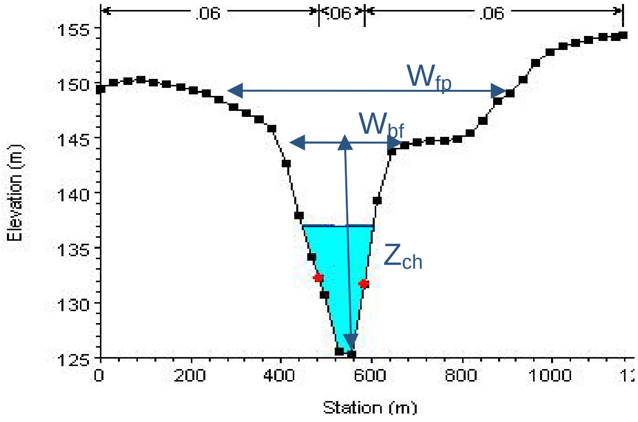

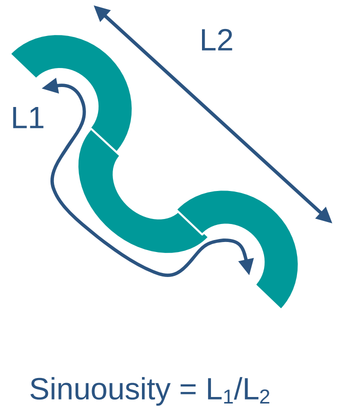

Figure 4.14. Sample river cross-section and plan view, showing the major geomorphic measurements taken for the six representative reaches.

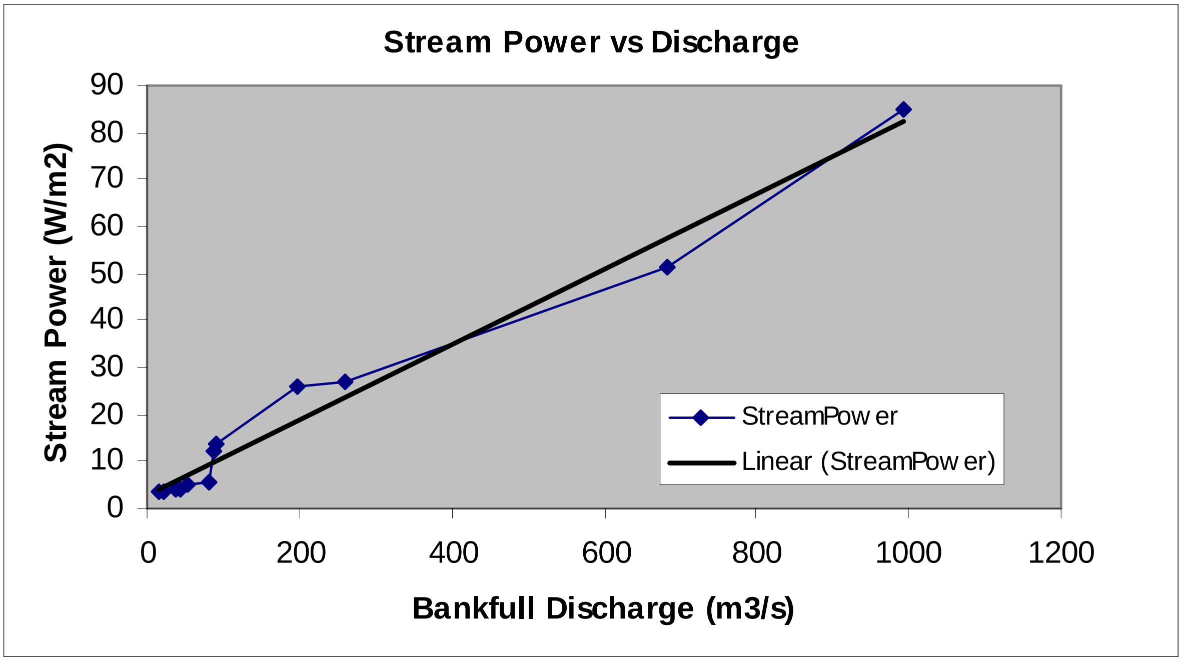

Figure 4.15. Stream power as a function of bankfull discharge across the San Antonio River Basin.

Numerous river measurements were taken to characterize the different regions; measurements taken from the six representative aerial photos are listed in Table 4.4. Figure 4.14 shows the physical representation of these measurements. All of the channels displayed sinuosities above 1.5, low channel gradients, and low width-to-depth ratios, implying a baseflow-dominated system (Larkin and Sharp, 1992). This implies that groundwater flow is perpendicular to the river, and changes direction depending on whether the stream is influent or effluent (see subsequent baseflow discussion).

Figure 4.15 shows the relationship between bankfull discharge and stream power in the San Antonio River Basin. A linear relationship is evident; deviations from the expected linear pattern may be explained by morphology, in a system that is intermediate between erosion and accumulation periods (Graf 1983). Wide, shallow reaches have lower stream power than predicted by the regression line (indicating sedimentation), while narrow, deep reaches have higher stream power than predicted (indicating erosion zones).

Figure 4.16 portrays a typical channel reach in downstream portions of the San Antonio watershed, which demonstrates evidence of sediment accumulation. During depositional equilibrium, flood energy is dissipated across floodplains, depositing sediments overbank instead of transporting them, and stream power in the channel is limited by the relatively small channel size. Opaque waters imply the stream carries a high sediment load and thus travels more slowly, decreasing stream power. Strong floods are so erosive as to deepen the channel, leading to a situation where future events can contain close to 100% of the water within the channel; hence all the water's power is used for sediment transportation, resulting in increased stream power downstream. This erosive situation is typical of upstream portions of the basin, where topography and bedrock control contribute to channel incision (Figure 4.17).

While intuitively stream power should increase in the downstream direction, this situation is often not the case due to the combined influences of channel slope, width, and depth (Equation 1). Lawler (1992) suggested a mid-basin peak in stream power as the typical situation, while Graf (1983) found the largest stream power values to lie in extreme upper and lower watershed areas. Similarly, Jordan and Fonstad (2005) found that cross-sectional stream power was highest in the most upstream and downstream portions of the basin (low and high discharge values, respectively), with much lower stream power values in midbasin regions. They speculate that high power zones reflect more bedrock control on channel width and bed, with greater slopes and shallow depths. Their results are consistent with results for the present study; highest stream power levels were found in the furthest upstream and downstream reaches, with relatively low stream power in the midstream reaches (Figure 4.18). This pattern reflects the influence of steep slopes and highly incised channels in many upstream reaches, and conversely the overriding influence of high streamflow values (as a result of large cross-sectional area) on stream power calculation for the lowermost basin reach.

Figure 4.16. Views of the Lower Cibolo Creek, near its confluence with the San Antonio River. This stream and other downstream reaches appear to be in a depositional phase, with evidence of fine-grained sediment aggradation along the banks.

Figure 4.17. View of upstream river reaches showing evidence of bank erosion and bedrock incision: Cibolo Creek (top photo) and Medina River (bottom photo). Upstream reaches are characterized by limestone riverbeds and significant bank instability.

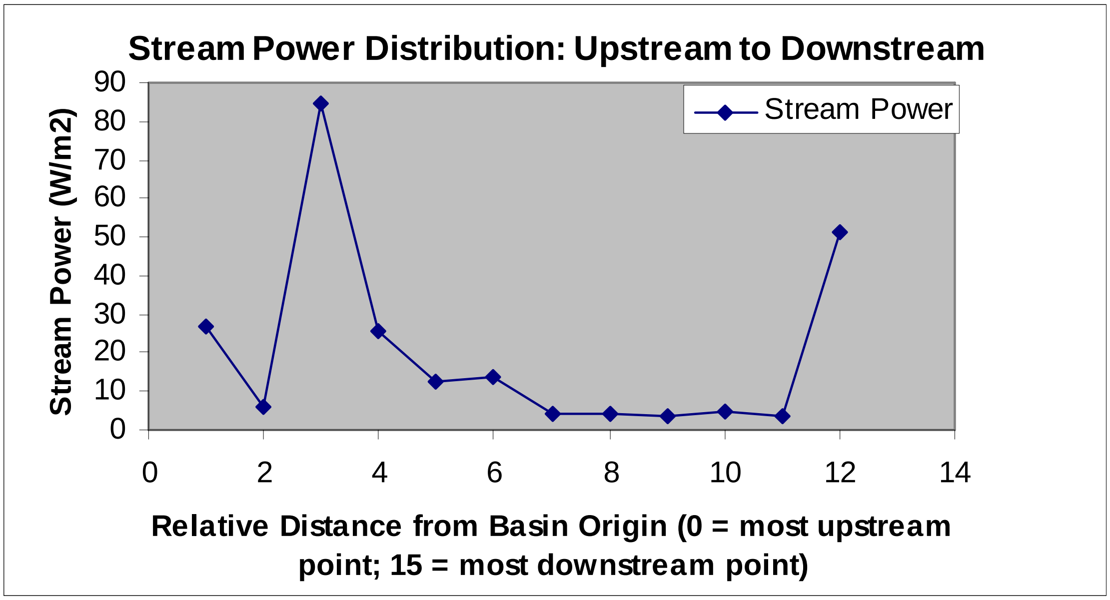

Figure 4.18. Stream power as a function of relative distance downstream (uppermost to lowermost reaches).

Caution must be used in regard to stream power measurements because little is known about the spatial and temporal variation in stream power across river networks. This variation must be explained in terms of the relationship between channel form and process, but this relationship is continuously changing, and thus hard to define. In addition, although the amount of sediment supplied to the river will limit the amount of sediment available for transport, there is no widely used method for determining temporal changes in sediment supply during stream power analysis.

Hydrology

The hydrology of the basin is highly variable. Figure 4.19 shows hydrographs for a four-year period (2000-2004) from each of the three general basin regions: upstream, midstream, and downstream. Baseflow, which can be approximated by a line connecting the hydrograph troughs, is lowest in the uplands regions (Figure 4.19a), where the stream system is mostly fed by direct precipitation; the lack of a strong groundwater influx keeps baseflow levels low between storm events.

The gauge in downtown San Antonio (Figure 4.19b) shows a moderate baseflow and a very flashy hydrograph response to rainfall (or lack of rainfall). Flow is much more variable here than in the uplands, with a high sensitivity to changes in precipitation evident in the large daily and monthly discharge variations. Much of this baseflow, especially in the San Antonio River, is supplied by well overflow and leakage from wastewater pipes; aquifer pumpage has lowered water table levels to such an extent that springflow rarely occurs from springs along the river as it flows through downtown. The baseflow for downstream basin areas is significantly higher than elsewhere in the basin (Figure 4.19c). This may be due to several factors. The slopes are flatter and the floodplains wider with large meanders, allowing significant time and space for storage and attenuation of water. Water infiltrated in the floodplains of the downstream region will flow into the river during times of little rainfall; as the water table falls, the local hydraulic gradient reverses direction and the river changes from an effluent to an influent stream. Irrigation ditches may also contribute their excess soil moisture as baseflow to the river, and the water table is much closer to the surface, as much as an order of magnitude or more compared to uplands areas (TWDB well logs; source: USGS, 2006).

Peak streamflow levels during storm events can be indicative of fluvial disturbance by looking at the flashiness of the hydrograph response. Urban areas that have lost natural floodplain storage tend to be flashiest, as demonstrated by the San Antonio gauging station during the July 2002 storm (Figure 4.20b). Downstream areas of the basin (Figure 4.20c) demonstrate a smoother hydrograph associated with floodplains in their natural state: a gradual flow increase to a large peak with a wide base (duration), and a slow regression back to baseflow.

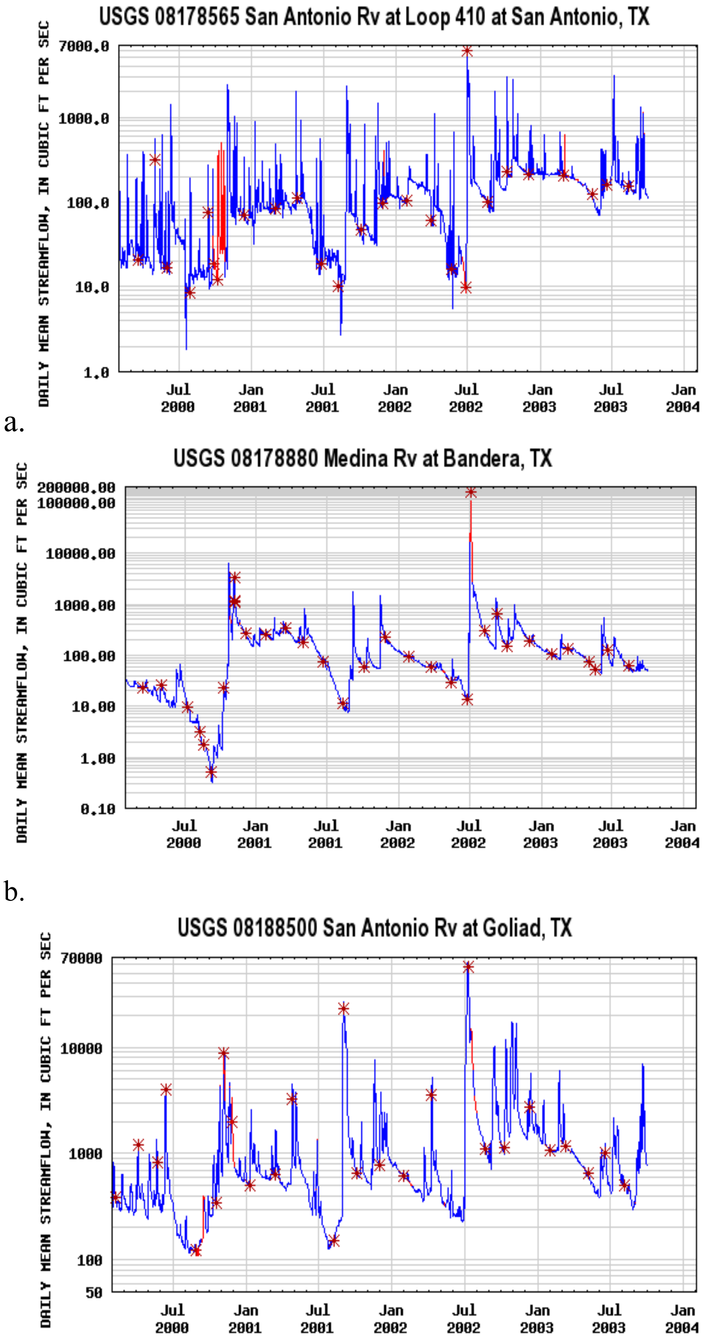

c.

Figure 4.19. Hydrographs for: a) upstream; b) midstream; and c) downstream basin areas (Source: USGS).

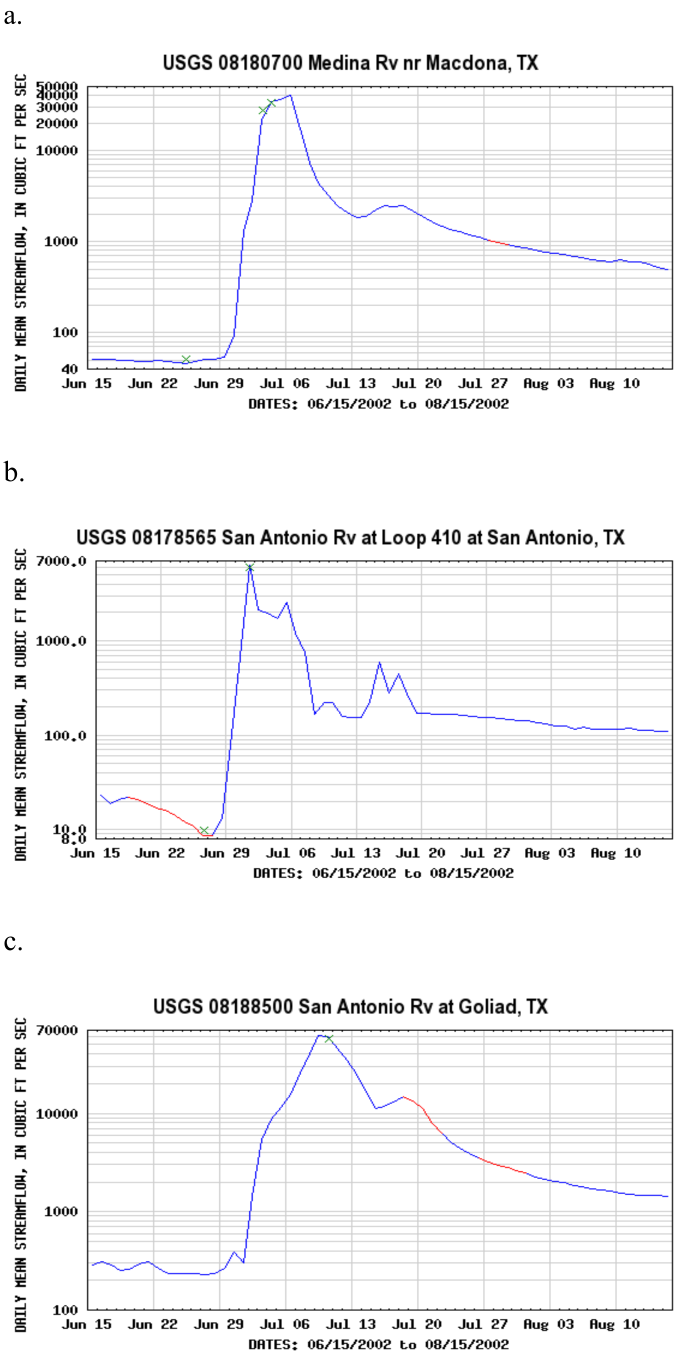

Figure 4.20. Streamflow peaks for the July 2002 storm over Central Texas for: a) upstream; b) midstream; and c) downstream areas (Source: USGS).

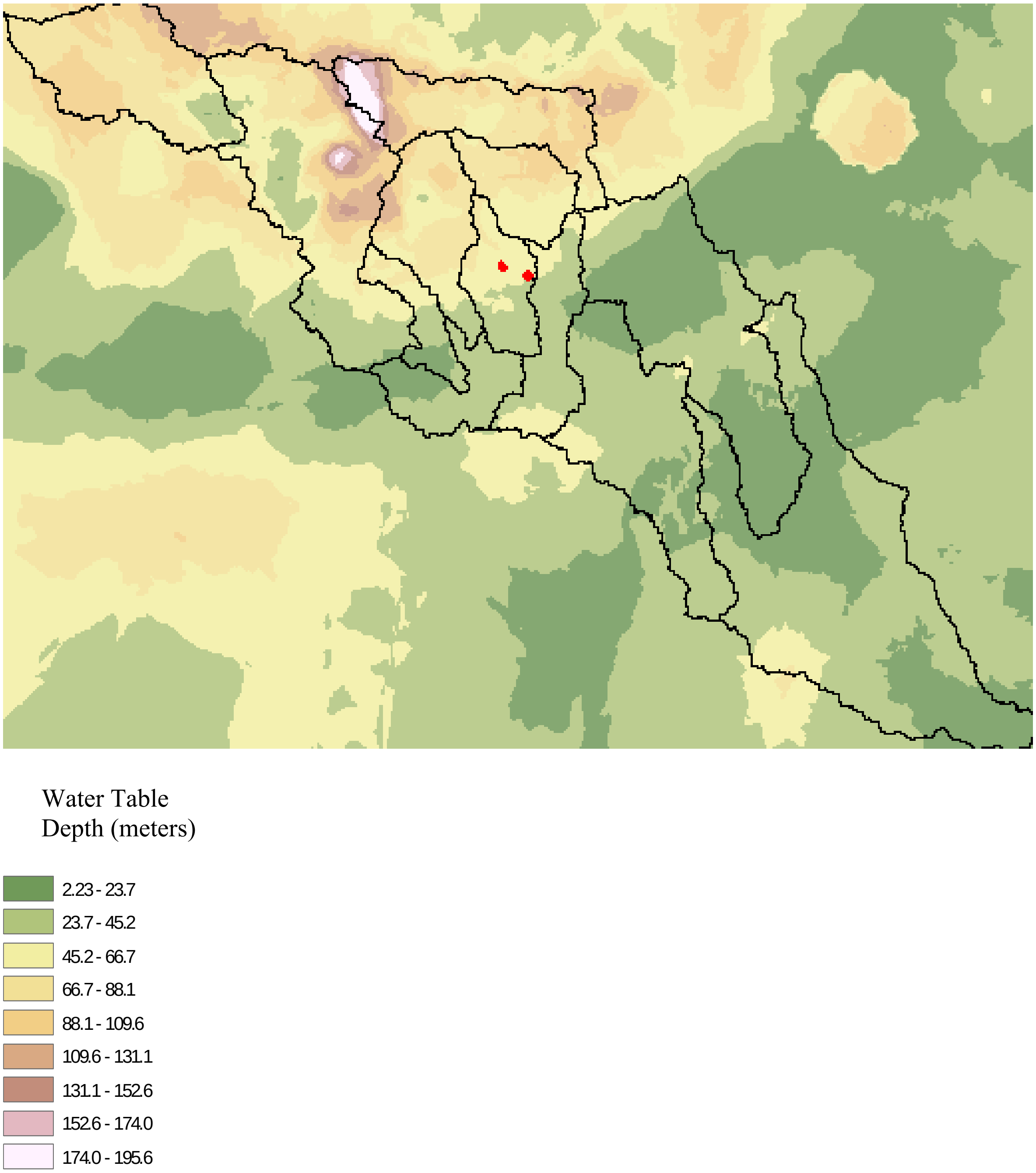

Figure 4.21. Water table depth (meters) across the study watershed.

Figure 4.21 is a map of water table depth across the basin, created by digitizing approximately 4,000 driller logs from the Texas Water Development Board. All depths were measured on or after the year 2000, so the effect of land use change is negligible. A general trend of deep water table values in the upbasin areas and relatively shallow water table values in the lower basin areas is apparent. In addition, the abrupt change in depth across the midbasin area coincides with the southern boundary of the aquifer recharge zone. Streams located north of this boundary mostly lose surface water to the aquifer, and correspondingly they were found to have scarce floodplain storage and low baseflow values during periods of no rainfall.

Flow duration curves (FDCs) plot streamflow values from highest to lowest on the y-axis against the percent exceedance on the x-axis, and can be used to determine return intervals for various discharge levels. FDCs were plotted from USGS peak streamflow data for twelve gaging stations (corresponding to subbasin outlets in the GIS model), in order to compare frequency patterns and derive bankfull discharge for each. Bankfull discharge generally has a return period of 1-2 years, as stated previously, or approximately a 50-67% chance of being exceeded in any given year. FDC results are shown in Figure 4.22.

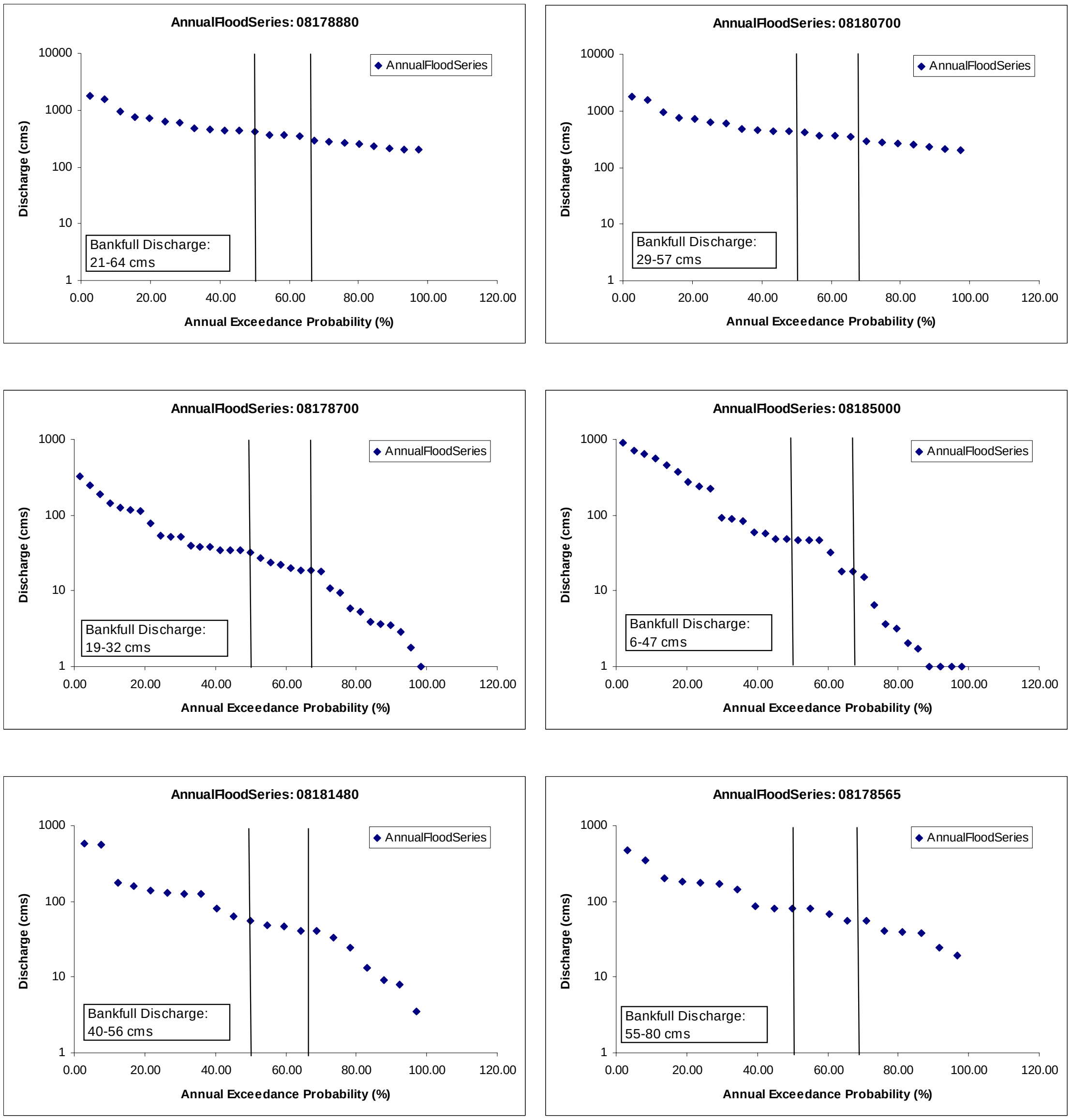

Figure 4.22. Flow duration curves for twelve gages across the San Antonio watershed. Upstream to downstream gages are shown left to right, top to bottom. The two solid lines mark the 50 and 67% flow exceedence values, used to estimate bankfull discharge.

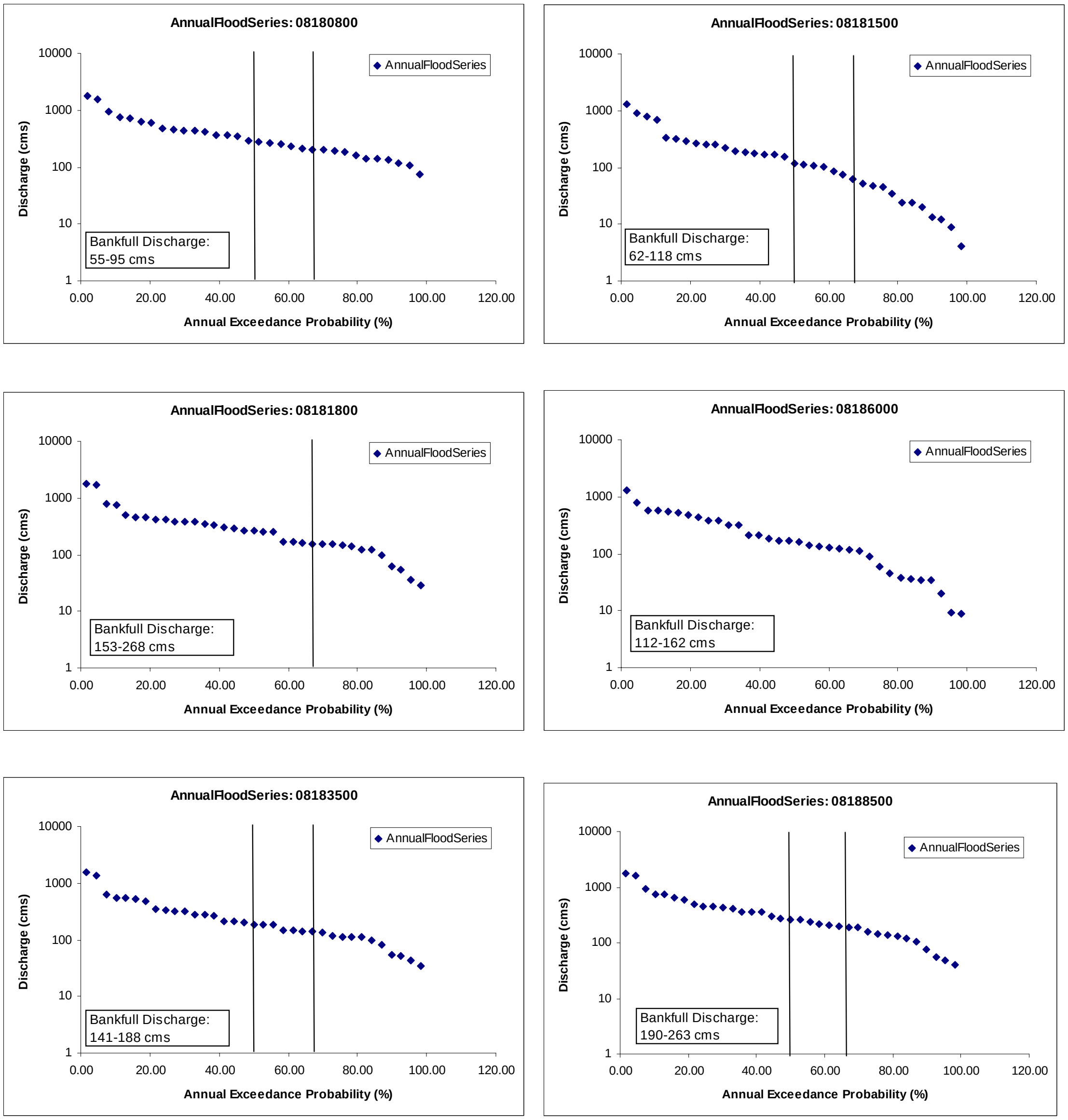

Figure 4.22 (continued). Flow duration curves for twelve gages across the San Antonio watershed. Upstream to downstream gages are shown left to right, top to bottom. The two solid lines mark the 50 and 67% flow exceedence values, used to estimate bankfull discharge.

Table 4.5. Flow duration curve results for 12 USGS gages across the San Antonio River Basin. Return period for bankfull flow is compared to the literature standard 1.5-yr return period.

Gage	Location	FDC 1.5-yr flow (cms)	Q_{bf} (cms), based on channel geometry	Q_{bf} return period from FDCs
08178880	Upstream	21	91	2.7 yr
08180700	Upstream	29	89	3.7 yr
08178700	Upstream	19	23	1.7 yr
08185000	Upstream	6	81	2.9 yr
08181480	Midstream	40	15	1.2 yr
08178565	Midstream	55	38	1.2 yr
08180800	Midstream	55	993	25.0 yr
08181500	Midstream	62	681	9.1 yr
08181800	Midstream	153	198	1.8 yr
08186000	Downstream	112	45	1.3 yr
08183500	Downstream	141	53	1.1 yr
08188500	Downstream	190	261	2.0 yr

MODEL IMPROVEMENTS BASED ON GEOMORPHOLOGIC FINDINGS

The purpose of the present investigation of the geomorphologic and hydrologic variability of the San Antonio River Basin was twofold. The major goal of the study was to obtain a broader understanding of basin hydrologic response and its connections to geomorphology. A secondary goal was to use insight gained from this study to recommend improvements in the hydrologic model's representation of physical reality. To this end several modifications were employed, including an improved curve number grid and soil coverage.

Many methods exist for representing infiltration in hydrologic models. The curve number (CN; see Chapter 2) method was utilized in this study. This empirical method is based on studies from numerous gauged basins; it is moderately complex but highly applicable in flood-related hydrologic studies. As described in Chapter 2, initial model development used STATSGO soils data and a 30 meter resolution land cover dataset to derive CN. During calibration it was discovered that the model was sensitive to changes in CN. CN is derived largely from soil properties such as permeability and drainage capacity; the coarse scale of the STATSGO dataset may induce large errors in CN that propagate to errors in model output. In order to improve model performance, a much more detailed dataset, the Soil Survey Geographic (SSURGO) database for Texas was studied. SSURGO was created for local scale investigations and is most suitable for individual landowners needing information about the immediate area; more information can be obtained from the detailed county-wide soil surveys from which SSURGO data are derived (Batte 1984, Dittemore and Hensell 1981, Dittmar 1977, Dittmar and Stevens

1980, Hensell 1977, Miller 1978, Molina 2000, Ramsey and Bade 1977, Soil Survey Staff 2005, Taylor 1977, Taylor, Hailey, and Richmond 1966, USDA 1972, USDA 1986). Incorporation of SSURGO data in ArcGIS is computationally intensive but offers a significant improvement upon the resolution of soils data, including 1096 map unit types for the basin, compared to 34 map unit types in the STATSGO dataset (Figure 4.23).

Replacement of STATSGO data coverage with the SSURGO dataset resulted in little difference between model runs with the two datasets. In fact, the finer-resolution SSURGO data tended to overestimate observed streamflow more than the coarse STATSGO dataset, implying that the choice of infiltration method (i.e., CN) may be the limiting factor to model improvement, rather than the resolution of contributing datasets.

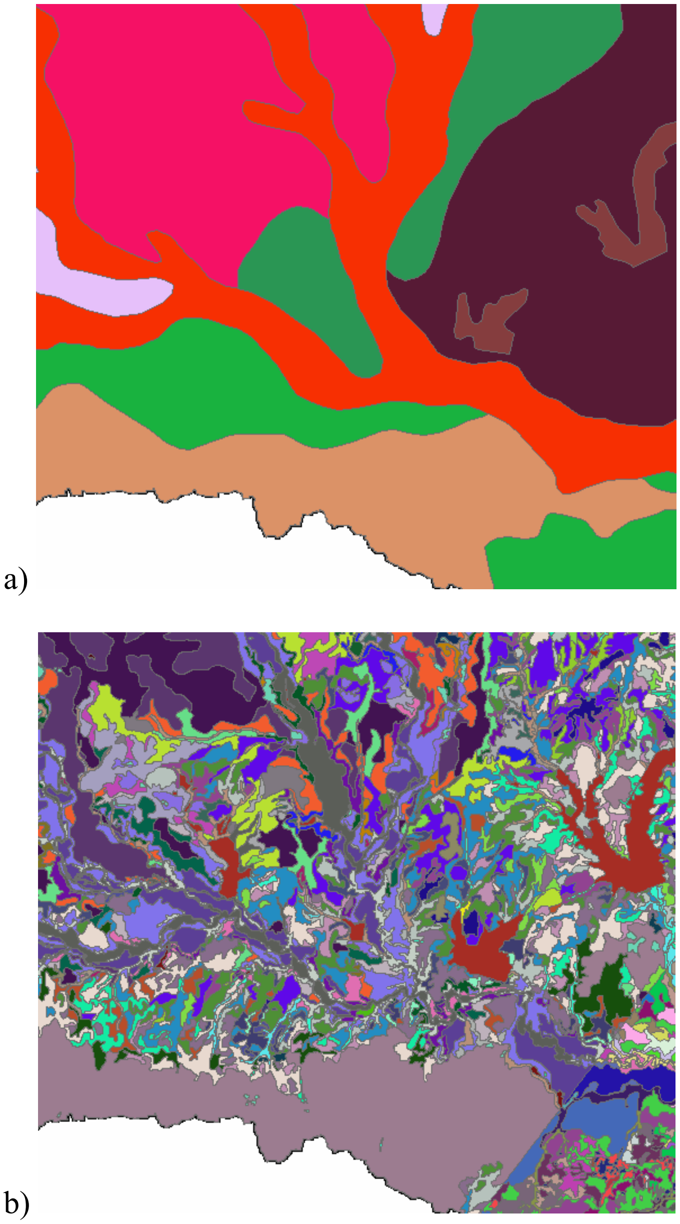

Figure 4.23. Soil data at the confluence of the Medina/San Antonio Rivers, for a) STATSGO and b) SSURGO datasets. Each color represents a separate soil type in the dataset.

Preliminary model results overestimated streamflow in almost all subbasins, implying that the model formulation allowed too much runoff and too little infiltration and storage. To achieve a more realistic representation of infiltration capacity across the basin, cave features were incorporated into the model. Cave locations, including those underneath losing streams, were plotted and georeferenced into ArcGIS (Figure 4.3). Locations of caves were based on maps and literature from the Texas Speleological Society (Elliot 1985, Elliot and Veni 1994, Reddell 1964, Reddell 1967, Veni 1988). A formula was developed to adjust the curve number based on the number of cave features in each grid cell:

$$CN_{new} = CN_{old} * (1 - 0.07x) \qquad (3)$$

where x = number of caves located in the particular grid cell

Model results demonstrated lower streamflow in cave-heavy areas following the CN modification (Figure 4.24).

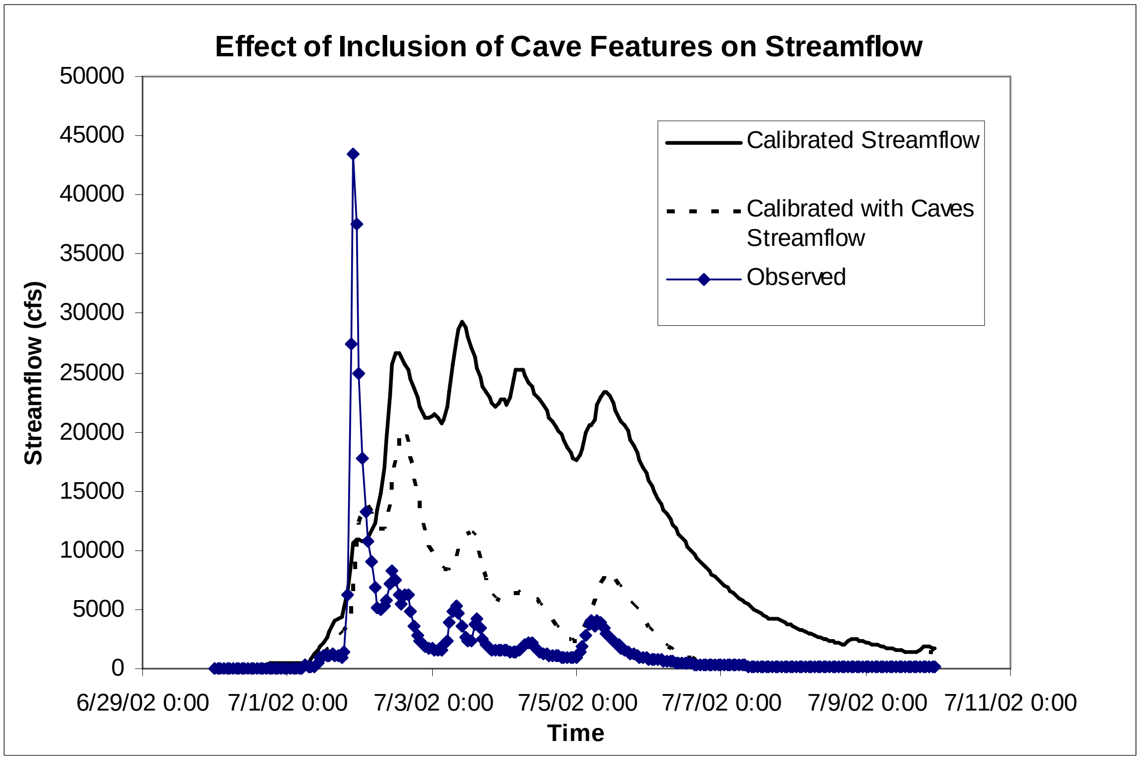

Figure 4.24. Hydrograph output from model comparing streamflow with and without inclusion of cave features. Inclusion of caves tends to lower overall streamflow, especially by lowering many of the sharp flow peaks.

SUMMARY: IMPLICATIONS FOR HYDROLOGICAL MODELING EFFORTS OVER THE SAN ANTONIO RIVER WATERSHED

This research has demonstrated the vast heterogeneity of the San Antonio River Basin in terms of geology, climate, land use, geomorphology, and hydrology. Using ArcGIS analysis of spatial datasets, aerial photographs, and previous research, the watershed has been subdivided into three areas with similar characteristics. The results of this study provide a more comprehensive understanding of the watershed features, and underscore the importance of accounting for geomorphic variability across large river basins such as the San Antonio Basin.

Upstream areas of the basin can be characterized by dendritic, braided, bedrock controlled streams, low sediment load, and vertical incision of the channel. As a result, the river system is topographically steep and carries a high energy flow with little baseflow between rain events. Midstream areas in urban settings are controlled by flow structures, lack a floodplain and floodplain vegetation, and carry very little sediment. Hence, the channels are straight and carry a high energy, flashy discharge. Midstream areas in non-urban settings are characterized by tight meanders and evidence of recent avulsions, showing that the channel is actively migrating and attempting to re-establish equilibrium. Downstream areas of the basin have a high sediment load, prominent floodplains and riparian vegetation, and high sinuosity. These characteristics result in a stable system with a low energy flow that has the capacity to carry large floods, as well as high baseflow levels from extensive floodplain storage.

Much of the geomorphic knowledge gained from this investigation could be used to improve the rainfall-runoff modeling capability of the flood model. Soil texture resolution in the STATSGO database is too coarse for modeling at the floodplain and river reach scale; a finer resolution dataset such as SSURGO is recommended. However, model runs with the SSURGO data demonstrated that the infiltration model limits the accuracy attainable for flood modeling; in other words, the accuracy of the derived curve numbers and methodology for estimating CN must be improved concurrently with improved soil texture datasets. Major features of the karstic landscape must be included in the hydrological model, such as cave features and springs. The inclusion of caves substantially increased streamflow accuracy over cavernous basins. The two large springs of the basin, San Antonio Springs and San Pedro Springs, are frequently dry and thus were considered to be influent for modeling purposes; however, it would be useful to model the temporal variation in springflow within the hydrological model to capture any effluent spring flow that may contribute to basin discharge.

The three regions characterized in this study must each be considered separately from one another and modeled according to the unique stream and floodplain features of each. Roughly, the three areas can be categorized as 1) incised limestone streambeds with steep floodplain slopes (upstream); 2) urbanized reaches lacking a functioning floodplain (midstream); and 3) natural streams flowing in alluvium channels with wide floodplains and meander belts (downstream). One important implication of the geomorphic differences between these regions is the soil moisture characteristics of each. In the bedrock controlled upper reaches, field evidence showing lack of riparian vegetation and mapped deep water table levels (Figure 4.21) signify hydrologic drought over the area. Conversely, the lowermost “natural” stream reaches have wide alluvium floodplains that encourage soil moisture storage and underflow. The antecedent moisture conditions (soil moisture) prior to the forecasted flood event are likely very different here than in other regions of the basin. Simple field work and analysis of water table levels can aid in the delineation of these regions. For example, the presence and density of oxbow lakes within the meander belt may give an idea of the volume of water storage available to the stream. The hydrological model should contain a methodology for including soil moisture conditions that takes into account the variation of available moisture across the basin. In midstream urban areas, the lack of any significant floodplain contributes to the flashy hydrologic response, made further complex by man-made drainage and control systems. Since a regional scale model cannot capture the complexity of the developed river system, it may be useful to model this portion of the watershed using an artificial neural network model (ANN), which can learn the response of the system without requiring the model to include specific details of the drainage system.

The San Antonio River Basin is not entirely in a depositional or erosional equilibrium; some regions appear to be undergoing erosion, deposition, or in transition between the two stages. Stream power measurements may be useful for river routing in the hydrological model, because they aid in understanding the level of channel bedrock control, sediment load, and bank deposition and erosion features. By correlating stream power with roughness coefficients, they also may be used as a supplement to Manning’s n values derived from coarse-scale land cover datasets.

This study demonstrates the importance of characterizing the heterogeneity of geomorphology and hydrology across a large river basin for regional scale flood modeling. The characteristics of the land surface, river network, and hydrologic behavior are inextricably linked; by addressing this relationship between form and process at a basin scale, hydrological modeling and resulting flood forecasts can be significantly improved.

Chapter 5: Conclusions

This research explored the potential for flood modeling over a large, heterogeneous watershed in central Texas. A case study of an extreme storm event during the summer of 2002 provided an example of a typical convective storm produced by excessively strong, moisture-laden Gulf winds, which combined with uplift-inducing conditions in upper atmospheric levels to produce persistent, intense rainfall over the region. Costly damages to homes and infrastructure, including the densely populated city of San Antonio, resulted from the flood.

Devastating flood events are not an uncommon occurrence in central Texas, but current flood prediction efforts are frequently local scale, with insufficient lead time for disaster mitigation. This study addressed the problem of flood forecasting from a regional scale over the entire San Antonio River watershed, and investigated the possibility of driving hydrological models with numerical weather model rainfall forecasts instead of real-time radar or gage datasets. Modeled hydrographs and flood inundation areas matched fairly well with observations. The introduction of WRF rainfall forecast grids, with a lead-time of 48 hours, produced streamflow results similar to those modeled with NEXRAD radar data. The expansion of the model to a regional scale necessitated an in-depth study of the heterogeneity of geomorphologic and hydrologic features of the channel and floodplain, features that are often considered homogeneous for small watersheds. Results from the investigation demonstrated that the

San Antonio River Basin can be divided into three major hydrogeomorphic areas, with further subdivision suggested for improved accuracy.

Appendix

Normal Manning's N Values for different channel types (modified from HEC, 2002)

Channel Type	Manning's N
A. Natural Channels	
1. Main Channels	
a. Clean, straight, full, no rifts or deep pools	0.030
b. Same as above, but more stones and weeds	0.035
c. Clean, winding, some pools and shoals	0.040
d. Same as above, but some weeds and stones	0.045
e. Same as above, lower stages, more ineffective slopes and sections	0.048
f. Same as "d" but more stones	0.050
g. Sluggish reaches, weedy, deep pools	0.070
h. Very weedy reaches, deep pools, or floodways with heavy stands of timber and brush	0.100
2. Floodplains	
a. Pasture no brush	
Short grass	0.030
High grass	0.035
b. Cultivated areas	
No crop	0.030
Mature row crops	0.035
Mature field crops	0.040
c. Brush	
Scattered brush, heavy weeds	0.050
Light brush and trees, in winter	0.050
Light brush and trees, in summer	0.060
Medium to dense brush, in winter	0.070
Medium to dense brush, in summer	0.100
d. Trees	
Cleared land with tree stumps, no sprouts	0.040
Same as above, but heavy sprouts	0.060
Heavy stand of timber, little undergrowth, flow below branches	0.100
Same as above, but with flow into branches	0.120
Dense willows, summer, straight	0.150
3. Mountain Streams, steep banks, no vegetation in channel	
a. Bottom: gravels, cobbles, a few boulders	0.040
b. Bottom: cobbles with large boulders	0.050
B. Lined or Built-Up Channels	
1. Concrete	

a. Trowel finish	0.013
b. Float finish	0.015
c. Finished, with gravel bottom	0.017
d. Unfinished	0.017
e. Gunite, good section	0.019
f. Gunite, wavy section	0.022
g. On good excavated rock	0.020
h. On irregular excavated rock	0.027
2. Concrete bottom float finished with sides of:	
a. Dressed stone in mortar	0.017
b. Random stone in mortar	0.020
c. Cement rubble masonry, plastered	0.020
d. Cement rubble masonry	0.025
e. Dry rubble on riprap	0.030
3. Gravel bottom with sides of:	
a. Formed concrete	0.020
Random stone in mortar	0.023
c. Dry rubble or riprap	0.033
4. Brick	
a. Glazed	0.013
b. In cement mortar	0.015
5. Metal	
a. Smooth steel surfaces	0.012
b. Corrugated metal	0.025
6. Asphalt	
a. Smooth	0.013
b. Rough	0.016
7. Vegetal lining	0.030-500
C. Excavated or Dredged Channels	
1. Earth, straight and uniform	
a. Clean, recently completed	0.018
b. Clean, after weathering	0.022
c. Gravel, uniform section, clean	0.025
d. With short grass, few weeds	0.027
2. Earth, winding and sluggish	
a. No vegetation	0.025
b. Grass, some weeds	0.030
c. Dense weeds or aquatic plants in deep channels	0.035
d. Earth bottom and rubble side	0.030
e. Stony bottom and weedy banks	0.035
f. Cobble bottom and clean sides	0.040
3. Dragline-excavated or dredged	
a. No vegetation	0.028
b. Light brush on banks	0.050

4. Rock cuts	
a. Smooth and uniform	0.035
b. Jagged and irregular	0.040
5. Channels not maintained, weeds and brush	
a. Clean bottom, brush on sides	0.050
b. Same as above, highest stage of flow	0.070
c. Dense weeds, high as flow depth	0.080
d. Dense brush, high stage	0.100

BIBLIOGRAPHY

Abbott, P.L. (1975). On the hydrology of the Edwards Limestone, south-central Texas. *Journal of Hydrology* 24, 251-269.

Abbott, P.L., and Woodruff, C.M., Jr. (1986). The Balcones Escarpment: Geology, Hydrology, Ecology and Social Development in Central Texas. *Geological Society of America*, San Antonio, Texas.

Acker, S.A., Gregory, S.V., Lienkaemper, G., McKee, W.A., Swanson, F.J., and Miller, S.D. (2003). Composition, complexity, and tree mortality in riparian forests in the central Western Cascades of Oregon. *Forest Ecology and Management* 173(103), 293-308.

Ahrens, C.D. (2005). Essentials of Meteorology: An Invitation to the Atmosphere. 4th Ed., Brooks/Cole, Belmont, CA, 472 pp.

Ahrens, S.R. and Maidment, D.R. (1999). Flood forecasting for the Buffalo Bayou using CRWR-PrePro and HEC-HMS, *CRWR Report 99-6*. Austin, Texas: Center for Research in Water Resources.

Anderson, M.L., Chen, Z.-Q., Kavvas, M.L., Feldman, A. (2002). Coupling HEC-HMS with atmospheric models for prediction of watershed runoff. *Journal of Hydrologic Engineering, 7* (4), 312-318.

Arnow, T. (1959). Ground-water geology of Bexar County, Texas. *Texas Board of Water Engineers Bulletin* 5911, 62p.

Bagnold, R.A. (1966). An approach to the sediment transport problem from general physics. *U.S. Geological Survey Professional Paper* 422-J. Washington: U.S. Government Printing Office.

Baik, J.-J., M. DeMaria, and S. Raman (1991). Tropical cyclone simulations with the Betts convective adjustment scheme. Part III: Comparisons with the Kuo convective parameterization. *Mon. Wea. Rev.*, 119, 2889-2899.

Barker, J.R., Ringold, P.L., and Bollman, M. (2002). Patterns of tree dominance in coniferous riparian forests. *Forest Ecology and Management*, 166(1-3), 311-329.

Bates, P.D. (2004). Remote sensing and flood inundation modeling. *Hydrological Processes*, 18, 2593-2597.

Batte, C.D. (1984). Soil Survey of Comal and Hays Counties, Texas. *U.S. Department of Agriculture*, Natural Resources Conservation Service, 136pp.

Becker, A., Grunewald, U. (2003). Flood risk in Central Europe. *Science, 300* (5622), 1099.

Bedient, P.B., Holder, A., Benavides, J.A., Vieux, B.E. (2003). Radar-based flood warning system applied to Tropical Storm Allison. *Journal of Hydrologic Engineering, 8* (6), 308-318.

Bélair, S., and J. Mailhot (2001). Impact of horizontal resolution on the numerical simulation of a midlatitude squall line: implicit versus explicit condensation. *Mon. Wea. Rev.*, 129, 2362-2376.

Beven, K. (2002). Towards an alternative blueprint for a physically based digitally simulated hydrologic response modeling system. *Hydrological Processes, 16*

(2),189-206.

Bonner, W.D. (1968). Climatology of the low-level jet. *Mon. Wea. Rev.*, 96, 833-850.

Borga, M. (2002). Accuracy of radar rainfall estimates for streamflow simulation. *Journal of Hydrology*, 267, 26-39.

Bryant, R.G., and Gilvear, D.J. (1999). Quantifying geomorphic and riparian land cover changes either side of a large flood event using airborne remote sensing: River Tay, Scotland. *Geomorphology* 29, 307-321.

Bryant, R.G., Rainey, M.P. (2002). Investigation of flood inundation on playas within the Zone of Chotts, using a time-series of AVHRR. *Remote Sensing of Environment*, 82 (2-3), 360-375.

Chen, X., and Chen, X. (2003). Stream water infiltration, bank storage, and storage zone changes due to stream-stage fluctuations. *Journal of Hydrology* 280, p246-264.

Chow, V.T. (1964). Handbook of Applied Hydrology. New York: McGraw-Hill.

Chow, V.T., Maidment, D.R., Mays, L.W. (1988). Applied Hydrology, McGraw-Hill.

Clark, C.O. (1945). Storage and the unit hydrograph. *Transactions: American Society of Civil Engineers,* 110, 1419-1488.

Colby, J.D., Mulcahy, K.A., and Wang, Y. (2000). Modeling flooding extent from Hurricane Floyd in the coastal plains of North Carolina. *Environmental Hazards* 2, 157-168.

Dery, S.J., E.F. Wood, and C. Kerr (2005). Comparing NARR, ERA-40, and observed Hudson Bay river discharge. *Proc. North American Regional Reanalysis Workshop*, San Diego, CA, American Meteorological Society.

Descroix, L., Viramontes, D., Vauclin, M, Gonzales Barrios, J.L., Esteves, M. (2001). Influence of soil surface features and vegetation on runoff and erosion in the Western Sierra Madre (Durango, Northwest Mexico). *Catena* 43, 115-135.

Detenbeck, N.E., Brady, V.J., Taylor, D.L., Snarski, V.M., and Batterman, S.L. (2005). Relationship of stream flow regime in the western Lake Superior basin to watershed type characteristics. *Journal of Hydrology*, In Press.

Dingman, S.L. (2002). *Physical Hydrology* (2nd Edition). New Jersey: Prentice-Hall, Inc.

Dittemore, Jr.,W.H., and Hensell, J.L. (1981). Soil Survey of Kendall County, Texas. *U.S. Department of Agriculture*, Natural Resources Conservation Service, 87pp.

Dittmar, G.W. (1977). Soil Survey of Medina County, Texas. *U.S. Department of Agriculture*, Natural Resources Conservation Service, 92pp.

Dittmar, G.W., and Stevens, J.W. (1980). Soil Survey of Atascosa County, Texas. *U.S. Department of Agriculture*, Natural Resources Conservation Service, 131pp.

Dolcine, L., Andrieu, H., Sempre-Torres, D., Creutin, D. (2001). Flash flood forecasting with coupled precipitation model in mountainous Mediterranean basin. *Journal of Hydrologic Engineering, 6* (1), 1-10.

Dutta, D., Herath, S., Musiake, K. (2000). Flood inundation simulation in a river basin using a physically based distributed hydrologic model. *Hydrological Processes*, 14 (3), 497-519.

Ekwoanya, M.A., and Ojanuga, A.G. (2002). Productivity assessment of upland and floodplain soils at Makurdi, Nigeria. *Geoderma* 108, 19-29.

Elliot, W.R. (1985). A Field Guide to the Caves of Kendall County. 143pp.

Elliot, W.R., and Veni, G. (1994). The Caves and Karst of Texas. *NSS Convention Guide*, National Speleological Society, 342pp.

Emanuel, K.A., and M. Zivkovic-Rothman (1999). Development and evaluation of a convection scheme for use in climate models. *J. Atmos. Sci.,* 56, 1766-1782.

Ferrier, B.S. (1994). A double-moment multiple-phase four-class bulk ice scheme. Part I: description. *J. Atmos. Sci.,* 51, 249-280.

Freeze, R.A., Harlan, R.L. (1969). Blue-print for a physically-based digitally simulated hydrologic response model, *Journal of Hydrology*, 9, 237-258.

Fritsch, J.M., and R.E. Carbone (2004). Improving quantitative precipitation forecasts in the warm season. *Bull. Amer. Meteor. Soc.,* 85, 955-965.

Gallus, W.A., and M. Segal (2001). Impact of improved initialization of mesoscale features on convective system rainfall in the 10-km Eta simulations. *Wea. Forecasting,* 16, 680-696.

Garen, D.C. (1998). ENSO indicators and long-lead climate outlooks: Usage in seasonal streamflow volume forecasting in the western United States. *Eos Supplement*, v. 79, American Geophysical Union Fall Meeting, F325.

Garnier, J., Billen, G., Hannon, E., Fonbonne, S., Videnina, Y., and Soulie, M. (2002). Modeling the transfer and retention of nutrients in the drainage network of the Danube River. *Estuarine, Coastal, and Shelf Science*, 54(3), 285-308.

Garrote, L., Bras, R.L. (1995). A distributed model for real-time flood forecasting using digital elevation models, *Journal of Hydrology, 167*, 279-306.

Giannoni, F., Smith, J.A., Zhang, Y., Roth, G. (2003). Hydrological modeling of extreme floods using radar rainfall estimates. *Advances in Water Resources, 26* (2), 195-203.

Giorgi, F., and L.O. Mearns (1999). Introduction to special section: Regional climate modeling revisited. *J. Geophys. Res.,* 104, 6335-6352.

Giorgi, F., and C. Shields (1999). Tests of precipitation parameterizations available in latest version of NCAR regional climate model (RegCM) over continental United States. *J. Geophys. Res.,* 104, 6353-6375.

Gochis, D.J., W.J. Shuttleworth, and Z.-L. Yang (2002). Sensitivity of the modeled North American monsoon regional climate to convection parameterization. *Mon. Wea. Rev.,* 130, 1282-1298.

Graf, W.L. (1983). Downstream changes in stream power in the Henry Mountains, Utah. *Annals of the Association of American Geographers*, Vol. 73, No. 3, pp373-387.

Grassotti, C., Hoffman, R.N., Vivoni, E.R., Entekhabi, D. (2003). Multiple-timescale intercomparison of two radar products and rain gauge observations over the Arkansas-Red River Basin. *Weather and Forecasting, 18* (6), 1207-1229.

Green, W.H., Ampt, G.A. (1911). Studies on soil physics, Part I. Flow of air and water through soils. *Journal of Agricultural Science, 4*, 1-24.

Groffman, P.M., Bain, D.J., Band, L.E., Belt, K.T., Brush, G.S., Morgan Grove, J., Pouyat, R.V., Yesilonis, I.C., and Zipperer, W.C. (2003). Down by the riverside: urban riparian Ecology. *Frontiers in Ecological Environments* 1, 315-321.

Halihan, T., Sharp, J. M., Jr., and Mace, R. E. (1999). Interpreting flow using permeability at multiple scales: *in Karst Modeling* (Palmer, A. R., Palmer, M. V., and Sasowsky, I. D., eds.) Karst Waters Institute Special publication No. 5, Charlottesville, VA, p. 82-96.

Halihan, T., Wicks, C.M., and Engeln, J.F. (1998). Physical response of a karst drainage basin to flood pulses: example of the Devil's Icebox cave system (Missouri, USA). *Journal of Hydrology* 204, 24-36.

Hall, M.J. (1984). Urban Hydrology. Northern Ireland: Elsevier Applied Science Publishers.

Hamlet, A.F., and Lettenmaier, D.P. (1999). Columbia River streamflow forecasting based on ENSO and PDO climate signals. *Journal of Water Resources Planning* and Management 125, pp333-341.

Harden, C.P., and Mathews, L. (2000). Rainfall response of degraded soil following reforestation in the Copper Basin, Tennessee, USA. *Environmental Management* 26, 163-174.

HEC (2002). River Analysis System: *Hydraulic Reference Manual*. Davis, California. U.S. Army Corps of Engineers Hydrologic Engineering Center.

HEC (2000). Hydrologic Modeling System: *Technical Reference Manual*. Davis, California. U.S. Army Corps of Engineers Hydrologic Engineering Center.

HEC (1996a). ModClark model development for the Muskingum River Basin, OH. Davis, California: U.S. Army Corps of Engineers Hydrologic Engineering Center.

HEC (1996b). A pilot application of weather radar-based runoff forecasting, Salt River Basin, Missouri. Davis, California. U.S. Army Corps of Engineers Hydrologic Engineering Center.

Hensell, J.L. (1977). Soil Survey of Bandera County, Texas. *U.S. Department of Agriculture*, Natural Resources Conservation Service, 42pp.

Higgins, R.W., W. Shi, E. Yarosh, and R. Joyce (2000). Improved United States precipitation quality control system and analysis. *NCEP/Climate Prediction Center ATLAS No. 7,* 40 pp.

Hirsch, R.M., Walker, J.F., Day, J.C., Kallio, R. (1990). The influence of man on hydrologic systems. *Surface Water Hydrology*, Boulder, CO: Geological Society of America.

Hirschboeck, K.K. (1987). Catastrophic flooding and atmospheric circulation anomalies. *Catastrophic Flooding,* Mayer, L. and D. Nash, Eds., The Binghamton Symposia in Geomorphology: International Series, No. 18, 23-56.

Hooke, J.M. (2004). Cutoffs galore!: occurrence and causes of multiple cutoffs on a meandering river. *Geomorphology* 61, 225-238.

Horritt, M.S., Bates, P.D. (2002). Evaluation of 1D and 2D numerical models for predicting river flood inundation. *Journal of Hydrology*, 268 (1-4), 87-99.

Hudson, P.F., Colditz, R.R. (2003). Flood delineation in a large and complex alluvial valley, lower Panuco basin, Mexico, *Journal of Hydrology, 280*, 229-245.

Jain, V., and Sinha, R. (2004). Fluvial dynamics of an anabranching river system in Himalayan foreland basin, Baghmati river, north Bihar plains, India. *Geomorphology* 60, 147-170.

Janić, Z.I. (1994). The step-mountain eta coordinate model: Further development of the convection, viscous sublayer, and turbulence closure schemes. *Mon. Wea. Rev.,* 122, 927-945.

Jankov, I., and W.A. Gallus, Jr. (2004). MCS rainfall forecast accuracy as a function of large-scale forcing. *Wea. Forecasting,* 19, 428-439.

Jayakrishnan, R., Srinivasan, R., Arnold, J.G. (2004). Comparison of raingage and WSR-88D Stage III precipitation data over the Texas-Gulf basin. *Journal of Hydrology,* 292 (1-4), 135-152.

Jiongxin, X. (2004). A study of anthropogenic seasonal rivers in China. *Catena* 55, 17-32.

Jordan, D.C., and Fonstad, M.A. (2005). Two dimensional mapping of river bathymetry and power using aerial photography and GIS on the Brazos River, Texas. *Geocarto International*, Vol. 20, No. 3, September 2005, pp1-8.

Juang, H.-M. H., and S.-Y. Hong (2001). Sensitivity of the NCEP regional spectral model to domains size and nesting strategy. *Mon. Wea. Rev.,* 129, 2904-2922.

Kessler, E. (1969). On the distribution and continuity of water substance in atmospheric circulation. *Meteor. Monogr.,* No. 32, Amer. Meteor. Soc., 84pp.

Knebl, M.R., Z.-L. Yang, K. Hutchison, and D.R. Maidment (2005). Regional scale flood modeling using NEXRAD rainfall, GIS, and HEC-HMS/RAS: a case study for the San Antonio River Basin summer 2002 storm event. *J. Environ. Manag.,* 75, 235-226.

Knox, J.C. (1977). Human Impacts on Wisconsin Stream Channels. *Annals of the Association of American Geographers* 67, 323-342.

Knox, J.C. (2001). Agricultural influence on landscape sensitivity in the Upper Mississippi River Valley. *Catena* 42, 193-224.

Larkin, R.G., and Sharp, J.M. (1992). On the relationship between river-basin geomorphology, aquifer hydraulics, and ground-water flow direction in alluvial aquifers. *Geological Society of America Bulletin* 104, 1608-1620.

Lawler, D.M. (1995). The impact of scale on the processes of channel-side sediment supply: a conceptual model, in Osterkamp, W.R. (Eds), *Effects of scale on the interpretation and management of sediment and water quality*, International Association of Hydrological Sciences Publications No. 226, 175-184.

Lecce, S.A. (1997). Spatial patterns of historical overbank sedimentation and floodplain Evolution, Blue River, Wisconsin. *Geomorphology* 18, 265-277.

Lee, K.S., Lee, S.I. (2003). Assessment of post-flooding conditions of rice fields with multi-temporal satellite SAR data. *International Journal of Remote Sensing*, 24 (17), 3457-3465.

Leopold, L.B. (1968). Hydrology for Urban Land Planning, Circular 559. U.S. Geological Survey, Washington, D.C.

Leopold, L.B. (1971). The Hydrologic effects of urban land use. Man's Impact on Environment. New York: McGraw-Hill.

Leung, L.R., Y. Qian, and X. Bian (2003). Hydroclimate of the western United States based on observations and regional climate simulation of 1981-2000. Part I: Seasonal statistics. *J. Climate,* 16, 1892-1911.

Liang, X.-Z., and K.E. Kunkel (2001). Development of a regional climate model for U.S. Midwest applications. Part I: sensitivity to buffer zone treatment. *J. Climate,* 14, 4363-4378.

Liang, X.-Z., L. Li, and K.E. Kunkel (2004a). Regional climate model simulation of U.S. precipitation during 1982-2002. Part I: Annual cycle. *J. Climate,* 17, 3510-3529.

Liang, X.-Z., L. Li, A. Dai, and K.E. Kunkel (2004b). Regional climate model simulation of summer precipitation diurnal cycle over the United States. *Geophys. Res. Lett.,* 31, L24208, doi:10.1029/2004GL021054.

Maclay, R.W., and Small, T.A. (1984). Carbonate geology and hydrology of the Edwards aquifer in the San Antonio area, Texas. *U.S. Geological Survey Open File Report* 83-537, 72pp.

Magilligan, F.J., Nislow, K.H., and Graber, B.E. (2003). Scale-independent assessment of discharge reduction and riparian disconnectivity following flow regulation by dams. *Geology* 31, 569-572.

Marston, R.A., Girel, J., Pautou, G., Piegay, H., Bravard, J.P., and Arneson, C. (1995). Channel metamorphosis, floodplain disturbance, and vegetation development: Ain River, France. *Geomorphology* 13, 121-131.

Mayer, J. M., and Sharp, J. M., Jr. (1998). Fracture control of regional ground-water flow in a carbonate aquifer in a semi-arid region: *Geol. Soc. America Bull.*, v, 110, p. 269-283.

Mesinger, F., G. DiMego, E. Kalnay, et al. (2006). North American Regional Reanalysis: A long-term, consistent, high-resolution climate dataset for the North American domain, as a major improvement upon the earlier global reanalysis datasets in both resolution and accuracy. *Bull. Amer. Meteor. Soc.,* 87, 343-360.

Michalakes, J., J. Dudhia, D. Gill, T. Henderson, J. Klemp, W. Skamarock, and W. Wang (2005). The Weather Research and Forecast Model: Software Architecture and Performance. *Proc. Eleventh ECMWF Workshop on the Use of High Performance Computing in Meteorology,* W. Zwieflhofer and G. Mozdzynski, Eds., World Scientific, 156–168.

Miles, E.L., Snover, A.K., Hamlet, A.F., Callahan, B., and Fluharty, D. (2000). Pacific Northwest Regional Assessment: The impacts of climate variability and climate change on the water resources of the Columbia River Basin. *Journal of the American Water Resources Association* 36(2), pp399-420.

Miller, W.M. (1978). Soil Survey of DeWitt County, Texas. *U.S. Department of Agriculture*, Natural Resources Conservation Service, 80pp.

Mitchell, M.J., R.W. Arritt, and K. Labas (1995). A climatology of the warm season Great Plains low-level jet using wind profiler observations. *Wea. Forecasting,* 10, 576-591.

Molina, R. (2000). Soil Survey of Karnes County, Texas. *U.S. Department of Agriculture*, Natural Resources Conservation Service, 217pp.

Muller, E. (1997). Mapping riparian vegetation along rivers: old concepts and new methods. *Aquatic Botany* 58, 411-437.

Nakamura, F., and Kikuchi, S. (1996). Some methodological developments in the analysis of Sediment transport processes using age distribution of floodplain deposits. *Geomorphology* 16, 139-145.

Nielsen-Gammon, J. W., F. Zhang, A. Odins, and B. Myoung (2006). Extreme rainfall events in Texas: Patterns and predictability. *Phys. Geogr.,* in press.

Nigam, S., and A. Ruiz-Barradas (2006). Seasonal hydroclimate variability over North America in global and regional reanalysis and AMIP simulations: varied representation. *J. Climate,* 19, 815-837.

Olson, D.A., N.W. Junker, and B. Korty (1995). Evaluation of 33 years of quantitative precipitation forecasting. *Wea. Forecasting,* 10, 498-511.

Patton, P.C. and V.R. Baker (1977). Geomorphic response of central Texas stream channels to catastrophic rainfall and runoff. *Geomorphology in arid regions,* Doehring, D.O., Ed., SUNY Binghamton Publications in Geomorphology, 189-217.

Paul, M.J., and Meyer, J.L. (2001). Streams in the urban landscape. *Annual Reviews of Ecological Systems* 32, 333-365.

Phillips, D.H., Foss, J.E., Stiles, C.A., Trettin, C.C., and Luxmoore, R.J. (2001). Soil-landscape relationships at the lower reaches of a watershed at Bear Creek near Oak Ridge, Tennessee. *Catena* 44, 205-222.

Pomerantz, M., Pon, B., Akbari, H., and Chang, S.-C. (2000). The effect of pavements' temperatures on air temperatures in large cities. :Lawrence Berkeley National Laboratory, LBNL-43442, Berkeley, California.

Puente, C. (1978). Method of estimating natural recharge to the Edwards Aquifer in the San Antonio area, Texas. *U.S. Geological Survey Water Resources Investigations* 78-10.

Ramsey, R.N., and Bade, N.P. (1977). Soil Survey of Guadalupe County, Texas. *U.S. Department of Agriculture*, Natural Resources Conservation Service, 82pp.

Reddell, J.R. (1964). The Caves of Comal County, 60pp.

Reddell, J.R. (1967). The Caves of Medina County, 58pp.

Reed, S.R., Maidment, D.R. (1995). A GIS procedure for merging NEXRAD precipitation data and digital elevation models to determine rainfall-runoff modeling parameters. *CRWR Report 95-3*. Austin, TX: Center for Research in Water Resources.

Robayo, O., Whiteaker, T., Maidment, D. (2004). Converting a NEXRAD map to a floodplain map. Paper presented at the meeting of the American Water Resources Association, Nashville, TN.

Rosgen, D.L. (1994). A classification of natural rivers. *Catena* 22, 169-199.

Schilling, K.E., Zhang, Y.K., and Drobney, P. (2004). Water table fluctuations near an incised Stream, Walnut Creek, Iowa. Journal of Hydrology 286, 236-248.

Senger, R.K., and Kreitler, C.W. (1984). Hydrogeology of the Edwards aquifer, Austin area, Central Texas. *The University of Texas at Austin, Bureau of Economic Geology Report of Investigations* No. 141, 35p.

Seth, A., and F. Giorgi (1998). The effects of domain choice on summer precipitation simulation and sensitivity in a regional climate model. *J. Climate,* 11, 2698-2712.

Sheng, Y., Gong, P., Xiao, Q. (2001). Quantitative dynamic flood monitoring with NOAA AVHRR. *International Journal of Remote Sensing*, 22 (9), 1709-1724.

Sieh, T.W. (1975). Edwards (Balcones Fault Zone) aquifer test-well drilling investigation: Austin, TX. Texas Water Development Board, 117p.

Smedsmo, J.L., E. Foufoula-Georgiou, and V. Vuruputur (2005). On the vertical structure of modeled and observed deep convective storms: insights for precipitation retrieval and microphysical parameterization. *J. Appl. Meteor.,* 44, 1866-1884.

Smith, M.B., Koren, V.I., Zhang, Z., Reed, S.M., Pan, J.J., and Moreda, F. (2004). Runoff response to spatial variability in precipitation: an analysis of observed data. *Journal of Hydrology* 298, 267-286.

Soil Survey Staff, Natural Resources Conservation Service, U.S. Department of Agriculture. Soil Survey Geographic (SSURGO) Database for Texas [Online WWW]. Available URL: “http://soildatamart.nrcs.usda.gov" [Accessed 07/05/05].

Taylor, F.B. (1977). Soil Survey of Wilson County, Texas. *U.S. Department of Agriculture*, Natural Resources Conservation Service, 102pp.

Taylor, F.B., Hailey, R.B, and Richmond, D.L. (1966). Soil Survey of Bexar County, Texas. *U.S. Department of Agriculture*, Natural Resources Conservation Service, 126pp.

Texas Natural Resource Information System (2005). Digital data download. Website online. Available from: http://www.tnris.state.tx.us. Accessed 1 April 2005.

Ting, M., and H. Wang (2006). The role of the North American topography on the maintenance of the Great Plains summer low-level jet. *J. Atmos. Sci.,* 63, 1056-1068.

Townsend, P.A., Walsh, S.J. (1998). Modeling floodplain inundation using an integrated GIS with radar and optical remote sensing. *Geomorphology, 21* (3-4), 295-312.

Twidwell, S.R., and David, J.R. (1987). Intensive surveys of San Antonio River segments 1901 and 1911, June 6, 1984-May 16, 1985: Austin, TX, *Texas Water Commission Report* IS-87-04, 87p.

U.S. Department of Agriculture, Soil Conservation Service. (1986). Soil Survey of Kerr County, Texas, 123pp.

U.S. Department of Agriculture, Soil Conservation Service (1972). Type IV Cooperative River Basin Survey: Texas Coastal Basins, 261pp.

U.S. Geological Survey (2006), in collaboration with Texas Water Development Board. Waterdata Groundwater Levels. Available from: http://waterdata.usgs.gov. Accessed 15 August 2006.

U.S. Soil Conservation Service (1986). Urban Hydrology for Small Watersheds *Technical Release 55*. U.S. Department of Agriculture.

Vaidya, S.S., and S.S. Singh (2000). Applying the Betts-Miller-Janjic scheme of convection in prediction of the Indian monsoon. *Wea. Forecasting,* 15, 349-356.

Veni, G. (1988). The Caves of Bexar County. 2nd Ed., Texas Memorial Museum, University of Texas at Austin, Austin, TX, 300pp.

Vieux, B.E., Bedient, P.B. (1998). Estimation of rainfall for flood prediction from WSR-88D reflectivity: a cast study, 17-18 October 1994. *Weather and Forecasting, 13* (2), 407-415.

Wadsworth, G. (1999). Flood Damage Statistics. Napa, CA: Public Works Department.

Walker, L.E. (1979). Occurrence, availability, and chemical quality of ground water in the Edwards Plateau region of Texas. *Texas Department of Water Resources, Report* No. 235, 337pp.

Wang, D., G. Wang, and E.N. Anagnostou (2005). Use of satellite-based precipitation observation in improving the parameterization of canopy hydrological processes in land surface models. *J. Hydrometeor.,* 6, 745-763.

Wang, W. and N.L. Seaman (1997). A comparison study of convective parameterization schemes in a mesoscale model. *Mon. Wea. Rev.,* 125, 253-278.

Warner, T.T., and H.M. Hsu (2000). Nested-model simulation of moist convection: The impact of coarse-grid parameterized convection on fine-grid resolved convection. *Mon. Wea. Rev.,* 128, 2211-2231.

Whiteaker, T.L., Maidment, D.R. (2004). Geographically integrated hydrologic modeling systems. *CRWR Report 04-04.* Austin, TX. Center for Research in Water Resources.

Whiteaker, T.L., Maidment, D.R., Robayo, O. (2004). Model integration through exchange of time series at information exchange points. Currently in submission.

World Meteorological Organization (2003). *Our Future Climate* (Publication WO-952).

Wolman, M.G. (1967). A cycle of sedimentation and erosion in urban river channels. *Geografiska Annaler* 49A, 385-395.

Wolman, M., and Miller, J. (1960). Magnitude and frequency of forces in geomorphic processes. *Journal of Hydrology* 69, 54-4.

Woodruff, C.M., and Abbott, P.L. (1979). Drainage-basin evolution and aquifer development in a karstic limestone terrain, south-central Texas, U.S.A. *Earth Surface Processes*, v. 4, pp319-339.

Xu, J., and E.E. Small (2002). Simulating summertime rainfall variability in the North American monsoon region: The influence of convection and radiation parameterizations. *J. Geophys. Res.,* 107, 4727, doi:10.1029/2001JD002047.

Zhang, Z.Y., Koren, V., Smith, M., Reed, S., Wang, D. (2004). Use of next generation weather radar data and basin disaggregation to improve continuous hydrograph simulations. *Journal of Hydrologic Engineering*, March/April, 103-115.

Zhang, F., A.M. Odins, and J.W. Nielson-Gammon (2006). Mesoscale predictability of an extreme warm-season precipitation event. *Wea. Forecasting,* 21, 149-166.

VITA

Marla Rose Knebl Lowrey was born in New Haven, Connecticut on February 28, 1978, the daughter of Dena Darlene Knebl and Siegmar Manfred Knebl. After graduating from Hamden High School, Hamden, Connecticut, in 1996, she entered Boston College in Newton, Massachusetts. She graduated with a B.S. in Geology and Music from Boston College in May 2000. During the following year she was employed as a geologist at the Massachusetts Water Resources Authority, and a substitute teacher at Brookline Public Schools. She received a Masters Degree in Music Education from The University of Texas at Austin in May 2003. She entered The University of Texas at Austin Department of Geological Sciences Graduate Program in August 2002.

Permanent address: 4305 Bonnell Vista Cv. #4, Austin, TX 78731

This dissertation was typed by the author.